Ranging with Ultra-Reliable and Low Latency mm-Wave Communication

Dissertation

zur Erlangung des akademischen Grades

Doktor der Ingenieurwissenschaften (Dr.-Ing.)

vorgelegt dem Fachbereich 1 (Physik/Elektrotechnik)

der Universität Bremen

von

Mohammad Soliman

Tag des öffentlichen Kolloquiums:	22.11.2024
Gutachter der Dissertation:	Prof. Dr.-Ing. Armin Dekorsy
	Prof. Dr.-Ing. Michael Meurer
Weitere Prüfer:	Prof. Dr.-Ing. Martin Schneider
	Prof. Dr.-Ing. Alberto Garcia-Ortiz

To my parents

Abstract

In the face of growing demand, the way rail infrastructure is used must change. Although it is obvious that the infrastructure is underutilized, conventional safety systems and the lack of direct communication between trains are the main reasons for the limited use of railroad tracks. One of the applications that has the potential to enable a significantly more efficient use of railroad infrastructure is Automatic Train Coupling (ATC). ATC is a method for automatically coupling and decoupling train wagons. This can be done while one wagon is standing still or while both wagons are in motion. ATC has the potential to increase track utilization for passenger and cargo trains by allowing easy physical coupling of wagons when they occupy the same track block and decoupling when they otherwise do not.

This thesis aims to address the theoretical and practical aspects of the realization of ATC. A wireless Train-to-Train (T2T) communication system capable of accurate ranging is required for the realization of ATC. To this end, standardized and non-standardized communication systems are analyzed and a communication system is recommended on the basis of the investigations. To evaluate the communication and ranging performance of the proposed communication system in realistic railroad environments, a measurement campaign was conducted with two train wagons. The measurement data was used to derive a channel model and thereby evaluate the performance of the communication system.

The observation of the channel and the behavior of the received components from the measurement campaign data has shown that the ranging accuracy of the communication system can be improved. In this study, a novel ranging estimation method is proposed that benefits from the knowledge gained from

the channel model. The novel ranging estimation method uses both Kalman filters and Space Alternating Generalized Expectation-Maximization (SAGE) to compensate for clock offsets by exploiting the knowledge of the mm-Wave channel.

The interaction between the proposed wireless communication system and all other systems involved in the ATC maneuver is designed. Designing the complete maneuver and all possible scenarios allowed translating the performance of the mm-Wave communication system into ATC maneuver success rate figures. The figures used are Safety Integrity Levels (SIL) which shows at which conditions would the ATC maneuver remain below a certain SIL threshold. Results show that using the proposed mm-Wave communication system and the proposed ranging estimation method allow a guaranteed SIL level 4 throughout the ATC maneuver.

Zusammenfassung

Aufgrund der wachsenden Nachfrage muss sich die Nutzung der Eisenbahninfrastruktur ändern. Obwohl es offensichtlich ist, dass die Infrastruktur nicht ausreichend genutzt wird, sind die konventionellen Sicherheitssysteme und die fehlende direkte Kommunikation zwischen den Zügen die Hauptgründe für die eingeschränkte Nutzung der Bahngleise. Eine der Anwendungen, die das Potenzial hat, eine wesentlich effizientere Nutzung der Eisenbahninfrastruktur zu ermöglichen, ist die automatische Zugkupplung. Automatische Zugkupplung ist ein Verfahren zum automatischen An- und Abkoppeln von Zugwaggons. Dies kann geschehen, während ein Waggon stillsteht oder während beide Waggons in Bewegung sind. Automatische Zugkupplung hat das Potenzial, die Gleisauslastung für Personen- und Güterzüge zu erhöhen, indem es eine einfache physische Kopplung von Waggons ermöglicht, wenn sie denselben Gleisblock belegen, und eine Entkopplung, wenn sie dies nicht tun.

Ziel dieser Arbeit ist es, die theoretischen und praktischen Aspekte der Realisierung von automatische Zugkupplung zu behandeln. Für die Realisierung von automatische Zugkupplung wird ein drahtloses Zug-zu-Zug-Kommunikationssystem benötigt, das in der Lage ist, eine genaue Entfernungsmessung durchzuführen. Zu diesem Zweck werden standardisierte und nicht-standardisierte Kommunikationssysteme analysiert und auf der Grundlage der Untersuchungen ein Kommunikationssystem empfohlen. Um die Kommunikations- und Entfernungsmessungsleistung des vorgeschlagenen Kommunikationssystems in realistischen Eisenbahnumgebungen zu bewerten, wurde eine Messkampagne mit zwei Zugwaggons durchgeführt. Die Messdaten wurden zur Ableitung eines Kanalmodells und damit zur Bewertung

der Leistungsfähigkeit des Kommunikationssystems verwendet.

Die Beobachtung des Kanals und des Verhaltens der empfangenen Komponenten aus den Daten der Messkampagnen hat gezeigt, dass die Entfernungsgenauigkeit des Kommunikationssystems verbessert werden kann. In dieser Studie wird eine neuartige Methode zur Entfernungsschätzung vorgeschlagen, die von den Erkenntnissen aus dem Kanalmodell profitiert. Die neuartige Entfernungsschätzungsmethode verwendet sowohl Kalman-Filter als auch Space Alternating Generalized Expectation-Maximization (SAGE), um Taktabweichungen zu kompensieren, indem das Wissen über den mm-Wellen-Kanal ausgenutzt wird.

Die Interaktion zwischen dem vorgeschlagenen drahtlosen Kommunikationssystem und allen anderen am automatische Zugkupplung-Manöver beteiligten Systemen wird entworfen. Die Entwicklung des gesamten Manövers und aller möglichen Szenarien ermöglichte es, die Leistung des mm-Wave-Kommunikationssystems in Zahlen zur Erfolgsrate des automatische Zugkupplung-Manövers zu übersetzen. Bei den verwendeten Zahlen handelt es sich um Safety Integrity Levels (SIL), die angeben, unter welchen Bedingungen das automatische Zugkupplung-Manöver unter einem bestimmten SIL-Schwellenwert bleiben würde. Die Ergebnisse zeigen, dass die Verwendung des vorgeschlagenen mm-Wellen-Kommunikationssystems und der vorgeschlagenen Entfernungsschätzungsmethode während des gesamten automatische Zugkupplung-Manövers eine garantierte SIL-Stufe 4 ermöglicht.

Contents

Chapter 1

Introduction

Rail and road are the most popular modes of passengers and goods transport. Rail transport systems comprise High Speed Trains (HST), freight trains, tramways and others. Road transportation systems include cars, buses, and trucks.

Although rail transport is safer, more energy efficient, and more environmentally friendly, it is less popular compared to road transport systems. Cars, buses, and trucks carry more than 78 % of freight and 87 % of passengers, while trains and light rail carry 18 % of freight and just 10 % of passengers in Europe [CMT21]. Due to ever-increasing fuel prices and operating costs for road vehicles, attention to rail transport has continued to grow. This has drawn attention to the very difficult task of making rail transport more attractive and efficient. For all these reasons, it is worth investigating why rail transport is less attractive and how its attractiveness can be increased.

One issue related to this work is the inefficient use of rail infrastructure. As shown in Figure 1.1, the rails are not utilized to the same extent as roads. And in view of the growing demand, the way in which the railroad infrastructure is used must change. Conventional safety systems and the lack of direct communication between trains are the main reasons for the limited use of rail tracks. To explain inefficient use of rail infrastructure, consider a HST line. Trains must maintain a distance at least equal to their braking distance. To ensure maintaining enough space between trains utilizing the

Figure 1.1: A comparison of the utilization of road and rail transport infrastructure [A8H][Zur].

same track, the tracks are divided into blocks, and only one train can use a block at a time. On HST tracks a block can exceed 10 km in length.

In Europe, the European Train Control System (ETCS) standard prescribes how train control and signaling is used. Several levels are defined for ETCS. ETCS level 1 includes trackside equipment, namely the Eurobalise modules, which signal whether a particular block is occupied. ETCS level 2 extends the previous level to include wireless communication using Global System for Mobile Communications - Railway (GSM-R) technology to allow trains to exchange their locations with a Centralized Traffic Control (CTC) or with each other to increase reliability. ETCS level 3 introduces moving blocks where the blocks are no longer fixed. A safety distance is established behind and in front of a train and is maintained when the train is stationary or moving.

ETCS level 3 enables much more efficient use of infrastructure compared with the previous levels. However, the use of new technologies in rail transport is extremely limited compared with road transport. For example, ETCS level 3 continues to rely on the outdated GSM-R technology. An example of ETCS levels 1 and 3 with the fixed and moving blocks is shown in Figure 1.2.

ETCS level 3 significantly reduces the safety distance between trains, but there is still considerable potential for improvement. Envisioned future railroad applications such as autonomous trains, virtual coupling, intelligent traffic management and others rely heavily on wireless communication

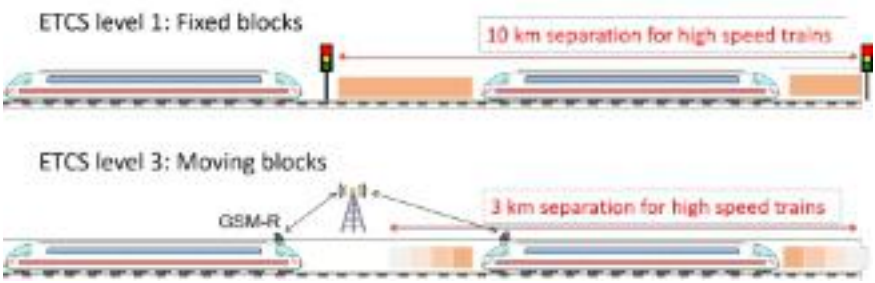

Figure 1.2: An illustration of ETCS level 1 and ETCS level 3 in railways.

systems. Therefore, the research on wireless communication systems and their application in rail transport has attracted more attention in recent years to review the application of various communication systems for rail transport [UPS+16]. In this work, one of the proposed future applications, namely Automatic Train Coupling (ATC), is investigated and a wireless communication system is proposed and evaluated to enable ATC.

1.1 Application and Open Challenges

In order to increase the efficiency and thus the attractiveness of rail transport, it is important to take large steps and directly use the most advanced wireless communication technologies to enable future applications. Therefore, several future applications are highlighted in this work, and exploring the wireless communication systems that enable these applications is a major focus.

One of the applications that has the potential to enable much more efficient use of rail infrastructure is ATC. In this work, ATC is defined as a process that allows train wagons to be automatically coupled and decoupled. This can be done while one wagon is stationary near a platform or in a shunting yard, while the other wagon is arriving or departing, or while both wagons are in motion. ATC has the potential to increase railroad track utilization for HST by allowing rail wagons to be easily physically coupled when they occupy the same track block and decoupled when they are to use other tracks. Automatic coupling can be achieved if a reliable ATC system is implemented that efficiently and completely automates the whole maneuver.

To enable ATC, a robust and Ultra-Reliable Low-Latency Communication (URLLC) system that enables direct Train-to-Train (T2T) communication is required. In addition, an accurate estimate of the relative distance between the train wagons is required. Therefore, it is advantageous if the communication system is able to estimate the distance between the train wagons and exchange the estimated distance among the wagons. Distance estimation is called ranging hereinafter. When designing a T2T communication system that enables ATC, many challenges can arise. For example, to evaluate a direct T2T communication system, an accurate channel model in the relevant frequency band and environment is required. To the best of our knowledge, there are no available channel models in the railroad environment and the relevant frequency band. Furthermore, in order to properly evaluate a communication system and assess whether it is suitable for a safety-critical application such as the ATC application, the difficult task of using the correct evaluation criteria arises. To ensure a meaningful evaluation, the interaction between all systems involved, including the communication system, must be modeled, and the evaluation criteria must be derived based on the model outcome. More details about the communication system, its performance requirements, design, and evaluation will be provided throughout this thesis.

1.2 Aim of the Thesis

The objectives of this thesis address the theoretical and practical aspects to realize ATC. At its core, ATC will involve multiple systems: a control system, a wireless T2T communication system capable of ranging, mechanical systems such as the brakes and the engine, and other on-board systems. To this end, the focus of this work is on the investigation of a suitable wireless communication systems for the realization of ATC. For this purpose, standardized and non-standardized communication systems are analyzed and a communication system is recommended based on the investigations.

Theoretical analysis of the communication and ranging subsystems will be held where multiple performance criteria, such as Packer Error Rate (PER) and ranging accuracy, will be highlighted. To analyze the performance of the communication system, a channel model is required. As will be discussed in

chapter 4, there are no channel models for the proposed frequency band and the rail environment. Therefore, a propagation measurement campaign was held specifically covering the channel between two train wagons in the rail environment. A realistic channel model will be derived from the collected data.

Furthermore, the interaction between the proposed wireless communication system and all other systems involved in the ATC maneuver will be studied and designed. The motivation behind studying the interactions between the communication system and other systems is that it is important to address the research questions from all relevant angles by linking the performance of the wireless communication system to the probability of performing a successful ATC maneuver. Doing so allows us to conclude whether the wireless communication system and other on-board systems are suitable to enable the ATC application.

1.3 Contribution and Structure of the Thesis

The main contribution of this work is to address the aforementioned research questions to enable ATC. The research questions are summarized in the following bullets:

- What wireless communication systems can be considered for ATC?
- How to derive a realistic channel model to evaluate the communication system under consideration?
- How much PER and ranging accuracy are expected during an ATC maneuver?
- What impact do PER and ranging accuracy have on the entire system and the maneuver's overall success?

This work begins with a literature review of the state of the art for wired and wireless railroad communication systems and then extends a proposed Single Carrier (SC) Millimeter Wave (mm-Wave) system, namely the Reliable and Low-Latency Broadband Transmission over Short Distances (SBDist) system, to improve its performance for the ATC application.

To enable the evaluation of the mm-Wave communication system, a mm-Wave channel model in the railroad environment is required. Due to the lack of channel models in the literature, a propagation measurement has been performed and the collected data is to be used to derive a realistic mm-Wave channel model in the railroad environment.

In addition, the ranging accuracy of the proposed mm-Wave system is evaluated and lower performance bounds are derived to compare the ranging performance with other communication systems. Besides, an innovative ranging scheme that can compensate for clock offset is introduced.

To complete this research, a system-level design for the ATC maneuver is required. The purpose of the design is to highlight the relevant communication and ranging requirements. The outcome of analyzing the system design will determine if the proposed mm-Wave system shall fulfill the ATC application requirements.

The structure of the thesis is as follows:

- Chapter 2 lays the foundation for this thesis by examining the state of the art of wired and wireless communication systems in the railroad sector. On the one hand, standardized wired Train Communication Network (TCN) on-board systems such as Multifunction Vehicle Bus (MVB) and Wire Train Bus (WTB) are explained. On the other hand, various wireless communication systems are discussed, including standardized ones such as GSM-R, Long Term Evolution - Railway (LTE-R), and Terrestrial Trunked Radio (TETRA), as well as proprietary technologies such as Future Railway Mobile Communication System (FRMCS) and the SBDist system. The SBDist system is of interest to enable ATC because it provides direct T2T communication, uses a wideband signal that is beneficial for ranging, and can be mounted on the nose of train cars near the coupler. Furthermore, a Device-to-Device (D2D) variant of the Institute of Electrical and Electronics Engineers (IEEE) 802.11 standard communication system, namely the Intelligent Transport Systems at 5.9 GHz (ITS-G5) system, is considered and compared with the SBDist system in the evaluation of distance accuracy for ATC.

- Chapter 3 describes the SBDist system and explores various ways to

extend the design of the SBDist system to improve its communication and ranging performance. The physical layer of the SBDist system is extended by introducing frequency domain equalization at the receiver and by using a preamble sequence, which provides better performance. Zadoff-Chu sequences are used for channel estimation and equalization, and Golay sequences are used for fine synchronization for ranging. Moreover, Circularly Polarized Antennas (CPAs) and redundancy are proposed to improve the PER performance of the SBDist system. Eventually, an efficient Monte Carlo simulation environment is developed to generate PER performance values as low as 10^{-8}.

- Chapter 4 begins by examining possible channel models that can be used to evaluate the communication and ranging performance of the SBDist system. To the best of our knowledge, there are no mm-Wave channel models in railroad environments in the literature. Therefore, we prepared and conducted the first dynamic mm-Wave T2T propagation measurement campaign. The preparation included the construction of two mm-Wave front-ends capable of being directly connected to the German Aerospace Center (DLR) RUSK channel sounder. The testing and evaluation of the mm-Wave front-ends was performed and the measurement campaign took place at the premises of RWTH Aachen University. The collected data were used to derive a mm-Wave T2T channel model. A three-ray geometry based channel model fitted the measurements and will be used in the next chapter to improve the ranging accuracy.

- Chapter 5 addresses the subject of ranging accuracy. The chapter begins with a discussion of various ranging schemes such as Round Trip Delay (RTD) and Time of Arrival (ToA), as well as the theoretical lower bounds on ranging accuracy for the ToA scheme. The lower bounds, namely the Cramér Rao Lower Bound (CRLB), are calculated for the distance estimation accuracy of the SBDist system and compared with the distance estimation accuracy lower bounds of ITS-G5 and Impulse Radio - Ultra Wide Band (IR-UWB). The SBDist system outperforms the other two systems due to its wider bandwidth and higher transmit power on the Industrial, Scientific and Medical (ISM)

mm-Wave band. In addition, an Expectation Maximization (EM)-based parameter estimation algorithm, namely the Space-Alternating Generalized Expectation-maximization (SAGE) algorithm, is used to estimate the distance between the train wagons using the recorded data during the measurement campaign. As an extension of the SAGE algorithm, the Kalman filter is used to include velocity measurements from on-board equipment in addition to the received impulse responses from the communication system. While the Kalman filter marginally improves distance estimation accuracy by eliminating outliers, the offset between the transmitter and receiver clocks contributes significantly to the error of the distance estimates. Therefore, an innovative state-of-the-art algorithm is used that takes advantage of the knowledge gained from the propagation measurements. By utilizing the channel knowledge and multipath components, we were able to develop an algorithm where the clock offsets were compensated. The performance of the proposed algorithm was evaluated using real-world measured data and computer simulations.

- Chapter 6 plays an important role in quantifying the performance of the communications and ranging subsystems in a manner that serves a meaningful conclusion. The chapter begins with a description of the various on-board systems involved in the ATC maneuver and how they interact with each other. Standardized wired TCN protocols are used to enable communication between all participating systems on board. An unconventional but important step in the quest to link system requirements to performance values is to analyze the mechanical aspects of the trains and define the required relative velocity at each separation distance. In this way, and by designing the ATC maneuver using Petri Nets (PN), it was possible to highlight that at each separation distance a certain number of successive errors is allowed, which decreases as the train cars get closer. In addition, worse distance accuracy decreases the number of successive errors allowed throughout the maneuver. Using the performance values from Chapters 3 and 5, it has been demonstrated that the SBDist system can meet the most demanding requirements of the Safety Integrity Level (SIL)-4 criterion throughout

the ATC maneuver.

1.4 Notation

The most important nomenclature is given in the following. Unless otherwise stated, this nomenclature applies to all parts of this work.

- Small italic characters denote scalars x and bold italic lowercase characters denote a column vector $\mathbf{x}$. Upper case bold italic characters denote a matrix $\mathbf{X}$.
- A continues function x at the instance n is denoted as $x\left(n\right)$, while a discrete function is denoted as $x\left[n\right]$.
- The transpose of a matrix is denoted as $\mathbf{X}^{\intercal}$ and the conjugate transpose of the matrix is denoted as $\mathbf{X}^{*}$. $\mathbf{X}^{-1}$ denotes the matrix inverse.
- The $N \times N$ identity matrix is denoted as $\mathbf{I}_N$.
- The estimated value of the parameter x is denoted as $\hat{x}$.
- log denotes the logarithm with respect to the basis 10.
- The absolute value of x is denoted as $|x|$ and $x{*}y$ implies the convolution operation on x and y.
- The aperiodic autocorrelation function of a sequence x is $C_x\left(\tau\right)$. $\delta\left(t\right)$ is a dirac function at time t.
- A Probability Density Function (PDF) of the random variable y is written as $p_y\left(y\right)$, a likelihood function of the variable x based on the observation y is written as $p_y\left(y|x\right)$.

Chapter 2

State of the Art

2.1 Wired Communications in Trains

In 1988, International Electrotechnical Commission (IEC) Technical Committee 9 established a working group to standardize a joint train communication network for railroad applications. Concurrently, several railroad system suppliers, such as Siemens and ASEA Brown Boveri (ABB), established a joint development project to develop a common prototype for such a communication system and to prove the feasibility of the concept. The outcome of this project was a reference implementation of hardware and software for a Train Communication Network (TCN) network and a laboratory test bed to verify and fine-tune the performance.

In October 1999, TCN became an international standard. TCN has been standardized by International Electrotechnical Commission (IEC) [IEC] and by the IEEE [IEE99]. The work on standardizing the application level was done in parallel to the development of the TCN system. The outcome is a definition of the periodic and sporadic frames and their content and structure. The definition was governed by the International Union of Railways (UIC) code 556 standard [SH00].

The architecture of the TCN takes into account all relevant topologies used in rail vehicles. It includes two layers, the Wire Train Bus (WTB) connecting multiple train wagons and the Multifunction Vehicle Bus (MVB)

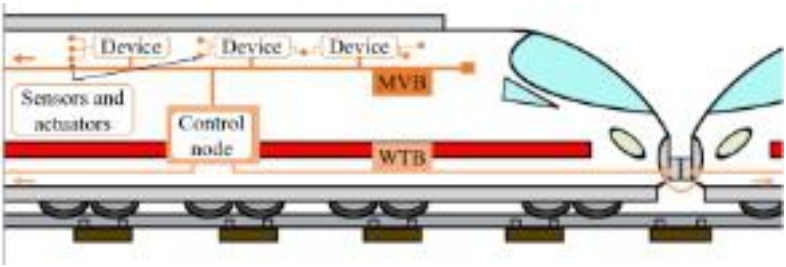

Figure 2.1: Architecture of the TCN network. MVB connects devices within a train wagon and WTB connects train wagons with each other.

connecting the equipment on board each train wagon, as shown in Figure 2.1.

A railroad wagon may be equipped with one or more MVB. To accommodate a variety of wagons and equipment, TCN uses logical addressing. That is, each device connected to the train control node is expected to support a set of application functions, each accessible by a unique function number. Each function can be performed by one or more devices or by the train control node itself. Moreover, each device can perform multiple functions. From the outside, it looks as if the train control node itself executes all functions. In other words, the internal structure is not visible from the outside.

2.1.1 Multifunction Vehicle Bus

The MVB is specified as a vehicle bus that connects the equipment on board the wagons in a closed train set. The MVB operates with 1.5 Mbit/s data rate over three media types: RS-485 for short distance up to 20 m, twisted pair wire for distances up to 200 m, and optical fiber for distances up to 2000 m. The different media can be interconnected directly with repeaters.

MVB is controlled by a dedicated bus master, which can be supported by backup redundant masters to increase reliability. MVB is supported by an integrated bus control system, which allows the setup of simple devices.

2.1.2 Wire Train Bus

For trains whose composition changes frequently, such as international trains or suburban trains, WTB was developed to connect the wagons with each other using hand plug connectors or automatic couplers. A shielded twisted pair is used for cabling, which transmits data at a rate of 1 Mbit/s and is capable of achieving redundancy.

The WTB covers train wagons of 860 m length and allows up to 32 control nodes to be connected. WTB uses Manchester II codes. Considering the harsh environment and the presence of connectors and interruptions on the bus path, a digital signal processor is used to encode and decode the Manchester signal [Zur05].

WTB is able to automatically assign numbers to the train control nodes in consecutive order. Furthermore, it is able to let all nodes recognize the heading direction of the train. Every time the train composition changes, e.g. when adding or removing carriages, the train bus nodes perform the inauguration procedure, which electrically connects the nodes and assigns each node its address. The train bus nodes are numbered consecutively. Generally, there is one node per wagon. However, there may be more than one node per wagon. In addition, one control node is assigned the role of master, while the others are assigned a slave role. The master role is usually the one furthest forward in the sequence. At the end of the inauguration, all vehicles are informed of the WTB topography.

The inauguration procedure is complex, as it not only ensures the correct node numbering and identification, but also the transition from the power-saving sleep mode to the active mode. To enable fast recovery in the event of a bus interruption, each control node has the option of becoming a bus master. In such a case, the master status is automatically transferred to a neighboring control node.

The functions of WTB and MVB are summarized in Table 5.1.

2.1.3 Real-Time Protocols

While WTB and MVB differ in the physical and link layers, both obey the same protocols (also known as Real-Time Protocol (RTP)) in terms of higher

WTB	MVB
up to 860 m	up to 200 m (wire) or 2000 m (optical)
automatic configuration	fixed configuration
relative addressing	absolute addressing
up to 32 control nodes	up to 256 devices
1 Mbit/s data rate	1.5 Mbit/s data rate
25 ms update period	1 ms update period

Table 2.1: Characteristics of WTB and MVB.

layers and especially user interfaces.

TCN provides two types of data service:

- Periodic process variable data frames such as train speed, motor current and others. Process variable information is transmitted periodically to ensure reliable and up-to-date data.

- Sporadic messages containing infrequent but possibly longer information such as diagnostics or passenger information. The message length varies between a few bits and several thousands of bits. The transmission delay of messages must be short, but variations are allowed. For this reason, messages are transmitted on demand.

Periodic (process data) and sporadic (messages) traffic share the same bus, but are handled separately in the devices. All buses belonging to the TCN are expected to provide these two basic data services. The periodic and sporadic transmission of data is controlled by a device acting as a master. This guarantees deterministic access to the medium. For this purpose, the master alternates between periodic and sporadic phases, as shown in Figure 2.2.

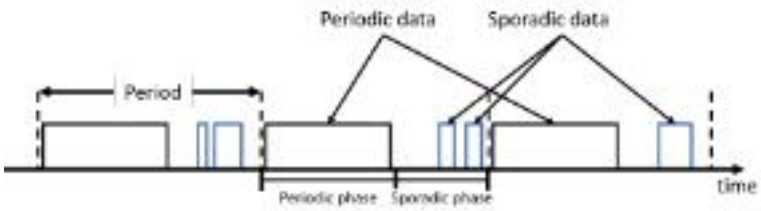

Figure 2.2: Periodic and sporadic data transmission as defined by IEC for the TCN network.

The periodic phase occupies a fixed slot of the bus time. During that time, the master control node queries the variables one by one. Variables include information regarding the state of the train collected by different devices such as the status of the doors, ventilation, lights, emergency brake, and others. The basic period is either 1 ms or 2 ms on the MVB and 25 ms on the WTB.

Application-specific profiles such as the content of process data frames and messages, their meaning, the period of process data, special requirements for redundancy, and so forth are defined by the UIC in the UIC-556 standard [SH00].

In this work, the international standards IEC 61375-1 and UIC-556 TCN will be considered in the definition of the requirements to enable ATC.

2.2 Wireless Communications in Trains

Digital wireless communication systems were recently introduced to the railroad sector. Two distinctive applications were targeted by introducing various wireless communication systems. The first application is related to infotainment and passenger connectivity. The second application covers transmitting and receiving train control system messages. The messages can be transferred directly between different trains or to a Centralized Traffic Control (CTC) via road side units. Infotainment and passenger connectivity applications are not discussed in this work as they cover different use cases and have different requirements.

Three directions have been taken to develop communication systems

capable of communicating control system messages. The three directions are:

- to develop communication systems based on open standards such as TETRA [RGLSF08], Global System for Mobile Communications (GSM), General Packet Radio Service (GPRS), and IEEE 802.11 group of standards [Fit06],

- to develop communication systems based on open standards but with slight or moderate modifications on some layer such as GSM-R and LTE-R ([KBNJ06], [HAW+16]),

- to specifically develop proprietary technologies for railways, such as European Train Control System (ECTS) EUROBALISE [Kje96] and the SBDist system [SSS+17].

In the following, the most prominent wireless communication systems, their advantages, and the possibility of using them to fulfill ATC application requirements is discussed.

2.2.1 GSM-R, LTE-R, and FRMCS

GSM-R is the most utilized wireless system in the railways domain. GSM-R is based on the GSM standard phase 2+ and is developed to cover specific railways requirements. GSM-R operates at the 900 MHz frequency band and there are some major difference when compared to GSM. The most important differences are the ability to perform voice broadcasts, voice group calls, and the ability to specify a priority value before initiating a call.

Voice broadcasts allow an initiator to transmit a voice command to multiple recipients by transmitting the information of the initiator and his cell identification to the Mobile Switching Center (MSC) (GSM core network). The MSC in the other hand establishes a single channel with each affected cell to enable all the recipients to listen to the incoming message. Voice group calls are similar to voice broadcasts but it gives the recipients the opportunity to gain control to the uplink, giving them a chance to transmit a broadcast after the initiator releases their connection.

Other issues were being highlighted by GSM-R such as the handover of calls at very high speeds up to 500 km/h and the topic of packetized data using GPRS [Wat96].

As GSM-R is approaching its obsolescence, later mobile communication generations are thought of as replacements. LTE-R is thought of as a natural successor to GSM-R. Naturally, better performance is expected from LTE-R. For example, LTE-R provides a system delay of 100 ms which is four times better when compared to the 400 ms system delay provided by GSM-R. LTE-R supports high data rates up to 100 Mbit/s [CLML18]. LTE-R is already applied as a replacement in many counties such as South Korea and was argued to potentially solve all the shortcomings of GSM-R [SS14].

In contrast, UIC are leaning towards skipping two generations and standardize a future communication system, namely the FRMCS, based on releases 15 and 16 of the Fifth Generation Mobile Network (5G) standard. FRMCS and other modern digital communication systems are planned to be integrated to digitize the ECTS providing a more reliable and efficient use of the infrastructure. For example, a so-called Digital Train Control System is planned to become applied to the underground lines in the city of Frankfurt, Germany. This will allow the underground trains to travel in shorter intervals closer to each other. In other words, the capacity of trains using the same infrastructure can be increased by 25 percent.

GSM-R, LTE-R, and FRMCS systems use Road Side Unit (RSU)s to enable communication between multiple trains. Therefore, the aforementioned systems do not allow direct T2T communication. Instead, all data is sent to a CTC, which distributes the data as it deems necessary.

2.2.2 TETRA and ITS-G5

It is envisioned that direct wireless T2T communication systems will be key enablers for future applications such as ATC. Enabling such and other applications would obviously increase the utilization of train wagons and enable more efficient use of infrastructure in the future. Therefore, this study considers possible standardized systems enabling Direct-Mode Operation (DMO), such as TETRA and ITS-G5.

TETRA is a two-way and trunked radio system designed specifically for

use by government agencies such as emergency services, police, ambulance, and fire departments. TETRA is also used by railroad employees for train radios, transportation services, and the military. TETRA was standardized by European Telecommunications Standards Institute (ETSI) in 1995.

TETRA operates in the lower Ultra High Frequency (UHF) band at 450 MHz and uses Time Division Multiple Access (TDMA) with four channels on each carrier frequency and 25 kHz spacing between the carriers. DMO and broadcast communication are both possible. Digital data transmission is also enabled at low data rate. TETRA DMO is especially interesting to allow direct T2T communication.

TETRA is intended as an auxiliary system that allows trains to communicate directly with each other and to communicate their current location and heading to other trains in the area. For example, the TrainCAS system based on TETRA uses Global Positioning System (GPS) and locally stored railroad maps to calculate the train's location and direction of travel. The location information, as well as the train's identification, is transmitted to all other trains within range via a TETRA-based wireless communication system. The performance of the TrainCas system was evaluated in [LSU17].

TrainCas allows a large transmission coverage of up to 39 km. This is made possible by the low carrier frequency of the TETRA wireless communication system. However, TETRA-based systems are not suitable for short-range communications due to their low data rates and high update delay due to the limited available frequency resources. To overcome the shortcomings of TETRA, ITS-G5 is considered as a potential system to enable direct T2T communication. ITS-G5, also known as IEEE 802.11p is a variation on the IEEE 802.11 standard and is defined by ETSI [ETS19]. ITS-G5 operates at 5.9 GHz and typically uses channels of 10 MHz bandwidth. ITS-G5 allows wireless DMO by enabling direct D2D communication.

ITS-G5 is mainly used to enable D2D communication between cars, trucks, and RSUs in the automotive domain ([TMS21], [TFB20], [MNH+22]). Recently, studies were initiated to evaluate the performance of ITS-G5 in railways environments to enable T2T and inside-train communication ([SUG16], [URWK20], [GMB+18]). Therefore, ITS-G5 is considered in this work to enable ATC.

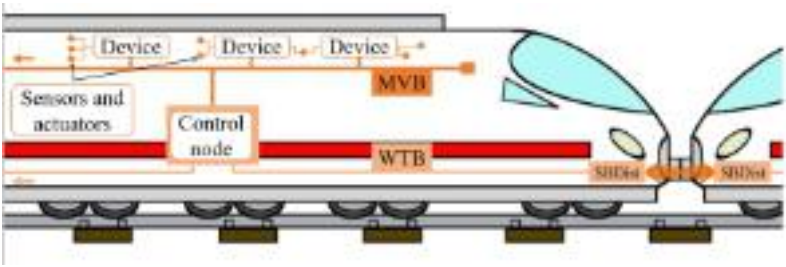

Figure 2.3: Architecture of the TCN network after integrating the SBDist module.

2.2.3 SBDist

In 2015, a project funded by the German Federal Ministry of Education and Research was launched to develop a short-range URLLC technology. This wireless technology enables high data rates, reliable and low-latency wireless communication on moving units over short distances up to a few meters covering multiple use cases in the industrial domain.

One application in which the technology has been validated is for communication between railroad passenger wagons to replace the mechanical wired connections previously required. After a requirements analysis and concept evaluation, it has been decided to implement the SBDist radio modem with a single carrier SC radio system in the mm-Wave band at a carrier frequency of 60 GHz. The requirement profiles and applications covered by the SBDist system are discussed in detail in [SSS+17].

The main application of the project is to replace the wired connection between the wagons with a wireless modem. There are two reasons for the proposed replacement. The first is the susceptibility of the WTB interface bins to physical damage due to frequent coupling and decoupling. This increases repair time and operating costs. The second reason is to investigate possible future applications, such as virtual coupling, where the train wagons do not necessarily need to be physically coupled. The proposed architecture is shown in Figure 2.3.

As illustrated, the SBDist system must transfer safety critical TCN data between wagons following WTB protocol. To fulfill this requirement, end-to-

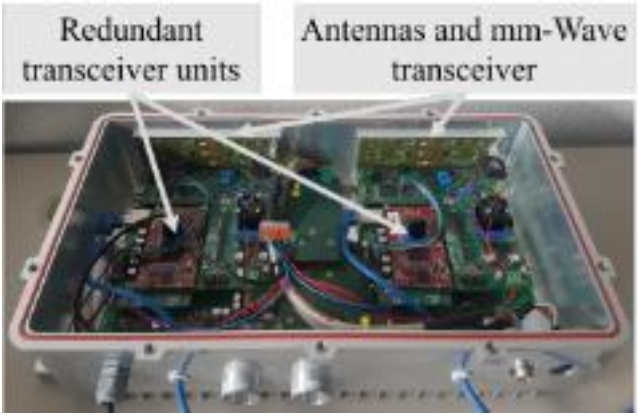

Figure 2.4: An SBDist module with two redundant transceiver units [SSS+17].

end latency must be below 50 µs and extremely low PER are expected.

Furthermore, robustness against damage and physical failure are required. Therefore, the SBDist system consists of two redundant transceiver units operating in parallel at two different carrier frequency utilizing Frequency Division Duplex (FDD) and both transceiver units are held inside water-, shock-, and weather-resistant housing. The SBDist module and the two redundant transceiver units are shown in Figure 2.4. Each transceiver unit is connected with two highly directional antennas where one antenna acts as a transmitter and the other acts as a receiver. Utilizing FDD allows the SBDist system to operate at minimal latency measured at 40 µs to 45 µs.

The SBDist system uses a SC physical layer architecture with a convolutional encoder to improve PER performance, and combined with the highly directional antennas, PER values of $10^{-}9$ are possible. The SBDist system uses a wideband signal with a bandwidth of 500 MHz to enable the transmission of data that requires high data rates, such as videos from on-board surveillance systems. The SBDist system is considered an excellent candidate for the ATC application due to the wide bandwidth, the use of highly directional antennas, and the ability to place the SBDist modules on the nose of the train wagons in proximity to the mechanical couplers.

2.3 Train Coupling

Train coupling is the connection of two train wagons in order to couple them mechanically and exchange data via the TCN network. There are various techniques for mechanically connecting trains. The best known mechanical couplers are the Scharfenberg couplers, named after Karl Scharfenberg, who designed the couplers in 1903. Scharfenberg couplers have small pneumatic cylinders that act on the rotating coupler heads to ensure engagement of the locking components, eliminating the need for force to make a proper engagement.

It is worth noting that while the mechanical interfaces are standardized, the electrical interfaces are not. Therefore, the couplers produced by different manufacturers are not necessarily compatible with each other. Apart from that, Scharfenberg couplers are widely used in Germany, France, the United Kingdom, the United States and many other countries.

Scharfenberg couplers are what are commonly referred to as automatic couplers in the railroad industry. By definition, automatic coupling means that the WTB interfaces and the electrical interfaces connect automatically as soon as both trains are mechanically coupled.

Automatic coupling may sound as if the entire process is automated, but that is not the case. The procedure itself is manual, with the driver carefully increasing the speed of one wagon while the other wagon stands still. Typically, another staff member is present on the platform to observe and guide the driver as he moves the wagon toward the stationary wagon until both wagons are fully coupled. A similar procedure applies to uncoupling two train wagons.

In this work, ATC extends the previously underlined definition by allowing trains to automatically approach each other and couple until they are mechanically and electrically coupled, and vice versa. This means that two separate train wagons can approach each other until they physically connect with the push of a button. To enable ATC, both train wagons must communicate with each other and measure the separation distance during the coupling process. Therefore, a reliable wireless connection capable of distance estimation must be maintained throughout the maneuver.

A possibility is to use the SBDist system while the train wagons are

close to each other to enable wireless communication and ranging. In this way, both train wagons can communicate and exchange their separation distance during the ATC maneuver. In addition, the use of the SBDist system will potentially solve the compatibility problem so that train wagons from different manufacturers can be successfully coupled.

2.4 Summary

In this chapter, we discussed the state of the art wired and wireless communication systems on-board of modern trains. Wired TCN protocols such as MVB and WTB are standardized by international bodies and are widely used by major manufacturers and in many countries. A different story is told for wireless communication systems. Various standardized and non-standardized communication systems are used to accommodate specific applications. Different technologies are used by different manufacturers based on the requirements and demands.

Furthermore, state of the art mechanical couplers, namely the Scharfenberg couplers, are discussed in this chapter. While Scharfenberg couplers are defined as automatic couplers, we want to extend the definition by enabling a fully autonomous ATC maneuver where two train wagons couple or disengage by the press of a button. To achieve this goal, a reliable wireless communication system capable of distance estimation is required to maintain a connection between the two involved wagons throughout the maneuver.

In the following, we will discuss the possibility of extending the SBDist system to provide reliable communication and ranging. In addition, the SBDist system will be evaluated to ensure that performance is above the baseline performance threshold.

Chapter 3

Wireless Train-to-Train Communication

3.1 Overview

To enable ATC, a wireless T2T communication system with ranging capabilities is required. This communication system must be capable of exchanging data between train wagons reliably and at ultra-low latency during the ATC maneuver. During the ATC maneuver, one wagon is assigned the leader role while the other wagon acts as the follower. The leader receives the velocity of the follower and the estimated distance between the two wagons calculated by the follower. Based on the received packets and comparing them to its own calculations, the leader commands the follower to increase, decrease, or maintain the current velocity, according to the specific situation. To make this interaction seamless, both wagons must communicate at all times with each other throughout the ATC maneuver. Having coupled, both trains must maintain the communication channel in order to continue exchange control information defined by the TCN standards as described in the previous chapter. A more detailed description on the interaction between the train wagons during the ATC maneuver is provided in Chapter 6.

In this chapter, we show that standardized communication systems are not

capable of fulfilling the requirements to successfully perform a ATC maneuver. Therefore, a Single Carrier with Frequency Domain Equalization (SC-FDE) wireless communication system based on the SBDist communication system is proposed to enable URLLC during the ATC maneuver and to maintain communication after the train wagons are coupled. PER performance of the proposed communication system is evaluated in this chapter. Moreover, various redundancy schemes and a novel antenna design, namely the CPA, are studied to enhance the performance of the proposed communication system.

3.2 Communication System Structure

Standardized communication systems such as LTE-R and GSM-R are not suitable for ATC because they cannot fulfill the latency and reliability requirements. It is required that the communication system maintains the update rates required by WTB. Therefore, an update rate of at most 100 ms during the ATC maneuver and 25 ms when the trains are coupled must be guaranteed by the communication system. LTE-R based systems provide reasonable throughput performance but registration time, round trip time, and PER performance do not fulfill the requirements for the ATC maneuver to succeed [SKCK16]. LTE-R provides end-to-end delay of up to 250 ms, which is not low enough to enable ATC. LTE-R systems use narrow bandwidth and they do not have a direct D2D communication mode. Hence, all the traffic must be routed through the access and core network to reach the destination causing unnecessary delay. Not only does narrow bandwidth affect latency and reliability negatively, it also affects the ranging accuracy. The relationship between bandwidth and ranging accuracy is explained in more detail in Chapter 5.

IR-UWB based systems use wide bandwidth but the specifications denote that the transmit power must be within the noise level of other systems operating at the same frequency band to avoid interference. The low power limitation means that IR-UWB is only suitable for applications where the distance between the transceivers is very short such as body area networks [XGPJ11].

To overcome the limitations of standardized communication systems, a novel communication system is introduced in this chapter. The proposed system is based on the SBDist system which utilizes a wide band and operates in the ISM mm-Wave band expanding from 61 to 61.5 GHz. The SBDist system utilizes low complexity SC transmitter and receiver design because when the wagons are coupled, the channel is static and a low complexity SC system provides good PER performance as described in [SSS+17]. However, during an ATC maneuver, a dynamic channel is expected where channel estimation and equalization schemes are needed to maintain low PER. Hence, we propose an extension to the SBDist physical layer design to enable channel estimation and equalization. The proposed system uses SC-FDE physical layer architecture. SC-FDE is used instead of the standard favored Orthogonal Frequency Division Multiplexing (OFDM) because SC-FDE has a better peak-to-average power ratio and the transmitter structure is less complex. It is also advantageous to use SC-FDE because it is possible to switch to SC communication system when the train wagons are already coupled in order to transmit control information at minimal latency fulfilling the WTB requirements [SSK+19].

The block diagram of the proposed mm-Wave SC-FDE system is shown in Figure 3.1. The modifications done to the SBDist system are highlighted with grey background. In the following, the blocks used to create the proposed mm-Wave SC-FDE system are described.

Zero Padding and Convolutional Coding

The received control data is zero-padded and and is structured into short packets with length 256 bits each. Although encoding short packets results in a worse PER compared to long packets, the use of short packets is necessary due to low latency requirements. A convolutional encoder with coding rate 1/4 is used to encode the control data outputting a total of 1024 coded bits. Convolutional encoders were chosen because they are less complex than other encoding methods and provide comparably good performance for short packets [SWJ+16].

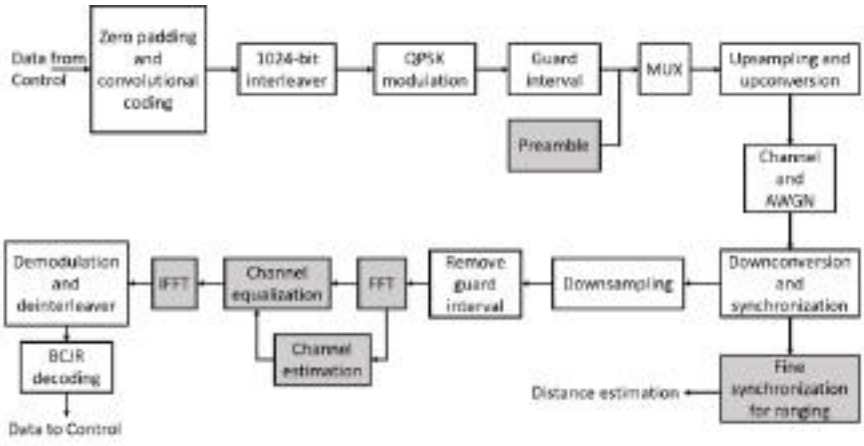

Figure 3.1: The block diagram of the physical layer transmitter and the receiver chains for the proposed SC-FDE system.

1024-bit Interleaver

The wireless signal between two wagons could adhere a fading dip. As a consequence, a large number of successive bits are strongly attenuated. A normal code usually cannot correct a large number of consecutive errors. Therefore, a block interleaver is used to spread the bits apart and decrease the probability of consecutive errrors. The output of the convolutional encoder is input to a 1024-bit block interleaver. This interleaver follows the ETSI 3GPP UMTS specification [ETS15].

QPSK Modulation

The output of the interleaver is modulated. Quadrature Phase Shift Keying (QPSK) modulation is used for ATC. The output frame from the modulator consists of 512 complex In-phase and Quadrature (IQ) symbols.

Guard Interval

A cyclic prefix with a length equal to 1/8 of one frame (64 symbols) is added to the beginning of each frame to form a frame with a total length of

576 QPSK symbols. Cyclic prefix is added to ensure that symbols do not interfere with each other. This is also known as inter-symbol interference.

Preamble

A preamble is multiplexed and transmitted together with the QPSK data symbols. The preamble has two different uses at the receiver: time synchronization and channel estimation. In one hand, Golay complementary sequences are used for time synchronization. Golay sequences have advantageous properties and provide superior performance compared to Pseudo Noise sequences.

Two sequences **a** and **b** form a Golay complementary pair if the sum of their aperiodic autocorrelation functions is an impulse function. The aperiodic autocorrelation function $C_a(\tau)$ of a sequence $\mathbf{a} = (a_1, a_2, ..., a_N)$ is defined as

$$C_a(\tau) = \sum_{n=1}^{N-\tau} a_n a_{n+\tau} \tag{3.1}$$

and sequences $\mathbf{a} = (a_1, a_2, ..., a_N)$ and $\mathbf{b} = (b_1, a_2, ..., b_N)$ form a Golay complementary pair if $C_a(\tau) + C_b(\tau) = 0$ for any $\tau \neq 0$. The Golay complementary sequences used in the proposed SC-FDE system are similar to the suggested sequences by the mm-Wave IEEE 802.15.43c standard [IEE09].

In the other hand, Zadoff-Chu sequences are used for channel estimation [Chu72]. Zadoff-Chu sequences exhibit several useful properties making them a good candidate for channel estimation. Cyclically shifted versions of a Zadoff-Chu sequence are orthogonal to one another. Also, Zadoff-Chu sequences have constant amplitude zero autocorrelation wave-forms. Zadoff-Chu sequences are therefore excellent candidates for the proposed SC-FDE system and provide better PER performance compared to pseudo-noise sequences [AZSK19].

Upsampling

Upsampling is performed by the Digital to Analog Converter (DAC). A Finite Impulse Response (FIR) filter is used to upsample each IQ symbol. The pulses used for the proposed SC-FDE system are Root-Raised Cosine (RRC) pulses. The impulse response of the RRC pulses follows the equation [KD18]

$$h(t) = \begin{cases} \frac{1}{T_s}\left(1+\beta\left(\frac{4}{\pi}-1\right)\right), & t=0 \\ \frac{\beta}{T_s\sqrt{2}}\left[\left(1+\frac{2}{\pi}\right)\sin\left(\frac{\pi}{4\beta}\right)+\left(1-\frac{2}{\pi}\right)\cos\left(\frac{\pi}{4\beta}\right)\right], & t=\pm\frac{T_s}{4\beta} \\ \frac{1}{T_s}\frac{\sin\left[\pi\frac{t}{T_s}(1-\beta)\right]+4\beta\frac{t}{T_s}\cos\left[\pi\frac{t}{T_s}(1+\beta)\right]}{\pi\frac{t}{T_s}\left[1-\left(4\beta\frac{t}{T_s}\right)^2\right]}, & \text{otherwise} \end{cases} \tag{3.2}$$

where β is roll-factor and equals 0.25 and T_s is symbol duration.

Channel and AWGN

After upsampling and upconversion, the signal is transmitted through a mm-Wave channel from the transmitter to the receiver. A realistic channel model must be used to evaluate the performance of the communication system. Therefore, a geometry-based stochastic two-ray channel model is used. The two rays are the Line-of-Sight (LoS) signal and the Ground-Reflected (GR) signal as shown in Figure 3.2. The assumption of only having two dominant rays at the receiver is only valid if highly directional antennas are used. Highly directional antennas are appropriately used in the ATC application as both transmitter and receiver antennas can be mounted on the front of each wagon (on top of the couplers for example). In Chapter 4, mm-Wave propagation measurements will be described and we will show that a two-ray channel model is a good approximation by evaluating the propagation measurements data. The channel impulse response representation is

$$h(t) = a_{\mathrm{LOS}}\delta(t-\tau_{\mathrm{LOS}})\,e^{-i2\pi f_c\tau_{\mathrm{LOS}}} + a_{\mathrm{GR}}\delta(t-\tau_{\mathrm{GR}})\,e^{-i2\pi f_c\tau_{\mathrm{GR}}}, \tag{3.3}$$

where a_{LOS} and a_{GR} are the amplitudes of the LoS and the GR components, τ_{LOS} and τ_{GR} are the delays of the LoS and the GR components, and f_c is the carrier frequency.

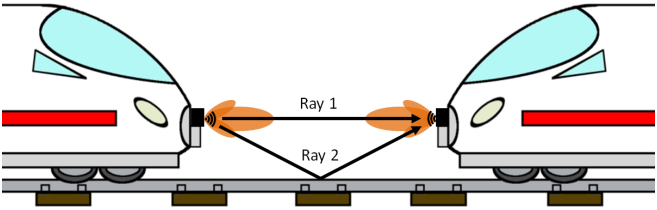

Figure 3.2: An illustration of the two-ray channel between two train wagons. The first ray is the LoS signal and the second is the GR signal.

Downconversion and Synchronization

The first thing that happens at the receiver once a signal is detected is to down-convert the received signal from the mm-Wave band to baseband. The baseband signal is run through a RRC filter and is afterwards converted to a digital signal using a DAC. The analog signal is convoluted with a recorded complementary Golay sequence and a peak search is performed. If the peak crosses a predetermined threshold, the receiver confirms the detection of a signal and the start of reception is triggered.

Downsampling

At the receiver, after the signal is detected and down-converted, if synchronization is successful, the received signal is down-sampled and the guard interval is removed.

Channel Estimation and Equalization

Channel estimation and equalization are performed in the frequency domain using Fast Fourier Transform (FFT) of size 512. Here, the Chu sequence part of the preamble is used for channel estimation and noise estimation. After the channel is estimated, Minimum Mean Square Error (MMSE) method is used for equalization.

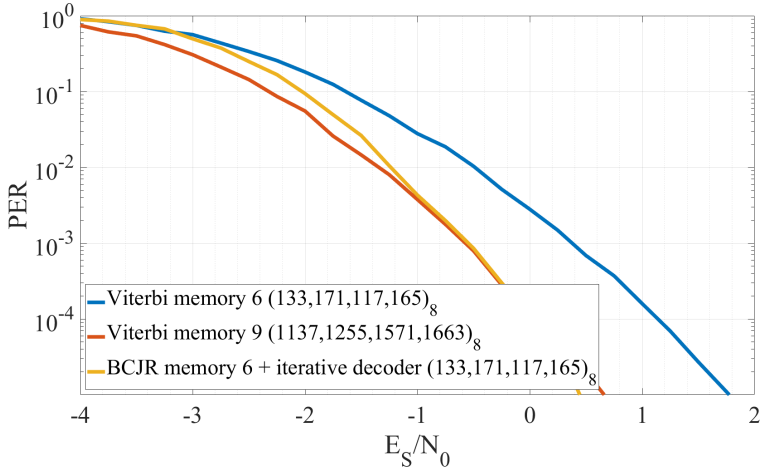

Figure 3.3: Performance comparison of three different convolutional code decoders.

Demodulation and Deinterleaver

After equalization, the received data is transformed to the time domain using Inverse Fast Fourier Transform (IFFT) of size 512 and a QPSK demodulator is used to estimate 1024 bits from the 512 QPSK symbols. A deinterleaver of size 1024 is used at the receiver to correctly rearrange the received bits.

Viterbi Decoding

Finally, a maximum a posteriori decoder is used to decode the data and the output 128 bits are transmitted to the control system. The performance of three decoders is compared in Figure 3.3. The results show that, while BCJR decoders perform better than Viterbi decoders, the gain is low and Viterbi decoders provide the best trade-off when considering complexity. Therefore, Viterbi decoders with a memory value of six are used to minimize the processing delay and complexity.

3.3 Communication System Performance

To evaluate the performance of the proposed SC-FDE system, Monte-Carlo simulations were performed using MATLAB program. In the aforementioned simulations, random data stream is generated, In each iteration, a frame consisting of 1 preamble sequence and 1000 data packets is transmitted through a Additive White Gaussian Noise (AWGN) channel. After the received signal is synchronized, equalized, and decoded, each packet is compared with the original transmitted packet and PER is calculated. The simulations are repeated for different received power values and, hence, different Signal-to-Noise Ratio (SNR) values. To have enough statistics, the amount of data packets transmitted is at least 2 orders of magnitudes higher when compared to the reciprocal of the corresponding PER value. For example, to have enough statistics in simulating PER of 10^-6, at least 10^8 packets are transmitted [LG07].

In order to perform the simulations in a considerably short time frame, the MATLAB Parallel Computing Toolbox was utilized and an efficient code was written. The code allowed the execution of each loop in under 1.5 s allowing us to simulate extremely low PER values. The results of the Monte-Carlo simulation are shown in Figure 3.4 and are compared to the theoretical channel coding lower bounds for convolutional encoders and viterbi decoders [ZW87]. The simulation results show that SC-FDE theoretically achieves low PER values if the SNR value is larger than 4 dB. SC-FDE have worse performance compared to the optimal lower bounds as expected, but the results show that there is room for performance improvement. In the next two sections, we propose two ways to enhance the PER performance of the proposed SC-FDE system when considering a two-ray channel model.

3.4 Circularly Polarized Antennas

Two multipath components are expected to provide the majority of the contribution to the channel, one is the LoS ray and the other is a GR ray as visualized in Figure 3.2. The time difference between the first and the second component is considerably small. This means that both signals will overlap at the receiver and constructive or destructive interference will occur

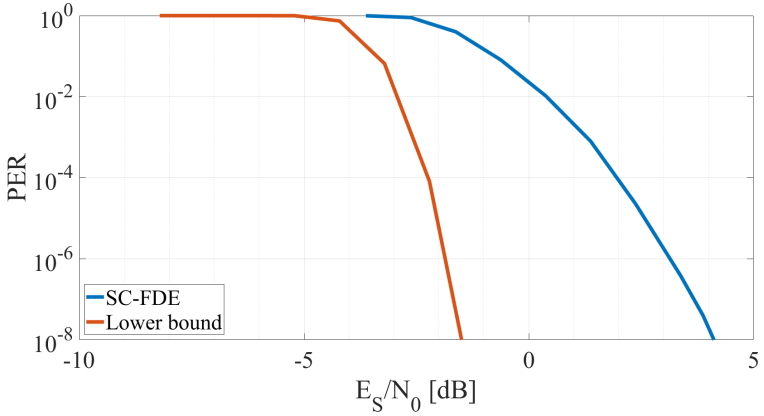

Figure 3.4: PER versus SNR for SC-FDE at a AWGN channel. The results are compared to theoretical optimal lower bounds.

based on the phase difference. Destructive interference will affect the PER performance negatively and the equalizer won't be able to mitigate the rapid variation in the received signal power due to the fast phase changes. To decrease the contribution of the GR signal, innovative solutions were studied.

One of the proposed solutions is to use CPA ([MLLC14], [WCF16], and [YSG20]). The CPA designs studied in this work are antenna arrays which are arranged specifically to manipulate the received signals based on their reflection order [ABAH18]. CPAs consist of four sub-arrays. Each of them consists of four truncated-corner patch antennas which are fed by a sequentially-rotated feeding network to enhance the axial ratio over frequency as illustrated in Figure 3.5a.

Signal components which undergo even number of reflections, including the LoS signal, are subject to a different antenna pattern when compared to signals which undergo an odd number of reflections. In other words, the LoS signal will be affected by a different antenna pattern to that of the ground reflected signal. This is desirable because the interference caused by ground reflected signal can be suppressed if the antenna is designed to produce higher gain for the LoS signal compared to that of the GR signal. A CPA having the aforementioned desirable properties is proposed for a T2T wireless

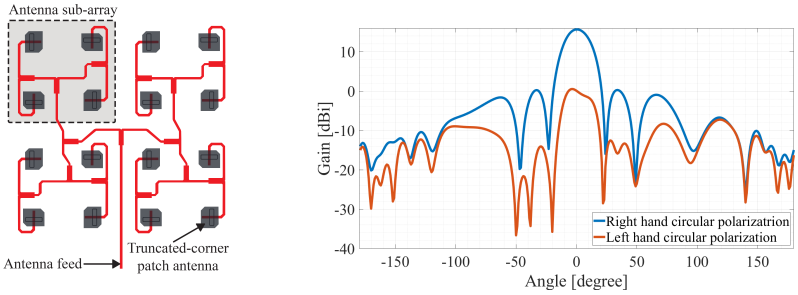

Figure 3.5: (a) Design of the CPA array. (b) Antenna patterns of the CPA for even- and odd-reflected incident signals [SSS+17][ABAH18].

communication system at the mm-Wave frequency domain [SSS+17]. The antenna pattern is shown in Figure 3.5b. The right hand circular polarization is the pattern affecting the LoS signal and it provides a 3 dB beamwidth of 20° for the main lobe. The left hand circular polarization is the pattern affecting the ground reflected signal. Therefore, if both transmitter and receiver are equipped with CPA, the received LoS signal will undergo up to 18 dBi power gain more than the GR signal.

To analyze the benefits of CPA, PER Monte Carlo simulations are carried out to compare the performance of the transceivers using CPA against transceivers using mm-Wave horn antennas. The horn antennas used in the simulation provide the same gain value at 0° for the main lobe compared to the CPA. In the PER simulations, the transmit power is set to 10 dBm. Figure 3.6 shows the PER performance at each separation distance between the transceivers. In these simulations, we assume that the LoS and GR signals always overlap at the receiver. This assumption is valid due to the geometry of the T2T channel where the incident angle between the two signals is small, i.e. both lie within the main lobe.

The PER results show that using horn antennas will cause severe PER variations which, in order, will negatively affect the ATC maneuver. In the other hand, CPA minimize the variations while maintaining the overall PER performance [SSK+19]. Therefore, CPA can successfully mitigate the

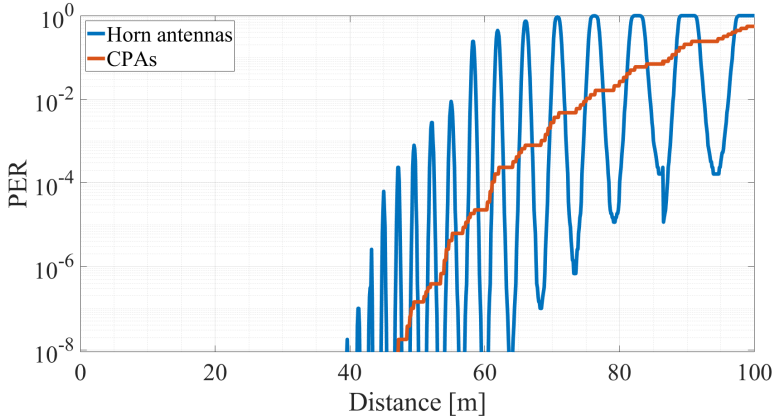

Figure 3.6: PER of the SC-FDE system using horn antennas vs. CPA. PER values are simulated for each separation distance between the train wagons.

contribution from the ground reflected ray in a two-ray channel model.

3.5 Redundancy

Redundancy is a familiar concept for wired safety critical systems. For example, current railway control systems exchange information between wagons through the couplers using gold-plated bins as shown in Figure 3.7. These communication bins are physically redundant where a set of bins on one side transfers the exact same information as the set of bins on the other side. Redundancy provides robustness against physical damage and decreases error rate values [SSK+19].

To provide better PER performance and robustness against physical damage, redundant SC-FDE transceivers are investigated for ATC. Redundancy is implemented by attaching two SC-FDE transceivers to each wagon where both transceivers are transmitting and receiving the same information to and from the wagon. The set-up top view is shown in Figure 3.8a.In that setup, each pair of transceivers is exchanging the exact same control data and this allows the system to have redundancy against physical damage

Figure 3.7: Photos of two different train coupler types showing electrical wired communication interfaces to transfer safety critical control data between wagons.

(a) **(b)**

Figure 3.8: Top view of two train wagons. (a) Each wagon has two transceivers to provide redundancy. (b) Cross-communication is enabled to further enhance PER performance.

and physical blockage. Furthermore, PER enhancement can be enhanced by using diversity combining schemes, especially if the channels between each pair are considered mutually independent.

To further enhance PER performance, cross-communication between the transceivers is investigated. Redundancy with cross-communication is shown in Figure 3.8b where each receiving transceiver receives data from the adjacent transceiver as well as from the crossing transceiver. This provides a noticeable PER enhancement because four independent redundant data signals are received in total. To enable cross-communication, the two transmitters Tx1 and Tx2 are assumed to use FDD. Hence, the transmitters use two different carrier frequencies.

To analyze the performance enhancement provided by redundancy, PER

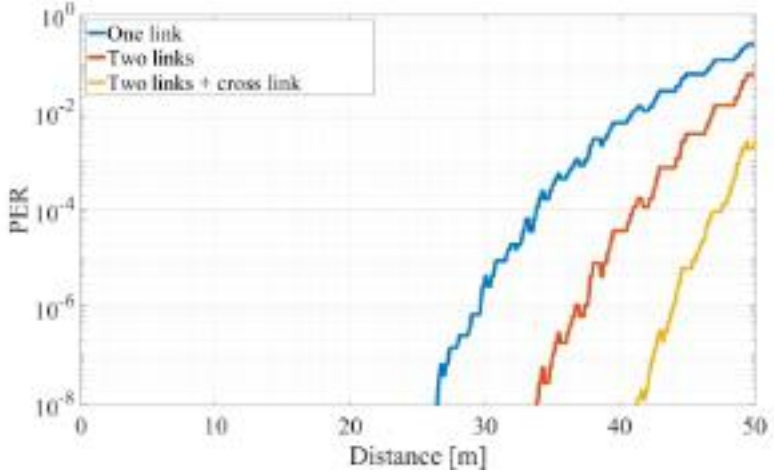

Figure 3.9: PER of SC-FDE system using CPA in a two-ray channel. One link is compared with two links sending redundant data and four links by enabling cross communication.

evaluation was performed using the proposed SC-FDE communication system. CPA were used to mitigate the variations caused by the two-ray channel. The results are shown in Figure 3.9. We assumed that the channels are mutually independent. This assumption simplifies the simulations. The results show that, while the two redundant links enhance the PER performance, allowing cross-communication between the transceivers noticeably enhances the PER values compared to having one or two parallel redundant links. More importantly, the presented PER results show that it is possible to enhance the performance of the proposed wireless mm-Wave SC-FDE systems for ATC by using CPA and redundancy.

3.6 Summary

In this chapter, a mm-Wave SC-FDE communication system is introduced to enable ATC. The proposed system is based on the SBDist system proposed to enable wireless WTB communication. The proposed system extends the SBDist system by using frequency domain equalization and fine synchroniza-

tion for ranging. The communication system is responsible of exchanging control information between the two train wagons involved in the ATC maneuver. Furthermore, the performance of the communication system is evaluated using Monte-Carlo simulations.

Two approaches are proposed to enhance the performance of the communication system. The first approach is to use CPAs to decrease the negative influences of unwanted multipath components. The second approach is to use redundancy to provide physical redundancy and to enhance the PER performance. The simulations show that the two approaches provide noticeable improvements and allow ultra-reliable communication throughout the ATC maneuver.

Chapter 4

mm-Wave Train-to-Train Channel Characterization

4.1 Overview

Since ATC requires communication over short distances, the ISM bands are good candidates for such an application. As described earlier, a bandwidth of 500 MHz is required to meet latency and reliability requirements. Conveniently, the 61 to 61.5 GHz frequency range is reserved for ISM applications. Therefore, a mm-Wave SC-FDE T2T communication system operating in the ISM band at 61.5 GHz, namely the SBDist communication system, is proposed to enable ATC.

4.2 mm-Wave Channel Characteristics and Literature Review

By definition, the mm-Wave band spectrum extends from 30 GHz to 300 GHz because the wavelengths in this frequency range are on the order of millimeters, hence the name. Some standards extend the mm-Wave band spectrum to lower frequencies. For example, the 5G mm-Wave spectrum is at 26 GHz.

There are several advantages to using the mm-Wave frequency bands. First,

there is plenty of available spectrum for short-range communication systems in the mm-Wave frequency band compared to the extremely congested sub-6 GHz band.

Second, there is less interference in the mm-Wave frequency band because the spectrum is less congested but the path loss is high compared to the sub-6 GHz bands. As the wavelength decreases, the reduction in power density increases, as shown by the equation for free-space path loss

$$PL_{\text{fs}} = 20 \log \left(\frac{4\pi d}{\lambda} \right), \tag{4.1}$$

where PL_{fs} is the free-space path loss in dB, λ represents the signal wavelength, and d is the distance between the transmitter and the receiver. While this is considered a disadvantage in other applications, high path loss means that intelligent frequency allocation and spectrum sensing techniques are not required for operation in the mm-Wave band due to natural spatial diversity.

Third, mm-Wave signals have higher energy efficiency when compared to sub-6 GHz signals. The authors of [AKIR16] indicated that the amount of energy required to transmit information at a given Signal to Interference Noise Ratio (SINR) value is lower at 60 GHz central frequency compared to 2 GHz central frequency in a LoS environment. Finally, mm-Wave components, especially the mm-Wave antennas, have a smaller physical footprint. The size of the antennas is proportional to the wavelength of the signal. Therefore, it is possible to fabricate mm-Wave antenna arrays that consist of multiple antenna elements and have a very small footprint. For example, the CPAs presented in chapter 3.4 have 16 (4x4) elements and their total size is 12x12 mm^2 [ABAH18].

Communication systems operating in the mm-Wave frequency band are promising, but need further investigation to enable accurate evaluation of the communication systems operating at the corresponding mm-Wave frequency band. For this purpose, mm-Wave channel models are needed. The mm-Wave channel is being studied in depth in various 5G mobile environments, such as indoor environments ([WWS+17], [ZQZ+19], [MRSD15], [VZF+18]) and urban outdoor areas ([AWW+13], [RBDMQ12], [KCH+17]). Several Car-to-Car measurements have been performed. These measurements have

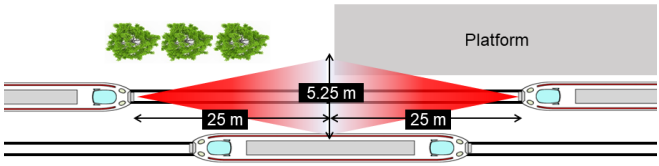

Figure 4.1: Top view illustration of two train wagons communicating using highly directive antennas.

been described in [HSA+20]. All measurements are exclusively performed in vehicular environments such as parking lots and urban roads, and none of them are suitable for use in the railways environment.

In the field of trains, channel measurements have been performed at frequencies below 10 GHz. The authors in [UPS+16] listed all published railroad measurements in recent years. The authors in [GAP+18] describe the different scenarios in which railroads could benefit from mm-Wave 5G communications. The authors also conclude that there is a lack of mm-Wave measurements in the railroad sector. Although this is true, some static measurements have been performed to investigate the intra-wagon mm-Wave channel [GPH+21]. Although the measurements are recent, they cannot be used for the ATC scenario because the environments are different.

Figure 4.1 shows an illustrated top view of the environment of two train wagons while performing an ATC maneuver. While the proposed mm-Wave ATC communication system employs highly directional antennas, there is a possibility of contribution from the environment to the mm-Wave T2T channel. The 3 dB beam opening is 5.25 m if the distance between the two wagons is 50 m. This means that a nearby platform, a wagon in a parallel track, vegetation, or even the metallic track bars might affect the mm-Wave channel. Therefore, mm-Wave propagation measurements are required to study the channel in a realistic environment using moving train wagons.

Due to the lack of literature in this field, under the collaboration with the university of RWTH Aachen, mm-Wave T2T propagation measurements

were performed. In the upcoming sections, we will describe the hardware we used, the measurements, and the analysis of the recorded measurement data.

4.3 mm-Wave Channel Measurements

4.3.1 Hardware Setup

To perform the mm-Wave propagation measurements, hardware for channel sounding is required. Most of the necessary hardware is available at the DLR Institute of Communications and Navigation, since many channel measurements have been performed by the institute in various environments. For example, ship-to-ship [WJRF17], car-to-car [WFZ14][JJL+21], train-to-train [USS+17], and air-to-air measurements [BS19] were performed. All these measurements were carried out with the DLR RUSK channel sounder at sub-6 GHz carrier frequency. The DLR RUSK Channel Sounder consists of an accurate signal generator at the transmitter and a real-time data grabber at the receiver. Two highly accurate rubidium atomic clocks from Temex Time [Tem] were used to synchronize the channel sounder transmitter and receiver. The bandwidth of the channel sounder is 120 MHz and it can operate at various carrier frequencies up to 5.2 GHz. During the measurements discussed in this chapter, the channel sounder was set to use the parameters listed in Table 4.1.

Parameter	**Value**
Center frequency	3.5 GHz
Bandwidth	120 MHz
Maximum delay	12.8 µs
Time grid	1.024 ms
Transmit power	0 dBW

Table 4.1: Parameters of the DLR RUSK channel sounder.

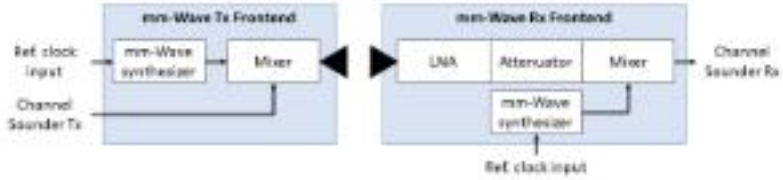

Figure 4.2: A block diagram of the mm-Wave transmitter and receiver front-ends.

The DLR RUSK channel sounder provides good channel sounding performance for frequencies below 6 GHz. To perform mm-Wave channel measurements, the output signal of the channel sounder must be converted to a mm-Wave signal. Therefore, we have built mm-Wave transmitter and receiver front-ends that can be integrated with the DLR RUSK channel sounder. The block diagram of the front-ends is shown in Figure 4.2. The transmitter front-end accommodates two inputs. The first input is the channel sounder signal and the second input is the clock reference to synchronize the mm-Wave Local Oscillator (LO) with that of the channel sounder. The input signal is mixed with the mm-Wave LO using a waveguide upconverter. The output of the upconverter is fed into a waveguide horn antenna resulting in a mm-Wave output signal. During the measurements discussed in the following sections, the carrier frequency of the mm-Wave signal was set to 62.5 GHz. This carrier frequency was attained by fixing the LO frequency to 59 GHz. At the receiver, the mm-Wave signal is received by a waveguide horn antenna. The antenna is connected to a Low Noise Amplifier (LNA) and a variable attenuator. The attenuator is used only when both the transmitter and receiver front-ends are connected directly through a waveguide for calibration purposes. The attenuator is otherwise disabled. The attenuator is connected to a waveguide downconverter that mixes the received signal with a signal from a mm-Wave LO. The mm-Wave LO of the receiver is synchronized by the clock of the channel sounder. The output of the downconverter is fed to the receiver of the DLR Rusk Channel Sounder. The receiver filters the signal and downconverts it to baseband. The receiver stores the IQ samples with a time stamp and logs them to allow offline

Figure 4.3: The mm-Wave front-ends housing from the front and back sides.

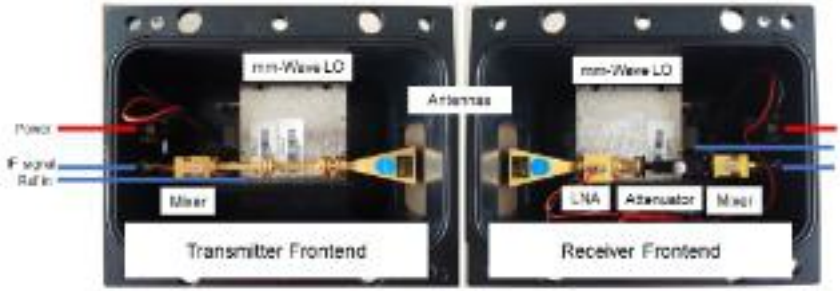

Figure 4.4: The mm-Wave front-end components are accessible from the bottom side of the housing.

processing.

The components of the mm-Wave front-ends are enclosed in steel housing with passive cooling to avoid heat, dust and other undesirable external influences. Synthetic radomes are installed in front of the antennas to allow lossless mm-Wave propagation. The radome materials cause a loss of approximately 0.3 dB to the mm-Wave signals. Figure 4.3 shows the mm-Wave front-ends from the front and back sides. The mm-Wave components are accessible from the bottom side. The components are shown in Figure 4.4.

Figure 4.5: Long-term stability test of the mm-Wave front-ends.

4.3.2 mm-Wave Front-ends Evaluation

To evaluate the performance of the hardware, we performed a series of indoor and outdoor measurements. The measurements included short- and long-term tests in the lab as well as dynamic and static tests outdoors in different environments. One indoor measurement and three outdoor measurements are outlined in the following [SUDPM+18].

Indoor Measurements

Indoor static measurements were performed in the laboratory for approximately five hours to evaluate the long-term stability of the mm-Wave front-end oscillators and to ensure that the devices did not overheat. The performance of the oscillators was monitored using a real-time spectrum analyzer, and the temperature was monitored by the proprietary software of the local oscillators. Figure 4.5 shows the setup used in the laboratory measurements.

Outdoor Static Measurements

Two open-field measurements were conducted in the same environment to determine the maximum range of the mm-Wave Channel Sounder and to compare the received signal power with the free-space path loss model. The main difference between the two measurements was the height of the

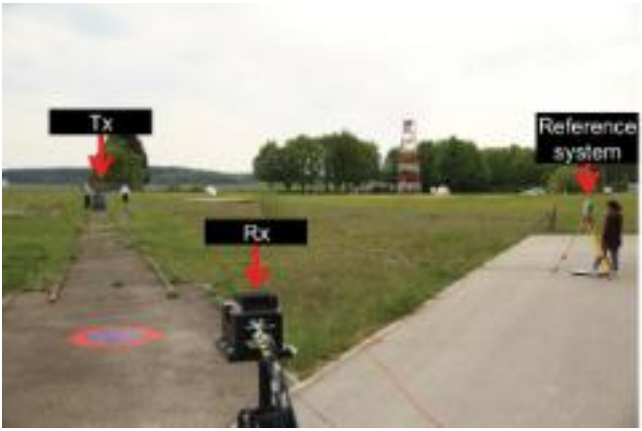

Figure 4.6: Open-field static test of the mm-Wave front-ends.

antennas above the ground. The front-ends of the transmitter and receiver were mounted on tripods. The tripods were 1.28 m above the ground for the first measurement and 2.63 m for the second measurement. More than 5000 samples were recorded at each separation distance in order to have enough statistics to calculate the average received power. After enough samples were collected, the transmitter tripod was moved farther away to take more static measurements. The tripod was moved through an asphalt track as shown in Figure 4.6. The receiver channel sounder was placed stationary at the entrance to the track.

We used a Leica TCRP 1201 tachymeter as a reference system to accurately measure the distance between the front-ends of the transmitter and receiver. For this purpose, we set up the tachymeter next to the track and placed a reflective prism at the transmitting and receiving antennas. The coordinates of the two antennas in an arbitrary coordinate system were subtracted from each other in post-processing to determine the separation distance.

The measurements were performed up to a distance of 110 m. As can be seen in Figure 4.7, the measured received power for both front-end heights matches the theoretical free-space path loss, but there were strong variations, especially at the lower antenna height. These variations are due to multipath effects caused by ground reflections. The measured received power includes

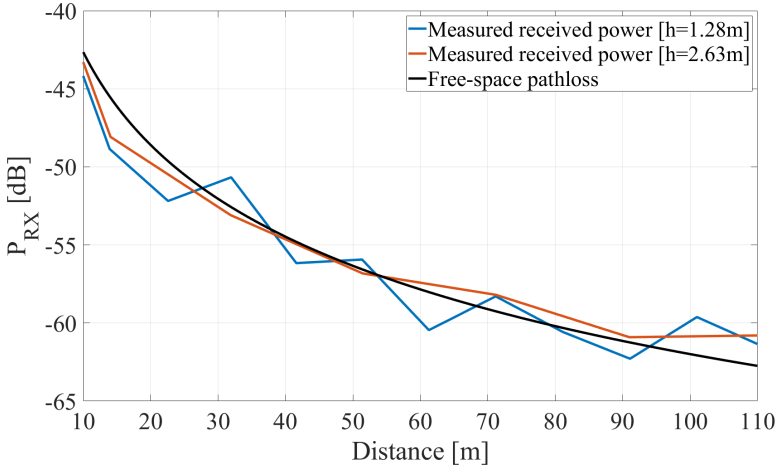

Figure 4.7: Measured received power from open-field static measurement at different antenna heights.

the gain of the transmit and receive antennas. All other gains and losses were calibrated out. At 110 m, the received signal was prominent at 15 dB above the noise floor. Although measurements over longer distances were feasible, the measurements made up to 110 m were sufficient to evaluate the performance of the mm-Wave front-ends.

Outdoor Dynamic Measurements

Dynamic measurements were performed in an open parking lot next to a building, as shown in Figure 4.8, to evaluate the stability of the group delay (phase information) and the influences of multipath. The group delay is particularly useful for estimating the distance between the transmitter and receiver. The front-end of the transmitter was mounted on a tripod and the front-end of the receiver was mounted on a remotely controlled rover as shown in the top left corner of Figure 4.8. The rover was driven in a 2.5 m wide corridor to a distance of 28 m away from the transmitter and then driven back towards the transmitter. On the north side, 10 cars were parked and on the south side, there was a metallic wall 5.6 m away. The

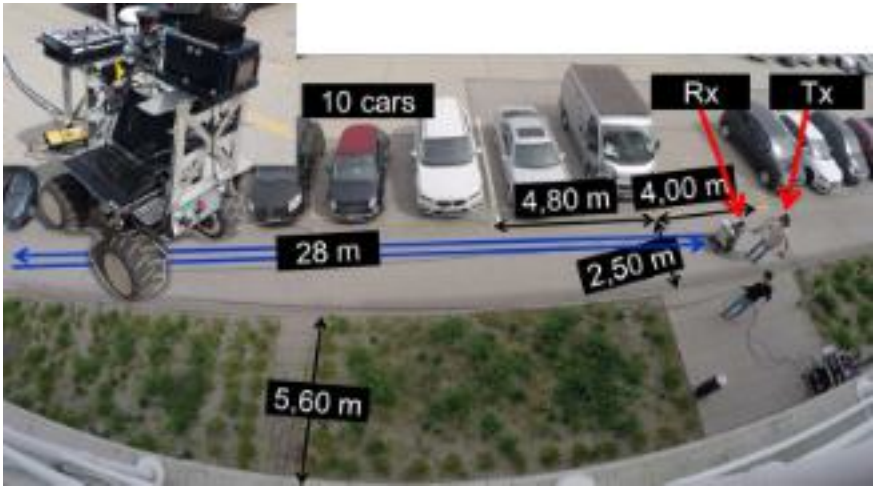

Figure 4.8: A top view shot of the dynamic tests environment. The receiver front-end was mounted on top of a remote-controlled rover (top-left corner) to enable dynamic measurements.

wall consisted mostly of double-glazed glass windows. Along the route were metal poles spaced 4.8 m apart. The initial distance between the tripod and the rover was about 4 m. The Leica tachymeter reference system was also used to determine the distance between the tripod and the rover.

Figure 4.9a shows the estimated distance between the tripod and the rover based on the measured group delay (phase slope) throughout the recorded measurement duration. The recorded measurement lasted for about 270 s. The plot shows good agreement between the estimated distance and the reference distance from the Leica up to about 100 s, when the distance between the front-ends is 15 m. The estimated distance is not affected by multipath components. At longer distances, the effects of multipath components due to ground reflections as well as reflections from the vehicles and the poles lead to increasing errors in the distance estimates based on the phase slope. A moving average filter is used to decrease the influence of multipath components.

Figure 4.9b shows the received power from the same measurement compared to the theoretical free-space path loss. The variations at the short

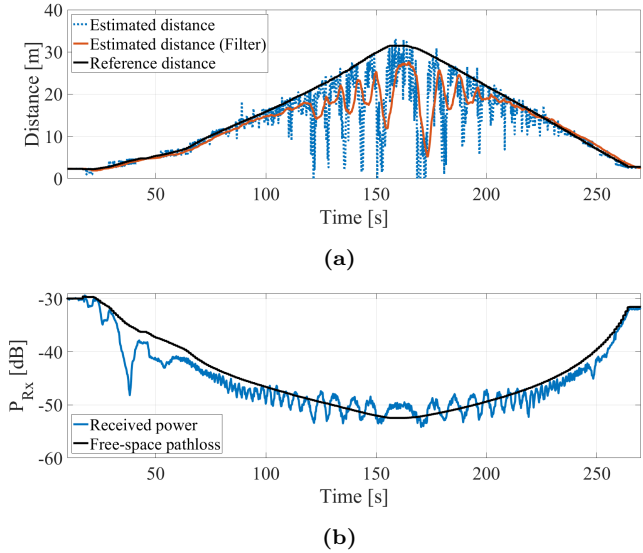

Figure 4.9: **(a)** Estimated distance between the transmitter and receiver compared to the reference distance. **(b)** Received power at the mm-Wave front-end receiver compared to theoretical free-space path loss.

distances up to 50 s are due to the misalignment of the highly directional antennas during the rover's departure. This misalignment resulted in significant drops in the received power, but the delay estimate in the same period is unaffected. With increasing distance, the contribution of multipath effects increases, resulting in variations in received signal power due to alternating constructive and destructive interference. The measured received power includes the gain of the transmit and receive antennas, which is 23 dB each. All other gains and losses have been calibrated out.

4.3.3 Measurement Campaign

After the evaluation of the mm-Wave front-ends, a channel measurement campaign was carried out on the premises of the Institute of Rail Vehicles and Transportation Systems at RWTH Aachen University. The Y-shaped tracks shown in Figure 4.10 are about 300 m long. The tracks are well suited

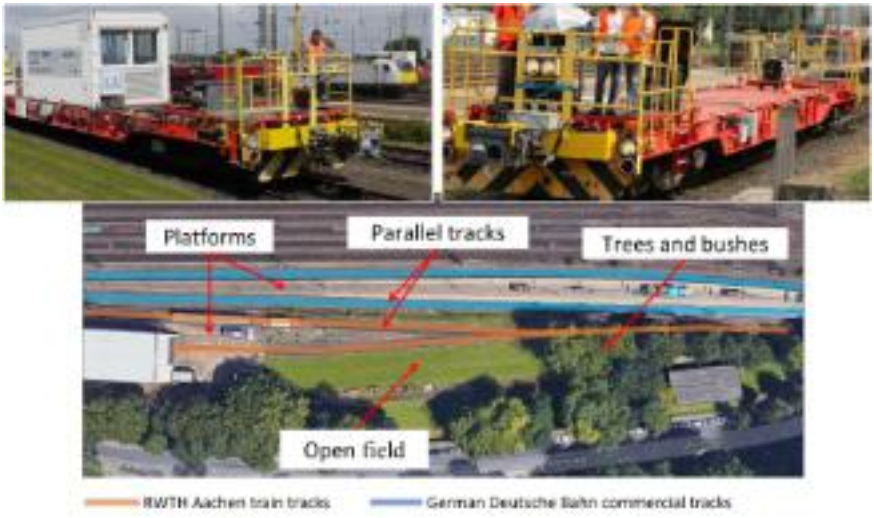

Figure 4.10: The two experimental trains used in the measurements and top view of the train track located on the premises of RWTH Aachen University [IFS].

for channel measurements because different environments are present in the various sections. These include open field, platform, trees and bushes, and the ability to make measurements when trains pass through a parallel commercial track.

The measurements were performed with two experimental self-propelled freight wagons from the institute of Rail Vehicles and Transport Systems at RWTH Aachen University. The wagons are shown in the top of Figure 4.10. The wagons were equipped with diesel generators to power the channel sounder, mm-Wave front-ends, desktop computers, and all other equipment on board. Both carriages were equipped with Scharfenberg couplers on which flat metal plates were mounted for easy mounting of the mm-Wave front-ends (see Figure 4.11). Other devices were used during the measurements such as a Leica tachymeter, two high resolution vibration sensors, and two Universal Software Radio Peripheral (USRP) devices to test a prototype control system using wireless communications based on the proposed SC-FDE system [SSS+17]. The Leica TCRP 1201 tachymeter was used as a

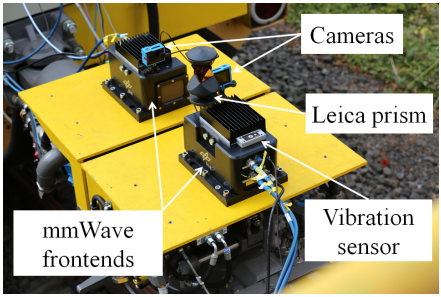

Figure 4.11: mm-Wave front-ends, Leica prism, and vibration sensors installed on the train couplers.

reference system to accurately measure the distance between the transmitter and receiver front-ends. To this end, the tachymeter was placed next to the track in different locations based on the environment section. A reflecting prism was mounted on top of the front-ends. The setup of the front-ends and the prism is visualized in Figure 4.11. One train wagon was static during the measurements and the other train was approaching and disengaging to emulate a ATC maneuver. Hence, the position of the static train was measured only once in the beginning of each measurement and the position of the moving train was tracked during the measurements. We also measured the location of different objects and landmarks. A highly accurate measurement in the order of millimeters can be expected with this setup.

Furthermore, to record any influences from the surroundings and to analyze any unpredictable behaviors, we installed four Garmin sport cameras. Two cameras were installed on top of the front-ends, one on the top of the Leica Tachymeter and one was installed further away to have a wide view of the track and both trains. The cameras have built-in sensors that included 10 Hz High-sensitivity GPS receiver, accelerometer, and other sensors. This allowed us to obtain synchronized and time-stamped recordings. Throughout the measurements, the channel sounder and the mm-Wave mm-Wave were set to generate a signal with a carrier frequency of 62.5 GHz.

Throughout the campaign, our focus was on the ATC maneuver, where one wagon is uncoupled from the rest of the train and moves away, or vice versa, where one wagon moves towards the other wagon until they are physically

coupled. In ATC, the relative speed between trains is low, especially when they get close to each other. Therefore, the relative speed between the trains was below 6 km/h throughout the measurements.

Environment	Number of measurements
Open field	6
One metallic sheet	4
Two metallic sheets	4
Next to a platform	6
Trees and bushes	4
Train on parallel track	2
Transition maneuvers	4

Table 4.2: Environments and number of measurements covered throughout the mm-Wave T2T channel measurement campaign

A total of thirty measurement sessions were recorded during the campaign, including fourteen coupling and fourteen uncoupling measurements. Two measurements were recorded when both trains were stationary while a third train was traveling on a parallel track. The environments recorded are summarized in Table 4.2. For each environment, the measurements were repeated 2 to 6 times. The open-field environment is the middle section shown in Figure 4.10. The environments with one and two metal sheets are located in the same section as the open field, but the metal sheets were placed next to the track to reproduce the reflections caused by surrounding metal objects such as traffic signs or metal pillars. Measurements were also made in the left section of the track, where a platform is located, and in the right section, which is closer to bushes and trees. Two measurements were made as a commercial suburban train passed on a track parallel to the measurement tracks to observe the reflections caused by the suburban train. Transition maneuvers are those recorded during the transition from

one section of track to the next [SUS+19].

4.4 Measurement Data Analysis

4.4.1 Received Power Evaluation

During the measurement campaign, six measurements were performed in the open-field area. The aim of these measurements is to compare them with the theoretical path loss models and to find a good fit for the performance analysis. The received signal power from the open-field measurements was evaluated for each separation distance. The results are shown in Figure 4.12. The gains of cables, amplifiers, splitters, and other components were calibrated prior to the measurements. Therefore, the transmit power of the calibrated recorded data is equal to 0 dBW. The antenna gains, on the other hand, were not calibrated out.

The measured data were compared with the free-space path loss received power,

$$P_r\left(d_1\right) = P_t + G_t + G_r - PL_{\text{fs}}\left(d_1\right) - L_{\text{ox}}\left(f, d_1\right), \tag{4.2}$$

where $PL_{\text{fs}}\left(d_1\right)$ is the free-space path loss with an attenuation exponent value of 2. The gain values of the transmitter and receiver antennas are expressed as G_t and G_r, P_t is the transmitted power in dB, and d_1 is the distance between the transmitter and the receiver front-ends. The loss due to oxygen absorption is given as L_{ox} and depends on the distance and the carrier frequency f. At close range, there is good agreement between the measured received power from the runs and that from the free-space path loss, but the fluctuations in the received signal power increase with distance. The fluctuations are caused by a second multipath component reflected from the ground (railroad track). The influence of the second path becomes stronger with increasing distance because the antenna gains increase as the transmit and receive angles of the multipath components get closer to the antenna bore-sight. We compared the measured received power of the six measurement sessions to a two-ray path loss received power which is expressed as follows:

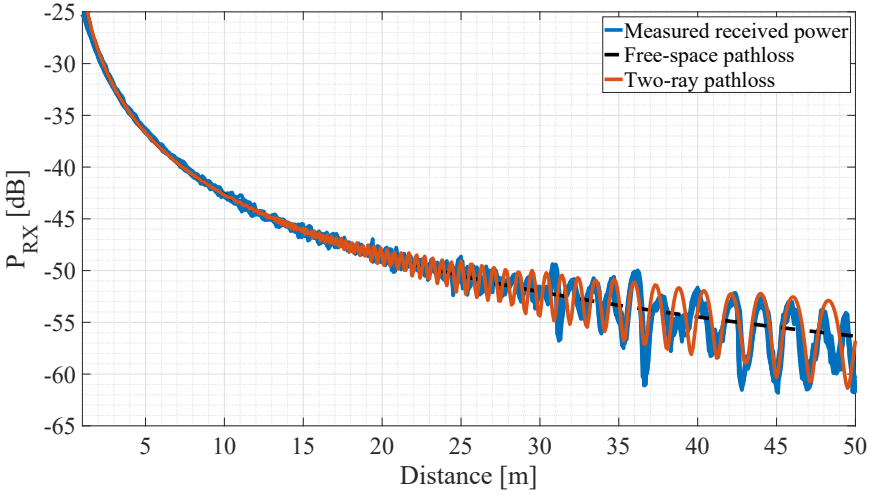

Figure 4.12: Received power from six recorded measurements in the open-field environment compared to theoretical free-space and two-ray path loss.

$$P_r\left(d_1\right) = P_t - PL_{\text{tr}}\left(d_1, d_2\right) - L_{\text{ox}}\left(f, d_1\right) - L_{\text{ox}}\left(f, d_2\right), \tag{4.3}$$

where d_2 is the distance of the second path, $PL_{\text{tr}}\left(d_1, d_2\right)$ is the two-ray path loss [NGAT17] defined as

$$PL_{\text{tr}} = -20\log\left|g_1 \frac{\lambda}{4\pi d_1} e^{-i\phi_1} + g_2 \Gamma_{\text{gr}}\left(\theta\right) \frac{\lambda}{4\pi d_2} e^{-i\phi_2}\right|. \tag{4.4}$$

In the above equation, $\Gamma_{\text{gr}}\left(\theta\right)$ is the GR coefficient, which depends on the angle of incidence θ and the ground material. The phase of the received signals on the LoS and on the GR path is ϕ_1 and ϕ_2, respectively. $g_1 = \sqrt{G_{t,LoS} G_{r,LoS}}$ and $g_2 = \sqrt{G_{t,gr} G_{r,gr}}$ are the LoS and GR antenna gain coefficients, respectively. As expected, the two-ray path loss model is better fit for open-field measurements compared to the free-space path loss. This is plotted in Figure 4.12.

To compare the above results with those of other environments, we plotted the received signal power in one of the open-field measurements, one of the measurements with a metal plate attached to the side, and one of the

Figure 4.13: The environment where the measurements next to the platform were performed. The platform extended for 16 m.

measurements next to a platform. The size of the platform was extended to 16 m, as shown in Figure 4.13. The figure is taken from the moving train. The results of the received power are shown in Figure 4.14. From the results, it can be seen that the received power of the platform measurement is on average 1.35 decibel higher than the other two measurements at short distances up to about 16 m, which is due to the concrete platform next to the track. In contrast, the received power in the measurements at a distance of more than 20 m behaves as in the open field. The reason for this is that, similar to the open field runs, the dominant contribution for all runs at long range comes from the LoS and the paths reflected from the ground. This is confirmed by comparing the received power in the three runs with the received power of the two-ray path loss model.

While the two-ray path loss model is a good fit to the measured data, periodic fluctuations were found in the measured data compared to the two-ray path loss model. For further investigation, the SAGE algorithm was used [FH94], [FTH$^+$99]. SAGE is used to identify and track the most prominent multipath components and their parameters (delay, amplitude, phase, ...) from the recorded channel sounding data. The output of the SAGE algorithm is filtered with a high-pass filter to remove noise. The result of the high-pass filter is shown in Figure 4.15. The figure shows that in addition to the LoS and GR signals, there was another relevant multipath component that traveled almost three times the distance compared to the

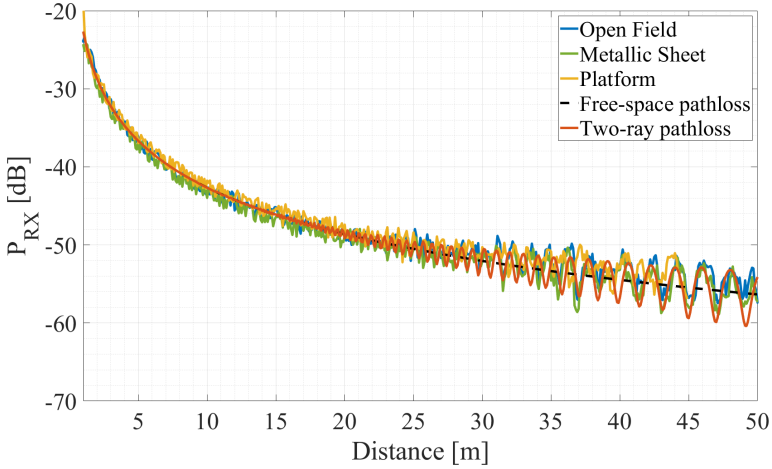

Figure 4.14: The recorded received power in three different environments compared to theoretical free-space and two-ray path loss.

LoS signal. After further investigation, this signal was identified as a double-bounced signal from the train fronts. The train fronts are metallic and are considered good reflectors. Therefore, the double-bounced signal has power of 5 to 15 dB less when compared to the LoS signal.

As a result, a three-ray channel model is proposed to evaluate the performance of the mm-Wave SC-FDE system for ATC. An illustration of the three paths of the proposed three-ray channel model is shown in Figure 4.16 [SUS+19].

The three-ray path loss model is defined as

$$PL_{3\mathrm{r}} = -20\log\left|g_1\frac{\lambda}{4\pi d_1}e^{-i\phi_1} + g_2\Gamma_{\mathrm{gr}}(\theta)\frac{\lambda}{4\pi d_2}e^{-i\phi_2} + g_1\Gamma_{\mathrm{db}}^2(\theta)\frac{\lambda}{4\pi d_3}e^{-i\phi_3}\right|. \tag{4.5}$$

Figure 4.17 shows the theoretical received power using the proposed three-ray path loss model compared with the recorded measured data. The proposed three-ray path loss model agrees with the measurements. The received power of the third path (doubly bounced signal) is considered low

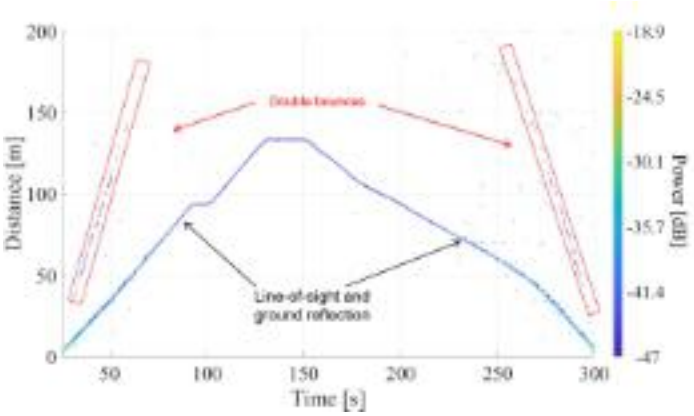

Figure 4.15: The output of the SAGE algorithm performed on one of the open-field measurements. The graph shows the distance covered by each multipath component versus time. The color map shows the received power in dB of each component.

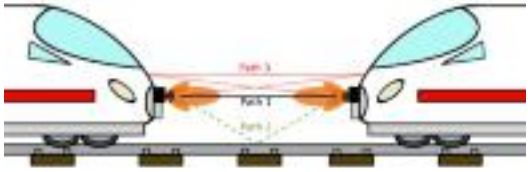

Figure 4.16: An illustration of the three-ray channel model.

enough not to affect the PER performance of the communication system. Therefore, it is ignored when evaluating the performance of the communication system. On the other hand, the knowledge gained by analyzing the mm-Wave T2T channel will be useful to improve the accuracy of estimating the distance between train cars. This will be demonstrated in a later section.

4.5 Summary

In this chapter, a study on various mm-Wave propagation measurements was performed. The study shows that there is a lack of mm-Wave T2T channel

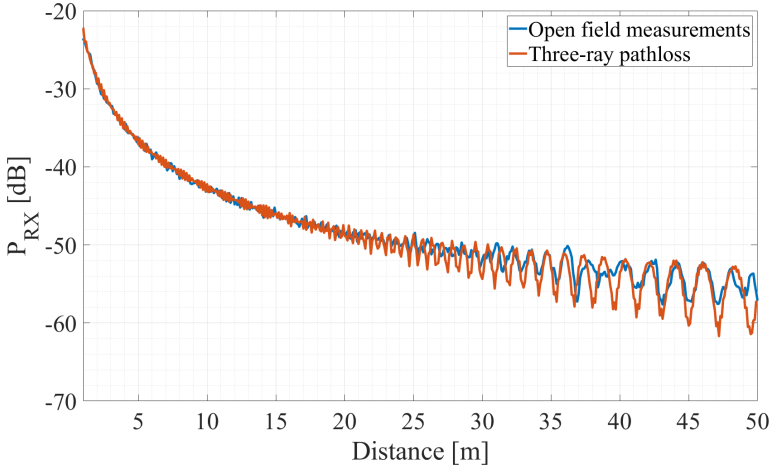

Figure 4.17: Received power from six measurements in the open-field environment. The received power is compared to that of the three-ray path loss model.

models based on dynamic measurements in the literature. Therefore, it was concluded that it is necessary to conduct a mm-Wave T2T propagation measurement.

To conduct the mm-Wave T2T propagation measurement, two mm-Wave front-ends were designed, assembled, and tested. Furthermore, the measurements were carried out on the premises of the Institute of Rail Vehicles and Transportation Systems at RWTH Aachen University using two experimental self-propelled freight train wagons. Recorded measurement data sets were analyzed and were compared to theoretical pathloss models.

The recorded data sets show that a two-ray path loss model fits the measurements. Still, minor deviations were observed when the curves where compared. After further analysis using the SAGE parameter estimation method, it was identified that the deviations were caused by a third path reflected by double bouncing on the train fronts. The received power of the doubly bounced signal is low in comparison to the LoS signal. While this might show no significant effect on the communication system PER values, the next section describes how the doubly bounced signal is used to enhance

the ranging accuracy.

Chapter 5

Distance Estimation

5.1 Overview

Several schemes can be used to estimate the distance between two transceivers. The most commonly used schemes are ToA, RTD and Time Difference of Arrival (TDoA).

Consider two train wagons, Wagon A and Wagon B. It is necessary to estimate the distance between them to enable ATC. The use of ToA requires one transceiver at Wagon A and one at Wagon B. Wagon A has to send time-stamped messages to Wagon B. Wagon B receives a time-delayed version of the message $s[n]$, as denoted by

$$r[n] = \sum_{l=1}^{L} \alpha_l s\left[n - \frac{\tau_l}{T_s}\right] + w[n], \tag{5.1}$$

where α_l represents the complex amplitude and τ_l and T_s the delay of multipath component and the sampling time, respectively. $w[n]$ is zero mean AWGN.

If the received signal consists only of LoS signal, i.e. $L = 1$, the distance between the train wagons is calculated from the difference between the transmit time t_1 and the receive time t_2. The difference between the transmit and receive time is also called the time of flight.

The main advantage of using ToA is the low complexity of the imple-

mentation. On the other hand, highly accurate time stamps and highly synchronized clocks in both transceivers are required to achieve acceptable accuracy. For example, if the clocks of Wagon A and Wagon B differ by 1 µs, the error in distance estimation can be on the order of 300 m.

RTD was introduced to mitigate clock errors and avoid dependence on clock difference. Similar to ToA, RTD requires two transceivers, one in Wagon A and one in Wagon B. Wagon A must send a time-stamped message to Wagon B. Once the message is received, Wagon B must send an acknowledge message back to Wagon A. Naturally, Wagon B introduces a processing delay to process the message from Wagon A and the acknowledgment message. To minimize the processing delay, analog amplify and forward can be used where Wagon B amplifies and forwards any received messages from Wagon A. In this case, considering a quasi-reciprocal channel, the message received at Wagon A satisfies the equation

$$r\left[n\right] = \sum_{l=1}^{L} \alpha_l s\left[n - 2\frac{\tau_l}{T_s} - T_{\text{proc}}\right] + w\left[n\right]. \tag{5.2}$$

T_{proc} is an excess delay caused by processing and forwarding the received message at Wagon B transceiver as shown in Figure 5.1. After decoding the received message, the transceiver at Wagon A compares the time of transmission to the time of reception, the time difference should translate to twice the distance between the two wagons if $T_{\text{proc}} = 0$. The main advantage of this scheme is that it does not depend on the synchronization accuracy of the clocks as the clocks are assumed short time stable. On the other hand, as described in the equation above, there is an excess delay due to the processing of the message and its transmission from Wagon B. This delay can be variable and depends on many external factors, such as the stability of the hardware and the temperature.

Finally, TDoA requires two transceivers on one side (for example, Wagon A) and one transceiver on the other side (Wagon B). Both transceivers on Wagon A must transmit exactly the same message at the same time. This is possible because both transceivers can be connected to the same reference clock. At Wagon B, the transceiver receives both signals. Similar to satellite GPS, if Wagon B knows the distance between the two transceivers in Wagon A, it can estimate the distance by calculating the time difference between

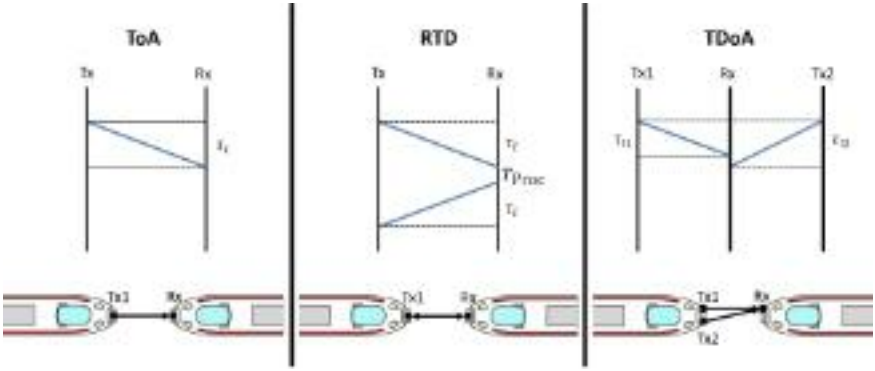

Figure 5.1: Comparison between ToA, RTD, and TDoA.

the reception of the two messages. The accuracy of this scheme is highly dependent on geometry. There may be a severe dilution of accuracy if the two transceivers at Wagon A are very close to each other, as shown in Figure 5.1. Unfortunately, this would be the case here because of the limited space in the nose area of the train wagons.

In summary, TDoA is not suitable for ATC. RTD would work well if we ensure stable hardware and good isolation. ToA is the least complex scheme, but it requires that the clocks in Wagon A and Wagon B be synchronized with extremely high accuracy. In the next sections, ToA is used as the distance estimation scheme of choice to enable ATC.

Theoretical lower bounds will be derived to give us an idea of the order of accuracy we must target under optimum conditions and to compare the proposed mm-Wave SC-FDE system with other candidates such as IEEE ITS-G5 and IR-UWB. We will also study the possible external effects such as the effects from the weather or the antenna heights from the ground. Afterwards, data from the measurement campaign will be used to estimate the accuracy of ToA ranging using a realistic channel. Finally, using the knowledge we gained from the channel measurement, we will propose a novel approach to enhance the accuracy of ToA even if the clocks are not synchronized perfectly.

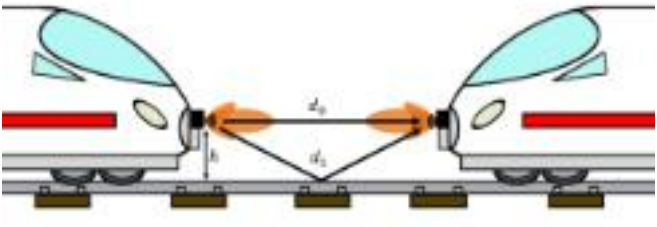

Figure 5.2: Representation of a two-ray channel model between two train wagons.

5.2 CRLB Theoretical Analysis

In this section, theoretical lower bounds will be derived to give an idea of the order of magnitude of accuracy we need to aim for under optimal conditions and to compare the proposed mm-Wave SC-FDE system with other candidates such as IEEE ITS-G5 and IR-UWB. Also, possible external effects such as weather effects or the height of the antennas above the ground will be investigated.

As visualized in Figure 5.2, one transceiver node is connected to the nose of each train wagon. The heights of the transceivers to the ground are known. The transceivers are assumed to be connected with directional antennas having known characteristics to decrease multipath and increase gain. In this specific scenario, it is assumed that the strongest received components are the LoS signal and a GR signal. A good statistical approximation is the two-ray channel model [SSCO09].

The two-ray channel model presumes a superimposed signal consisting of a LoS component and a slightly delayed GR replica. The reflected signal has weaker power due to reflection losses and lower antenna gain, but results in different constructive and destructive interference effects due to the phase difference from the LoS component. Depending on the geometry, the two received signals can overlap, resulting in a stretched, distorted pulse at the receiver end that can affect distance estimation [SSSS17].

The channel response $h_{\mathrm{c}}(t)$ is expressed as follows:

$$h_{\mathrm{c}}(t) = a_0 \delta(t - \tau_0)\, e^{-i\phi(\tau_0)} + a_1 \delta(t - \tau_1)\, e^{-i\phi(\tau_1)}, \tag{5.3}$$

where $\tau_0 = d_0/c$ and $\tau_1 = d_1/c$ are the propagation delays of the LoS and

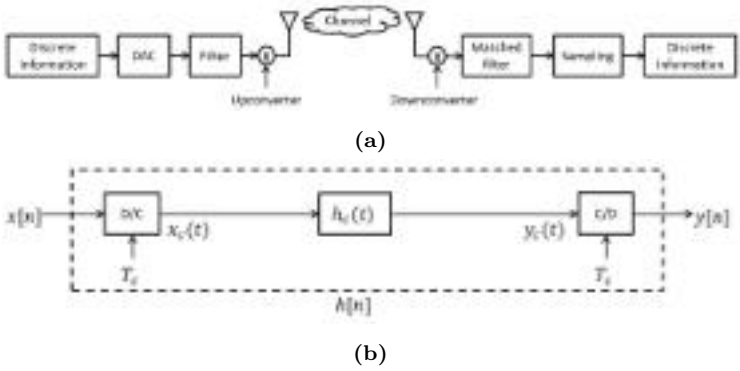

(a)

(b)

Figure 5.3: **(a)** Block diagram of the transmitting and receiving nodes. **(b)** An equivalent discrete representation of the system in **(a)**.

reflected signals. c, d_0 and d_1 are the speed of light, the traveling distance of the LoS path, and that of the GR path. The distance d_1 is a function of d_0 with the relation $d_1 = \sqrt{(2h)^2 + d_0^2}$. The phases of the received signals are denoted as $\phi(\tau_0)$ and $\phi(\tau_1)$ and are delay dependent with the relation $\phi(\tau_\mathrm{i}) = 2\pi f_\mathrm{c} \tau_\mathrm{i}$ for i = 0, 1. $f_\mathrm{c} = c/\lambda$ is the carrier frequency.

The gains of the LoS path and the reflected path are

$$\begin{aligned} a_0 &= \sqrt{G_{\mathrm{ant},0}} \left(\frac{\lambda}{4\pi d_0} \right), \\ a_1 &= \sqrt{G_{\mathrm{ant},1}} \Gamma(\theta) \left(\frac{\lambda}{4\pi d_1} \right). \end{aligned} \tag{5.4}$$

$G_{\mathrm{ant},0}$ and $G_{\mathrm{ant},1}$ are the antenna gains of the LoS and GR paths. The coefficient $\Gamma(\theta)$ is the loss due to ground reflection.

The transceivers system structure is described in Figure 5.3a. The discrete data is upconverted at the transmitter side after being converted from digital to analog. It should be noted that the channel is convolved with the signal in the continuous domain, while the information processed in the receiver is discrete. The discrete information is used for synchronization, equalization and additional data processing. To represent the discrete received signal, a sampled equivalent of the channel response presented in Equation 5.3 can

be directly used as follows:

$$y[n] = a_0 s\left[n - \frac{\tau_0}{T_\mathrm{s}}\right] e^{-i\phi(\tau_0)} + a_1 s\left[n - \frac{\tau_1}{T_\mathrm{s}}\right] e^{-i\phi(\tau_1)} + w[n], \tag{5.5}$$

where T_s is the sampling time, $s[n]$ is the discrete equivalent to the transmitted pulse and $w[n]$ is AWGN with zero mean and variance $\mathrm{E}\left\{w^2\right\} = \sigma^2$. This notation is only valid if the values τ_0/T_s and τ_1/T_s are integers, since the sequence $s[n]$ is only defined by integer values n. This is not a realistic representation and in particular does not apply to the proposed channel model since the proposed channel is based on geometry and the delay should take any non-integer value based on the distance between the transceivers.

An equivalent discrete channel model to $h_c(t)$ should be accurately derived to take non-integer delays into account. Figure 5.3b describes the block diagram representation of the equivalent system. $h[n]$ can be represented as [OS14]:

$$h[n] = a_0 \operatorname{sinc}(t - \tau_0) e^{-i\phi(\tau_0)} + a_1 \operatorname{sinc}(t - \tau_1) e^{-i\phi(\tau_1)}|_{t=nT_\mathrm{s}} \tag{5.6}$$

and the discrete received signal $y[n]$ is properly represented as

$$\begin{aligned} y[n] = a_0 s[n] * \operatorname{sinc}\left(n - \frac{\tau_0}{T_s}\right) e^{-i\phi(\tau_0)} \\ + a_1 s[n] * \operatorname{sinc}\left(n - \frac{\tau_1}{T_s}\right) e^{-i\phi(\tau_1)} + w[n], \end{aligned} \tag{5.7}$$

where $(*)$ represents the convolution operation. With this representation, a focus can be placed on the equivalent effect of the continuous-time system while dealing only with discrete transmitted and received data. This is done by deriving the CRLB of the distance estimators to evaluate their performance.

CRLB is a fundamental concept in estimation theory and is often used to estimate the minimum achievable error variance for an unbiased estimator. It is important to note that this performance cannot usually be achieved by practical estimators. Using the received signal represented in Equation 5.7, we are interested in estimating the parameters $\boldsymbol{\theta} = [\tau_0, \tau_1]^\mathrm{T}$. To do this, it is

assumed that measurement samples y_i, where $i = 1, ..., m$, are observed. A joint PDF is obtained over all samples with respect to the parameters being estimated

$$\mathrm{p}\left(\boldsymbol{y}|\boldsymbol{\theta}\right) = \prod_{i=1}^{m} \mathrm{p}\left(y_i|\boldsymbol{\theta}\right) = \left(2\pi\sigma^2\right)^{-\frac{m}{2}} e^{-\frac{1}{2\sigma^2}\sum_{i=1}^{m}|z_i(\boldsymbol{\theta})-y_i|^2}. \tag{5.8}$$

The log-likelihood can be easily constructed by calculating the natural logarithm of Equation 5.8. The CRLB of the parameters in $\boldsymbol{\theta}$ are the diagonal elements of the inverse of the 2×2 Fisher Information Matrix (FIM) $\boldsymbol{F}\left(\boldsymbol{\theta}\right)$ given by

$$\begin{aligned} \left[\boldsymbol{F}\left(\boldsymbol{\theta}\right)\right]_{k,k} &= \frac{2}{\sigma^2}\sum_{i=1}^{m}\left|\frac{\partial}{\partial\theta_k}z_i\left(\boldsymbol{\theta}\right)\right|^2, \\ \left[\boldsymbol{F}\left(\boldsymbol{\theta}\right)\right]_{k,l} &= \frac{2}{\sigma^2}\sum_{i=1}^{m}\frac{\partial}{\partial\theta_k}z_i\left(\boldsymbol{\theta}\right)\frac{\partial}{\partial\theta_l}z_i\left(\boldsymbol{\theta}\right)^* \end{aligned} \tag{5.9}$$

for $k, l \in \{1, 2\}$.

The derivation of the CRLB is given in Appendix A. Before calculating the FIM, it is necessary to simplify the equation of $s_i\left(\boldsymbol{\theta}\right)$ to obtain a numerical solution for the derivatives. At this point, it is assumed that the phase shift is constant and does not play a role in the estimation of the delay. This assumption results in some loss of information, but is acceptable if the difference between the delays τ_0 and τ_1 is small. The phase difference information is nevertheless included in the derivation by defining $A_0 = a_0 e^{-i\phi(\tau_0)}$ and $A_1 = a_1 e^{-i\phi(\tau_1)}$ as the complex amplitudes of the LoS and GR signals. Therefore, the signal equation can be written as

$$z_i\left(\boldsymbol{\theta}\right) = A_0 s\left[i\right] * \mathrm{sinc}\left(i - \frac{\tau_0}{T_s}\right) + A_1 s\left[i\right] * \mathrm{sinc}\left(i - \frac{\tau_1}{T_s}\right). \tag{5.10}$$

The elements of the FIM can now be derived using Equation 5.9 and Equation 5.10:

$$
\begin{aligned}
\left[\boldsymbol{F}\left(\boldsymbol{\theta}\right)\right]_{k,k} &= \frac{2}{\sigma^2}\sum_{i=1}^{m}\left|\frac{\partial}{\partial\tau_k}A_k s\left[i\right] * \operatorname{sinc}\left(i-\frac{\tau_k}{T_s}\right)\right|^2, \\
\left[\boldsymbol{F}\left(\boldsymbol{\theta}\right)\right]_{k,l} &= \frac{2}{\sigma^2}\sum_{i=1}^{m}\frac{\partial}{\partial\tau_k}A_k s\left[i\right] * \operatorname{sinc}\left(i-\frac{\tau_k}{T_s}\right)\cdot\frac{\partial}{\partial\tau_l}A_l^* s^*\left[i\right] * \operatorname{sinc}\left(i-\frac{\tau_l}{T_s}\right).
\end{aligned}
\tag{5.11}
$$

By defining

$$
r\left(\tau_k\right) = \frac{\partial}{\partial\tau_k}\operatorname{sinc}\left(i-\frac{\tau_k}{T_s}\right) = \frac{\sin\pi\left(i-\frac{\tau_k}{T_s}\right)}{\pi T_s\left(i-\frac{\tau_k}{T_s}\right)^2} - \frac{\cos\pi\left(i-\frac{\tau_k}{T_s}\right)}{T_s\left(i-\frac{\tau_k}{T_s}\right)}, \tag{5.12}
$$

it is possible to obtain

$$
\begin{aligned}
\left[\boldsymbol{F}\left(\boldsymbol{\theta}\right)\right]_{k,k} &= \frac{2a_k^2}{\sigma^2}\sum_{i=1}^{m}\left|s\left[i\right] * r\left(\tau_k\right)\right|^2, \\
\left[\boldsymbol{F}\left(\boldsymbol{\theta}\right)\right]_{1,2} &= \frac{2a_0a_1e^{i2\pi f_c(\Delta\tau)}}{\sigma^2}\sum_{i=1}^{m}s\left[i\right] * r\left(\tau_0\right)\cdot s^*\left[i\right] * r\left(\tau_1\right), \\
\left[\boldsymbol{F}\left(\boldsymbol{\theta}\right)\right]_{2,1} &= \frac{2a_0a_1e^{-i2\pi f_c(\Delta\tau)}}{\sigma^2}\sum_{i=1}^{m}s\left[i\right] * r\left(\tau_1\right)\cdot s^*\left[i\right] * r\left(\tau_0\right),
\end{aligned}
\tag{5.13}
$$

where $\Delta\tau = \tau_1 - \tau_0$.

The main aim is only to investigate the accuracy of the estimation of τ_0 as it is the only parameter required to calculate the distance between the two train wagons. Therefore, the value of the first diagonal element of the inverse of the FIM is what is to be computed. The value is calculated as follows

$$
\begin{aligned}
\left[\boldsymbol{F}^{-1}\right]_{1,1} = \frac{\sigma^2}{2a_0^2}\sum_{i=1}^{m}\left|s\left[i\right] * r\left(\tau_1\right)\right|^2\Bigg(&\sum_{i=1}^{m}\left|s\left[i\right] * r\left(\tau_0\right)\right|^2\sum_{i=1}^{m}\left|s\left[i\right] * r\left(\tau_1\right)\right|^2 \\
&- \sum_{i=1}^{m}s\left[i\right] * r\left(\tau_1\right)\cdot s^*\left[i\right] * r\left(\tau_0\right)\sum_{i=1}^{m}s\left[i\right] * r\left(\tau_0\right)\cdot s^*\left[i\right] * r\left(\tau_1\right)\Bigg)^{-1}.
\end{aligned}
\tag{5.14}
$$

If we assume that the distances between each multipath component are large enough to avoid overlap of the different pulses, and if we assume that the delays are integer, the same lower bounds as in [HK04] and [KN07] are obtained. It should also be noted that if one considers only the LOS component and neglects the reflected signal, all FIM components except $[\boldsymbol{F}(\boldsymbol{\theta})]_{1,1}$ will be zero. The accuracy of the delay estimation in this case would be equal to $[\boldsymbol{F}(\boldsymbol{\theta})]^{-1}_{k,k}$.

By deriving the CRLB, the next step is to evaluate the aforementioned system and compare it with other alternative systems in a two-ray channel. The CRLB is calculated for a wide-band SC-FDE signal operating in the mm-Wave frequency band, an ITS-G5 OFDM signal, and an IR-UWB signal operating at 6 GHz. The simulation parameters of each signal are summarized in Table 5.1.

	SC-FDE	**ITS-G5**	**IR-UWB**
Center frequency	60 GHz	5.9 GHz	6 GHz
EIRP	31 dBm	31 dBm	−14.5 dBm
Pulse shape	Raised Cosine	OFDM	Second-order Gaussian monocycle
Bandwidth	500 MHz	10 MHz	500 MHz
Sampling period	0.2 ns	10 ns	0.2 ns
Number of observed samples	500k	10k	500k

Table 5.1: CRLB simulation parameters.

To allow a fair comparison, a realistic path loss model described in chapter 4, section 4.4.1, was used taking into account oxygen absorption during mm-Wave propagation. In addition, the number of observed samples de-

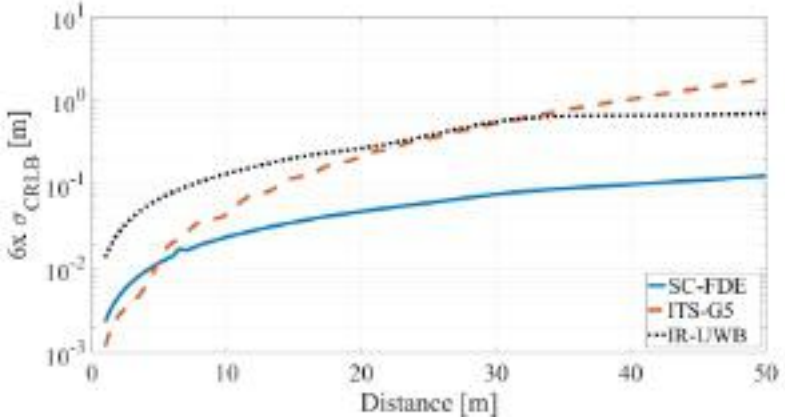

Figure 5.4: Distance estimation lower bounds for SC-FDE, ITS-G5, and IR-UWB signals.

pends on the duration of the observation (0.1 ms in our case). Therefore, the number of observed samples for SC-FDE and IR-UWB is fifty times higher compared to ITS-G5 due to the bandwidth difference. Since we are interested in analyzing the three selected systems for an ultra-reliable application, it was determined to multiply the lower bounds of the estimation accuracy by a factor of six (6σ figure-of-merit), corresponding to a reliability of 99.9997 %, and base our evaluation on the simulated results.

Figure 5.4 shows the accuracy of the distance estimation for transceivers up to 50 m apart. The antenna height to the ground surface (h) is equal to 1.5 m. We considered oversampling by a factor of ten. The geometry, delay, and path-loss are calculated for each separation distance, then the lower bounds are calculated using Equation 5.14.

The proposed SC-FDE signal outperforms both ITS-G5 and IR-UWB due to the wider bandwidth compared to ITS-G5 and the higher transmit power compared to IR-UWB. It is also shown that the distance accuracy lower bounds are in the decimeter to meter range for distances around 50 m and it reaches millimeter to centimeter accuracy for distances of a few meters. These are acceptable accuracy figures for ATC provided by mm-Wave signals.

Due to the wide bandwidth of the mm-Wave signal, it is easier to achieve

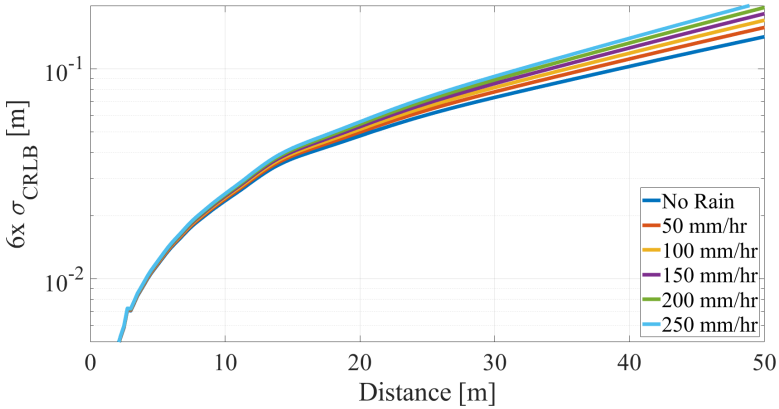

Figure 5.5: Effect of rain attenuation on distance estimation lower bounds for mm-Wave SC-FDE signals.

approximate lower bound accuracy in practical systems using the mm-Wave signal than with ITS-G5, which requires more accurate interpolation and sophisticated receivers to achieve the desired accuracy. The irregularities visible on the mm-Wave curve at distances between 3 and 4 m are due to the fact that the LoS and GR pulses start to overlap at these distances. With the ITS-G5, the LoS and reflected pulses always overlap because the pulse width is fifty times longer.

Figure 5.5 demonstrates the effect of rain on the accuracy of distance estimation with the proposed system operating in the mm-Wave frequency band. A model proposed in [ITU03] was used where losses caused by rain is equal to

$$L_{\mathrm{R}} = kR^{\alpha}, \tag{5.15}$$

where k and α are frequency-dependent coefficients, and R is the rain rate. The simulated rain rate varies from 0 (no rain) to the extreme value 250 mm/h. Losses due to rain at a rate of 250 mm/h cause an additional loss of almost 70 dB/km. This can lead to significant performance losses at long distances. However, as can be seen from the results, rain has minimal effect at the distance range up to 50 m for SC-FDE.

In addition, Figure 5.6 simulates the effect of antenna height on the

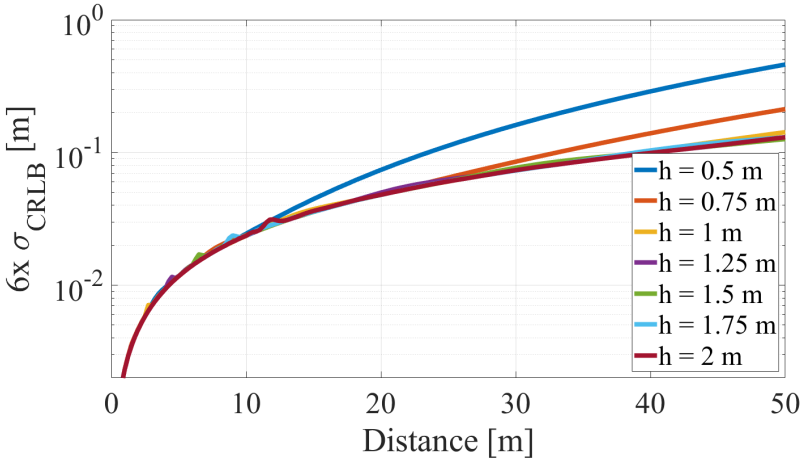

Figure 5.6: Effect of changing antenna height from the ground on distance estimation lower bounds for the SC-FDE system.

accuracy of distance estimation. It can be seen that the performance is worse as the antenna height decreases. This is because the effect of the reflected multipath signal on the LoS signal is more prominent as the antennas are lower. At antenna heights of 1 m and above, the performance is almost the same because the signals of the LoS and reflected paths cause similar decomposition. Hence, there is little difference in the lower bounds for heights equal to 1 m and above.

5.3 Distance Estimation Algorithms

There are a variant of algorithms to estimate parameters. These algorithms could be categorized under Bayesian recursive methods such as Kalman filters [Sor88] and particle filters [GGB+02] as well as snapshot-based estimation methods such as EM [Moo96], Multiple Signal Classification (MUSIC) [Sch86], and Maximum Likelihood Estimation (MLE) [LS02]. To this end, lets assume that the observed signal at the receiver $y[n]$ is formulated as

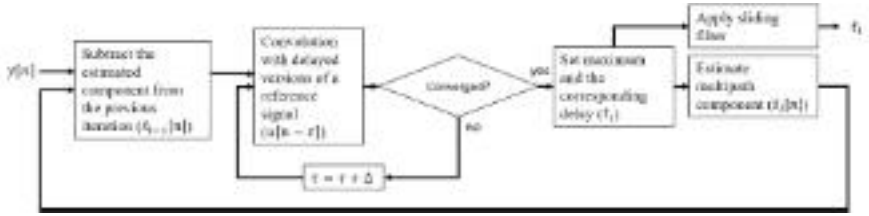

Figure 5.7: Block diagram of the SAGE algorithm used to estimate the delay of the multipath components from the received signal.

$$y\left[n;\boldsymbol{\theta}\right]=\sum_{l=0}^{L-1}s\left[n;\boldsymbol{\theta}_l\right]+w\left[n\right] \tag{5.16}$$

where $\boldsymbol{\theta}=[\boldsymbol{\theta}_0,...,\boldsymbol{\theta}_{L-1}]$ consists of all the unknown parameters at the receiver for all L observed multipath components and $\boldsymbol{\theta}_l=[a_l,\tau_l,\phi_l,\nu_l]$ is the vector containing the parameters of the l^{th} multipath component to be estimated. The parameters are the signal amplitude a, delay τ, phase ϕ, and Doppler frequency ν.

The problem at hand is the estimation of the parameters $\boldsymbol{\theta}_l$ for $l=0,...,L-1$. MLE of these parameters is computationally prohibitive due to the high dimension of $\boldsymbol{\theta}$ for large L. Therefore, an iterative generalized snapshot EM method is proposed in this work. EM is composed of two steps: the expectation (E-step) and maximization (M-step). The E-step allows us to estimate each non-observable multipath component as a conditional expectation based on the observation $y\left[n;\boldsymbol{\theta}\right]$ and assuming the previous estimate $\hat{\boldsymbol{\theta}}_{l-1}$. In the M-step, the estimated observed multipath components are used to estimate the parameters in $\boldsymbol{\theta}_l$ using MLE. The E- and M-steps are carried out in an iterative fashion by assuming an initial value $\boldsymbol{\theta}_l\left(0\right)$ until convergence is achieved. In practice, the convergence is achieved as soon as the distance between two consecutive parameter estimates returned at the M-step is below a predefined threshold.

The EM estimation algorithm allows splitting of the optimization problem required to jointly estimate L superimposed components into L separate optimization problems for estimating a single impinging component.

To decrease the complexity and allow real-time parameter estimation,

the SAGE algorithm was developed [FH94]. The SAGE algorithm is an extension of the EM algorithm. Each iteration of the SAGE algorithm is an EM iteration to re-estimate not necessarily all but only a subset of the components from $\boldsymbol{\theta}$ while keeping the estimates of the other components fixed. Faster convergence for a correspondingly lower complexity is the advantage of the SAGE algorithm when compared to the EM algorithm. The aim of this work is to estimate the distance between two train wagons to enable ATC. To this end, estimating the delay of the LoS signal (τ_0) with SAGE is of relevance.

The way SAGE operates is described in the following. First, the received signal is convoluted with a delayed version of a reference signal to generate the function

$$z\left(\boldsymbol{\theta}; s_l\right) = \sum_{D} u^*\left[n-\tau\right] \cdot e^{-j2\pi\nu n} \cdot e^{-j\phi} \cdot s_l\left[n\right], \tag{5.17}$$

where D is the duration of the received signal and $u\left[n\right]$ is the reference signal. As we are only interested in the delay of the received signal and as the relative velocity between the trains is considerably low, it is valid to consider $\nu = 0$ and $\phi = 0$. This leads to the function

$$z\left(\tau, \hat{\phi}_l = 0, \hat{\nu}_l = 0; s_l\right) = \sum_{D} u^*\left[n-\tau\right] \cdot s_l\left[n\right]. \tag{5.18}$$

Using EM would lead to a three-dimensional MLE of Equation 5.17 for all possible values of τ_l, ϕ_l, and ν_l. Whereas SAGE noticeably decreases the complexity by solving a one-dimensional MLE procedure of Equation 5.18. The procedure to estimate the delay τ_l when SAGE is used can expressed as [FTH+99]

$$\hat{\tau}_l = \arg\max_{\tau} \left\{ \left| z\left(\tau, \hat{\phi}_l = 0, \hat{\nu}_l = 0; s_l\right) \right| \right\}. \tag{5.19}$$

The block diagram of the SAGE distance estimation method is shown in Figure 5.7. First, the received signal is convoluted with a delayed reference signal and a peak search is performed to estimate the delay of the LoS path. Then, the LoS path is subtracted from the received signal to estimate the delay of the second strongest path. This is repeated to estimate the delay of as many multipath components as needed. For ATC, the delay of the LoS

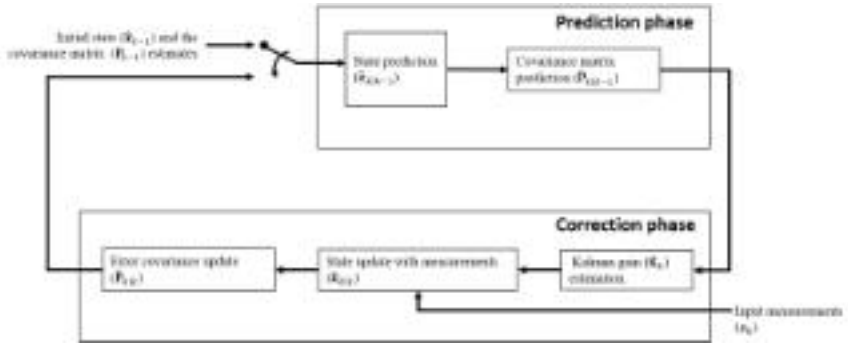

Figure 5.8: Block diagram of KF prediction and correction phases.

path τ_1 is enough to estimate the distance between the two train wagons. A sliding filter is used to exclude outliers (anomalies).

The received signal comprises noise from the hardware and the environment. Therefore, a smoothing filter is foreseen to enhance the distance estimation accuracy. Two possibilities are a sliding filter or a Kalman Filter (KF). While a sliding filter would remove the outliers and smooth the delay estimates curve, a KF is preferred to enable including other measurements such as the train velocity information gathered from the train control system.

The KF consists of two phases, prediction and correction. During the prediction phase, the KF predicts the state $\hat{\mathbf{x}}_{k|k-1}$ and error covariance $\hat{\mathbf{P}}_{k|k-1}$ ahead based on the previous estimated state $\hat{\mathbf{x}}_{k-1}$ and error covariance $\hat{\mathbf{P}}_{k-1}$. The correction phase uses the measurements vector $\hat{\mathbf{z}}_k$ to update the current state and error covariance. The confidence placed on the current measurements is based on the Kalman gain. The block diagram of the KF is shown in Figure 5.8.

The states to be estimated are the relative distance d and the relative velocity v between the two train wagons,

$$\hat{\mathbf{x}}_k = \begin{bmatrix} d & v \end{bmatrix}. \tag{5.20}$$

In the prediction phase, $\hat{\mathbf{x}}_{k|k-1}$ is predicted as follows,

$$\hat{\mathbf{x}}_{k|k-1} = \mathbf{F}_k \hat{\mathbf{x}}_{k-1}, \tag{5.21}$$

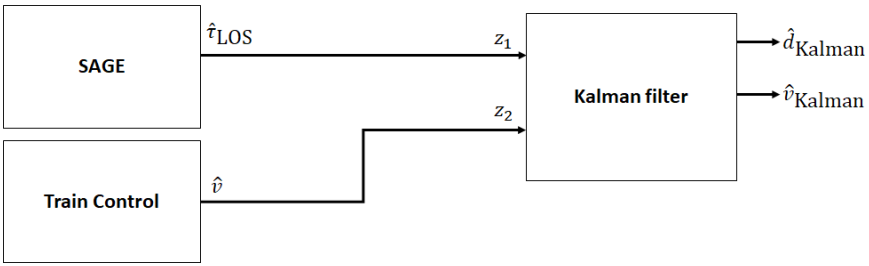

Figure 5.9: Block diagram of the KF used to estimate the distance between two train wagons using SAGE estimates and velocity information as input.

where $\mathbf{F}_k$ is the state transition model. For ATC, the following model is used,

$$\mathbf{F}_k = \begin{bmatrix} 1 & \Delta t \\ 0 & 1 \end{bmatrix}. \tag{5.22}$$

The error covariance is predicted as follows

$$\hat{\mathbf{P}}_{k|k-1} = \mathbf{F}_k \hat{\mathbf{P}}_{k-1} \mathbf{F}_k^{\intercal} + \mathbf{Q}_k, \tag{5.23}$$

where $\mathbf{Q}_k$ is the covariance matrix of the process noise. Also, $\hat{\mathbf{P}}_1$ is initialized as a symmetric diagonal matrix with large diagonal values.

In the correction phase, measurements vector $\mathbf{z}_k$ are used to update the states. To this end, the measurements vector consist of two components: the output of SAGE multiplied by the speed of light ($d_{\text{SAGE}} = c \cdot t_{\text{SAGE}}$) and the velocity estimate from the control system (v_{CTRL}). To this end, the state space and the observation space are mapped using an observation model $\mathbf{H}_k$,

$$\mathbf{H}_k = \begin{bmatrix} 1 & 0 \\ 0 & 1 \end{bmatrix}. \tag{5.24}$$

The estimated state estimate after the correction phase is equal to

$$\hat{\mathbf{x}}_{k|k} = \hat{\mathbf{x}}_{k|k-1} + \mathbf{K}_k \left(\mathbf{z}_k - \mathbf{H}_k \hat{\mathbf{x}}_{k|k-1} \right), \tag{5.25}$$

where $\mathbf{K}_k$ is the Kalman gain. The Kalman gain determines the amount of trust the KF places on the observation vector when compared with the prediction. The Kalman gain is expressed as

$$\mathbf{K}_k = \hat{\mathbf{P}}_{k|k-1}\mathbf{H}_k^\intercal \left(\mathbf{H}_k\hat{\mathbf{P}}_{k|k-1}\mathbf{H}_k^\intercal + \mathbf{R}_k\right)^{-1}, \tag{5.26}$$

where R_k represents the covariance matrix of the observation noise

$$\mathbf{R}_k = \begin{bmatrix} \sigma_{z_1}^2 & 0 \\ 0 & \sigma_{z_2}^2 \end{bmatrix}. \tag{5.27}$$

Finally, the correction phase is concluded by updating the error covariance using the equation

$$\hat{\mathbf{P}}_{k|k} = \hat{\mathbf{P}}_{k|k-1} - \hat{\mathbf{P}}_{k|k-1}\mathbf{K}_k\mathbf{H}_k. \tag{5.28}$$

The block diagram of the Kalman filter is shown in Figure 5.9. As shown in the figure, the Kalman filter uses both SAGE delay estimate and velocity estimate from the control system as inputs to estimate the distance between the train wagons.

5.4 Ranging Performance Using Measurement Data

To evaluate the distance estimation performance using SAGE with a sliding filter versus SAGE with KF, the recorded open-field measurements discussed in Chapter 4 are used. Therefore, the performance evaluation is based on real data which includes hardware imperfections, front-end noise, and other influences from the wireless channel. During these measurements, the distance between the train wagons varied from 0 to 135 m as the wagons approached and disengaged from each other. The transmitter and receiver where synchronized using high accuracy rubidium clocks. The distance estimates from the SAGE output and from the KF are compared to the measurements recorded by Leica Tachymeter reference system. The Leica

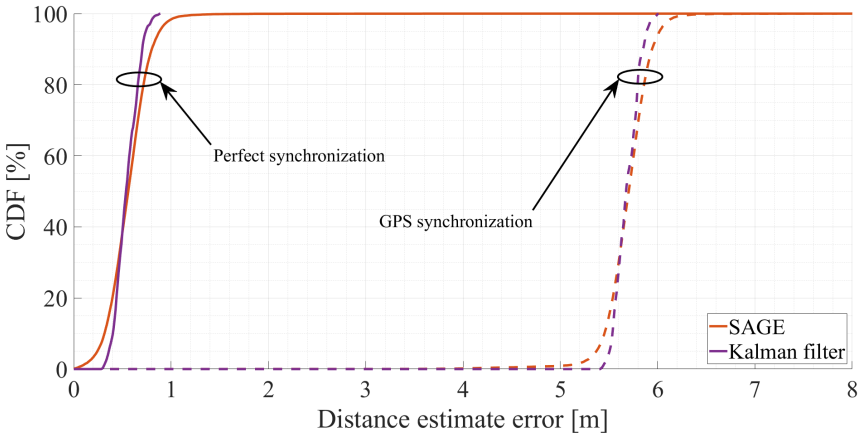

Figure 5.10: The CDF of the distance estimation error of SAGE and KF when the transmitter and receiver clocks are synchronized perfectly or when using GPS receivers.

reference system provides distance estimates with an accuracy of around 5 mm.

The absolute distance error Cumulative Distribution Function (CDF) of SAGE and the KF is plotted in Figure 5.10. For the two solid CDF plots, the transceivers at both wagons are perfectly synchronized using the aforementioned rubidium clocks. While for the two striped CDF plots, an artificial clock shift was introduced to simulate the conditions if GPS receivers are used to synchronize the transceivers. This is a valid assumption because it is not possible to synchronize the transceivers perfectly in a practical way when ToA scheme is used.

In both cases, the CDF plots show that there is an accuracy improvement when the KF is used. The KF provides 1σ accuracy of 65 cm and the largest error value equals 2 m when both transceivers are perfectly synchronized.

Naturally, if GPS receivers are used to synchronize the transceivers, the estimation performance of both SAGE and the KF deteriorates, as the estimators are not able to compensate for the clock offset between the transceivers due to the lack of knowledge thereof. GPS receivers provide synchronization errors of up to ± 10 nm which translates to a distance estimation error of up

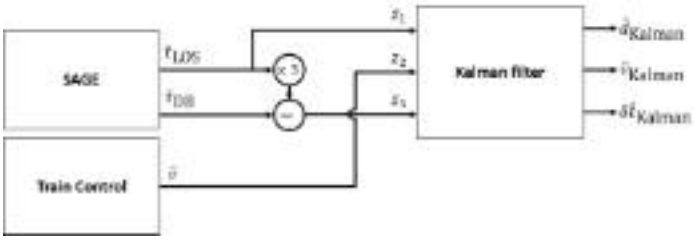

Figure 5.11: Block diagram of the proposed distance estimator exploiting the channel knowledge to compensate the clock offset.

to 6 m. This causes the estimation error CDF curves of both SAGE and KF to shift towards the right when GPS synchronization is used.

5.5 Performance Enhancement Using Channel Knowledge

As described in the end of Chapter 4, the wireless channel between two train wagons consists of three dominant paths: LoS, GR, and double-bounced paths. This knowledge is used to help reduce the synchronization error. The double-bounced signal is weak and noisy but can be used to estimate the clock offset between the transceivers of the two wagons. First, the double-bounced signal delay is estimated using SAGE. The estimated double-bounced signal delay estimate consists of a delay which is three times larger than the LoS signal plus the clock offset between the transmitter and the receiver

$$\hat{\tau}_{\mathrm{DB}} = 3\tau_{\mathrm{LOS}} + \delta t, \tag{5.29}$$

where τ_{LOS} and τ_{LOS} are the LoS and the bounced-signal delays, respectively. δt is the clock offset due to imperfect synchronization.

To have an estimate of the clock offset as an input to the Kalman filter, the estimated delay of the double-bounced signal is subtracted from the LoS signal as follows

$$z_3 = 3\hat{\tau}_{\mathrm{LOS}} - \hat{\tau}_{\mathrm{DB}} = 3\left(\tau_{\mathrm{LOS}} + \delta t\right) - \left(3\tau_{\mathrm{LOS}} + \delta t\right) \approx 2\delta t, \tag{5.30}$$

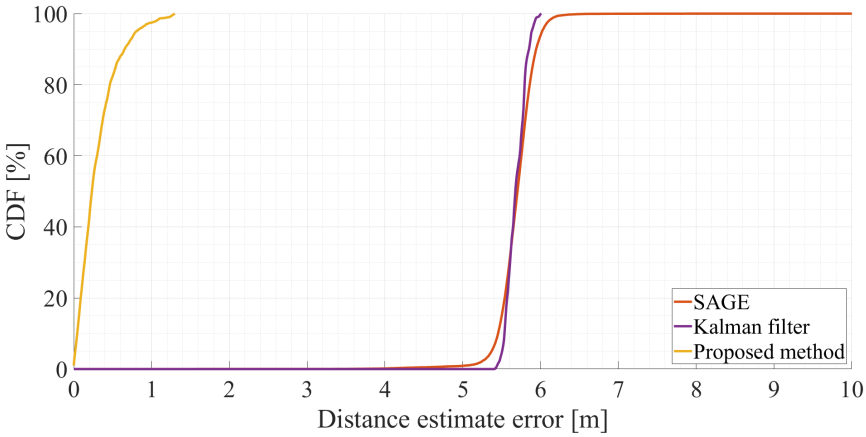

Figure 5.12: Comparison between the CDF of the distance estimation error for SAGE, KF, and the proposed estimation method if GPS clocks were used to synchronize the clocks of the transceivers.

allowing us to have a noisy estimate of the clock offset as a third input to the Kalman filter. It is important to note that Equation 5.30 holds if the reflection surfaces are close to the boresights of the antennas. Otherwise, a constant value of the excess traveled distance is subtracted. This constant can be measured once and recorded for each wagon type.

The estimated values of the LoS and double-bounced delays required to calculate z_3 are provided by SAGE. z_3 is input to the KF together with the delay of the LoS signal (z_1) and the relative velocity between the two wagons (z_2). The states to be estimated are extended to include the clock offset estimates,

$$\hat{\mathbf{x}}_k = \begin{bmatrix} d & v & \delta t \end{bmatrix}. \tag{5.31}$$

Using the proposed estimation method, the observation model $\mathbf{H}_k$ can be described as

$$\mathbf{H}_k = \begin{bmatrix} 1 & 0 & 0 \\ 0 & 1 & 0 \\ 0 & 0 & 2 \end{bmatrix} \tag{5.32}$$

and the state transition model $\mathbf{F}_k$ is described as

$$\mathbf{F}_k = \begin{bmatrix} 1 & \Delta t & 0 \\ 0 & 1 & 0 \\ 0 & 0 & 1 \end{bmatrix}, \tag{5.33}$$

where all states are observable.

The block diagram of the proposed distance estimator is shown in Figure 5.11. The block diagram shows that both SAGE and KF are used in tandem to estimate the distance and compensate for the clock offset by exploiting the channel knowledge. This is done by estimating the delay of the double-bounced path and comparing it with the delay of the LoS signal, as explained earlier.

The proposed solution using the channel information is evaluated and compared to SAGE and to the KF used in the previous section. The CDF of the distance estimation error is plotted in Figure 5.12. The transceivers are assumed to use GPS receivers for synchronization in all cases. The figure shows that by including z_3, i.e. the knowledge gained from the double-bounced signal, we were able to compensate the clock offset between the wagons' transceivers. The proposed distance estimation method provides 6σ accuracy of 129 cm. This is a noticeable performance enhancement when compared to the 6σ accuracy of 600 cm provided by the KF without including z_3.

This improvement can be seen when the actual distance estimates are compared. The actual distance estimates are plotted in Figure 5.13 and are compared with the Leica Tachymeter measured distance. The output from SAGE is noisy and consists of a drift due to clock synchronization errors. The KF smooth the measurements and provides a small improvement as the velocity information is incorporated. The proposed distance estimation

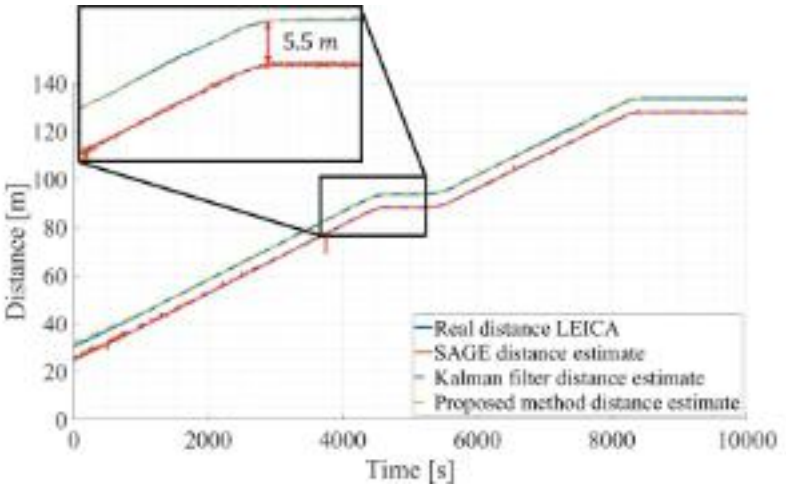

Figure 5.13: Comparison between the distance estimation accuracy for SAGE and three KF implementations compared to the reference in one of the open field runs.

method provides a noticeable improvement as the clock offset is compensated. The proposed method provides a sub-decimeter accuracy in most cases. The accuracy is degraded when the wagons get closer to each others because multipath from other surfaces become more prominent and diffraction affect the estimation of the delay from the double-bounced signal negatively.

5.6 Summary

In this chapter, the possibility of using the proposed SC-FDE mm-Wave to estimate the distance between the two train wagons during the ATC maneuver is investigated. Theoretical CRLB are derived to evaluate the performance of an unbiased estimator on the proposed system. The lower bounds are compared to the those for other standardized systems such as the OFDM IEEE 802.11p system and the SC IR-UWB system. The CRLB results show that the proposed SC-FDE mm-Wave system is expected to provide better distance estimation performance when compared to the other standardized systems.

Furthermore, mm-Wave data recorded during the propagation measurement campaign is used to evaluate the performance of estimation methods, such as SAGE, and the possibility of using a Kalman filter to include velocity measurements from other on-board systems and to exclude anomalies. In addition, various distance estimation schemes, such as ToA, RTD, and TDoA, were discussed.

It was shown that when using ToA, an unconventional approach had to be developed to compensate for the internal clock offset. Therefore, a novel distance estimation method is proposed that benefits from the knowledge of the channel. The proposed method offers better performance compared to conventional estimation methods and provides a 6σ distance estimation accuracy of 129 cm when GPS clock synchronization is used.

Chapter 6

Automatic Train Coupling

6.1 Overview

ATC is the procedure of automatic coupling or uncoupling of trains physically. These maneuvers can be performed while both trains are in motion or when one train is stationary and the other train is moving. The latter can be done at platforms or in shunting yards. For ATC, reliability and distance estimation accuracy requirements increase as the distance between trains decreases. In other words, for short distances between trains of less than 100 m), highly reliable communication with the capability of highly accurate distance estimation is required. In this chapter, the requirements for the ATC maneuver are derived. In addition, all the systems involved and the interactions between the systems involved are modeled using Stochastic Timed Petri Nets (STPN). The modeled system will inform us whether the reliability and distance estimation accuracy of the proposed SC-FDE mm-Wave communication system are good enough to successfully perform an ATC maneuver.

6.2 Automatic Train Coupling Requirements

The most difficult part of the ATC maneuver is the approach of the trains. The two trains involved must closely monitor and control their speeds. The

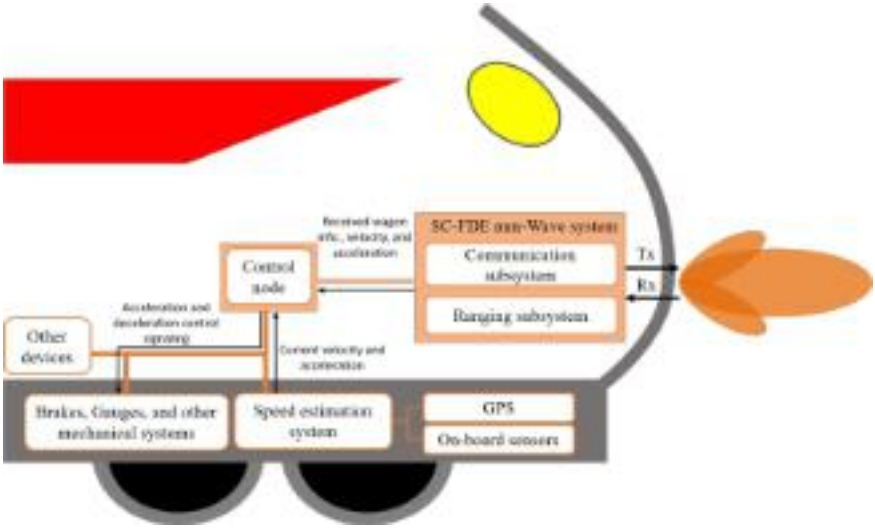

Figure 6.1: An illustration showing the various systems in the train and how they interact with each other to enable the ATC application.

trains must exchange their position, speed and other information reliably and frequently, especially when the distance is very small (less than 100 m). It is assumed in this work that one train partially controls the other train during the maneuver. That is, the requirements vary depending on the distance between the trains. As soon as the driver of the leading train initiates the maneuver, the leading train commands the other train to keep its speed at 0 m/s if the maneuver takes place on a platform or in a shunting yard, or at a fixed speed if both trains are assumed to be in motion. As soon as the other train confirms its fixed speed, ATC maneuver starts.

During the ATC maneuver, various devices (or systems) continuously exchange information over the TCN network. A representation of the devices and systems that are involved can be seen in Figure 6.1. Each of these devices has different roles and requirements. Such roles must be defined to meet the requirements of the ATC application.

The control node is the central operating unit whose main task is to control the speed of the train during the ATC maneuver. The control node requires inputs from various devices, including the speed estimation system

and the SC-FDE mm-Wave communication and distance estimation system. Based on the collected information, the control node decides whether to increase, decrease, or maintain the current speed of the train. The control node must maintain a certain relative speed between trains to ensure the safety of passengers and cargo. If this is not the case, the node must abort the maneuver immediately.

The first step in determining the requirements of the ATC application and the tasks of the various devices is to derive the allowed minimum and maximum relative speeds between trains at each separation distance. Mechanical aspects such as train type, weight, braking power, speed, and coupling type should be considered. Relative speed requirements are discussed subsequently.

6.2.1 Relative Speed Requirements

Train couplers, such as the Scharfenberg couplers most commonly used on high-speed trains in Europe, allow a compression and traction force of 1500 kN [FR817]. According to the EuroSpec recommendation [Eur16], the maximum permissible relative speed of the two cars involved during coupling is 2.7 m/s (10 km/h). Compliance with the above relative speed ensures no damage to the couplers.

Moreover, it is advisable not to disturb passengers or cargo. To ensure this, the displacement of the couplers during engagement must be less than 0.2 m. Assuming that the total weight of the train is about 470 t (German high-speed train Inter-City Express (ICE) 4) and the permissible displacement distance of the couplings (Δd) is 0.2 m, the corresponding relative velocity on engagement is calculated according to the equation

$$v = \sqrt{\frac{2F\Delta d}{m}}. \tag{6.1}$$

The force applied to the coupler is denoted by F and the mass of the train wagon is denoted by m. By solving the equation and using $\Delta d = 0.2$, it is possible to determine that the maximum relative velocity at impact must be less than 1 m/s so that the passengers are not disturbed and the goods are not destroyed. In addition, the minimum relative speed must be above

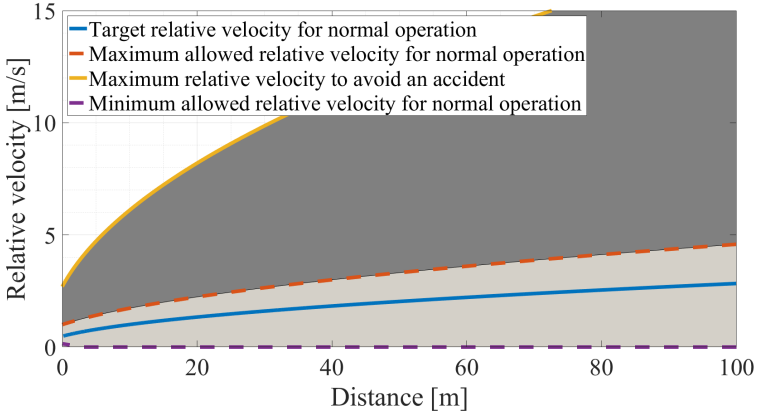

Figure 6.2: A plot showing the operational relative velocity limits required at each separation distance to insure a successful ATC maneuver.

0.15 m/s so that the mechanical coupling interface of the couplings receives sufficient thrust to engage and thus successfully couple.

The optimal relative velocity is shown as a blue solid curve in Figure 6.2. To derive the optimal relative velocity at each distance, it is assumed that the ATC maneuver starts at a distance of 100 m between the trains. Furthermore, the relative velocity at a distance of 100 m is approximately 3 m/s and the deceleration of the approaching train is constant at approximately -0.1 m/s. Finally, the duration of the entire maneuver until physical coupling is about 60 s.

Assuming that acceleration (or deceleration) reaches $\pm 0.5\,\mathrm{m/s^2}$ during normal operation, the upper and lower velocity limits for a successful ATC maneuver are shown as orange and purple dashed lines, respectively. In other words, a successful maneuver is possible if the relative velocity is within the light gray area depicted in Figure 6.2 at all times.

Moreover, taking into account that the trains can perform emergency braking with $-1.5\,\mathrm{m/s^2}$, it is possible to avoid an accident as long as the relative speed is below the yellow curve. If the relative speed exceeds the yellow threshold at any point, an accident is considered inevitable.

It is essential for the control node to constantly monitor the distance

between the two trains and their speeds. On this basis, the control node must steer the train so that it increases, decreases or maintains its speed and that the relative velocity remains within the limits.

Naturally, the upper and lower limits may vary depending on the train type, weight, coupling type, and braking and acceleration capabilities. All the necessary information can be provided by the manufacturer to determine the target speed and the upper and lower limits. Subsequently, these values can be coded as a look-up table in the control node database.

A certain margin of error is expected from each of the devices involved. For example, the relative velocity error can come from GPS errors, on-board sensors, or a combination of these. Many trains estimate their speed using a number of on-board sensors. Trenitalia's high-speed trains use the Trenitalia Unifi algorithm, which provides speed estimates with a mean error of 0.188 m/s [ACM02]. The velocity estimation errors might lead to tighter bounds in the worst case scenario. Hence, the upper bounds are shifted downwards and the lower bounds are shifted upwards.

On the other hand, the proposed SC-FDE mm-Wave communication system uses ToA algorithm to estimate the distance between trains. Theoretical lower bounds of an unbiased ToA distance estimator using the proposed system are derived in Chapter 5. Herein the proposed distance estimation scheme proposed in Chapter 5 is considered for the ATC maneuver. 99.9997 % of the derived distance estimation errors using the proposed method are below 1.29 m (6σ figure-of-merit). Therefore, as a worst case scenario, distance estimation error value of 1.29 m is considered when the train estimate the separation distance.

Including the velocity error and distance estimation error would lead to tighter bounds. These bounds are derived and are included in Figure 6.3 as dashed lines.

It can be summarized that the relative velocity of the two trains involved must be within the dashed curve for the entire duration of the maneuver to ensure a successful ATC maneuver. In this, the velocity and distance estimation errors are taken into account.

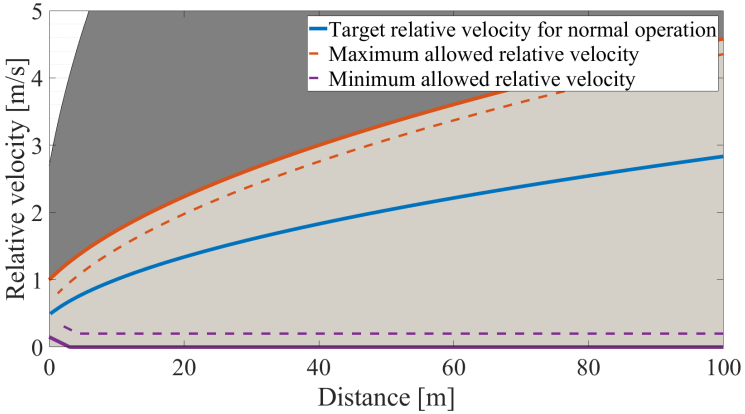

Figure 6.3: A plot showing the operational relative velocity limits required at each separation distance. The dashed illustrated limits include velocity estimation and distance estimation errors while the solid limits do not include any sources of errors.

6.2.2 Safety Integrity Levels

The design of control systems must be defined from the perspective of control engineering. One of the indicators usually used by control engineering is the SIL. SILs are used as indicators of the reliability and safety performance of an electrical control system. SIL levels are defined by the IEC 61508 standard, which is not railway-specific but is used to derive EN 50126, EN 50128 and EN 50129 standards to meet railway-specific requirements [IEC02].

Four SILs are defined for continuous operation, SIL-1 requires at most 10^{-5} probability of failure per hour (PFH). SIL-2, -3, and -4 require at most 10^{-6}, 10^{-7}, and 10^{-8} PFH, respectively. The connection between the requirements of the wireless communication system with the requirements of the control system is missing. For instance, while latency and PER values are important indicators for evaluating a wireless communication system, translating PER and latency measures into SILs is not a straightforward task. In other words, packet errors do not necessarily cause failures at the application level. The number of consecutive errors or the update delay requirements may be more relevant to meet certain SIL requirements. To

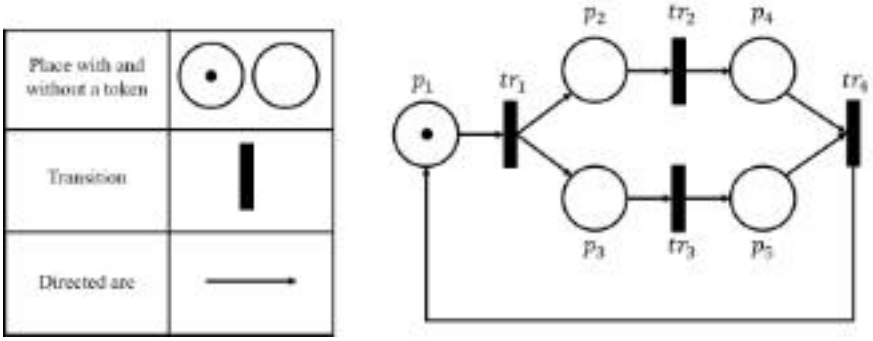

Figure 6.4: An illustration visualizing different PN graphical representations (left) and a sample system representation (right).

provide a solution to this research question, the proposed SC-FDE mm-Wave wireless communication system and its interaction with the control system are presented in the following using PN.

6.3 Petri Nets

PN are usually used by control engineers for the study and analysis of concurrent systems. PN are graphical tools that can be described by a set of linear algebraic equations or other mathematical models that reflect the behavior of the modeled system. Thereby allowing a formulaic analysis of the model through a mathematical verification of the properties associated with the behavior of the underlying system. For example, PN can analyze priority in triggering multiple events, repetitive activities, and mutual exclusion of shared resources.

The ability to verify a model in a formal manner is particularly important for safety-critical real-time systems, such as railroad control systems. PN are used to model real-time fault tolerant and safety critical systems [DT89, BG91, LS87]. Furthermore, PN have been used extensively to model and analyze railway traffic control and railway on-board systems [Gha09, Gha17, BG18, SS19].

Conventional PN consist of places, transitions, and directed arcs connecting

places with transitions and transitions with places. Figure 6.4 shows a graphical representation of the individual components and an example representation of a system. In the exemplary representation above, place p_1 is an input place of transition tr_1 and places p_2 and p_3 are output places of transition tr_1.

In order to study the dynamic behavior of the modeled system in terms of its states and their changes, each place can contain either no tokens or a positive number of tokens represented by small solid circles. The presence or absence of a token at a location can indicate whether a condition associated with that location is true or false. At any point in time, the distribution of tokens at locations, called PN markers, defines the current state of the modeled system. A marking of a system represented by m places is represented by a $m \times 1$ vector $\mathbf{ma}$. Each entry in the vector denotes the number of tokens at the corresponding place. For example, in the PN model shown in Figure 6.4, $\mathbf{ma} = (1, 0, 0, 0, 0)^T$.

Formally, a PN can be defined as follows

$$\mathbf{PN} = (\mathbf{p}, \mathbf{tr}, \mathbf{IN}, \mathbf{OUT}, \mathbf{ma}_0)\,; \tag{6.2}$$

where $\mathbf{p} = \{p_1, p_2, \ldots, p_m\}$ is a finite set of places, $\mathbf{tr} = \{tr_1, tr_2, \ldots, tr_n\}$ is a finite set of transitions. $\mathbf{IN}$ and $\mathbf{OUT}$ are non-negative $m \times n$ matrices defining directed arcs from places to transitions and from transitions to places, respectively. $\mathbf{ma}_0$ is the initial marking. More details of PN, their properties, and types can be found in [ZZ94].

In this work, the focus will be on STPN. STPN is a special form of PN where each transition is triggered after a certain time period $\mathbf{t}$. $\mathbf{t}$ is a $n \times 1$ vector, where each time period $t_i = [a_i, b_i]$ defines the time period in which the corresponding transition tr_i can be triggered. t_i is uniformly distributed within $[a_i, b_i]$, where a_i is the minimum allowed delay and b_i is the maximum allowed delay.

The values of a_i and b_i depend on the communication protocol used. For instance, if WTB is used, the expected delay has values between 0 and 25 ms, depending on whether the message is transmitted immediately or whether the transmitter has to wait for the next slot to transmit the message. WTB messages are transmitted periodically every 25 ms as explained in

chapter 2.1.2.

In addition, Weighted STPN are of interest in this work, where each place has a certain weight w_i. The weights indicate how many tokens are required to trigger the corresponding place. For example, a place p_i with $w_i = 3$ requires the presence of at least three tokens to trigger and activate the transition or transitions it is associated with. weighted STPN are used below to represent the ATC maneuver and to show how different devices interact during the maneuver instances.

6.4 System Representation Using Petri Nets

ATC maneuver involves complex interaction between many devices such as the proposed SC-FDE mm-Wave communication system, the control node, the velocity estimation equipment, and the acceleration and braking mechanical systems. Representing the entire maneuver and describing each interaction is a tedious task. Weighted STPN are used to formally represent the ATC maneuver in a clear and accurate representation.

TIme petri Net Analyzer (TINA) software is used to model the interaction between the involved devices during the ATC maneuver. TINA is a toolbox for editing and analyzing PN developed by the Laboratory for Analysis and Architecture of Systems in Toulouse [BV06]. TINA has the capability of analyzing weighted STPN. The full representation of ATC using TINA is detailed in the Appendix B. Throughout this chapter, we will only focus on the important interactions between the control node and all other systems such as the mm-Wave SC-FDE wireless communication system, the mechanical devices and all other systems involved.

The STPN representation of the interaction between the control node and the other devices is shown in Figure 6.5. All interactions between the control node and the communication system are considered to use WTB. Therefore, each transition between the control node and the communication system has an equally distributed delay ranging from 0 to 25 ms. The aforementioned transitions are represented in Figure 6.5 with a red color. Thereafter, all other interactions use MVB protocol. Therefore, all other transitions have an equally distributed delay ranging from 0 to 1 ms. These transitions have

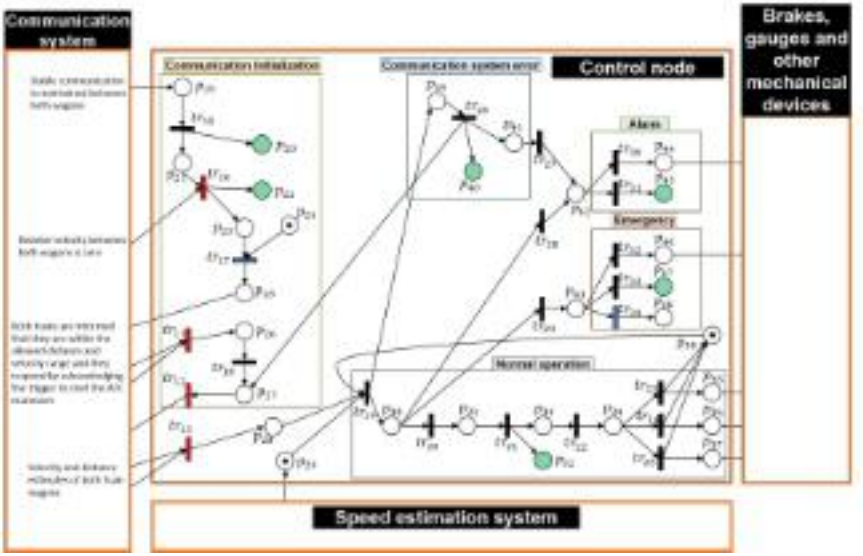

Figure 6.5: Weighted STPN representation of the interaction between the control node and other devices during an ATC maneuver.

the color black. Two transitions, tr_{17} and tr_{34} in Figure 6.5, are highlighted with the color blue. Both of these transitions have different delays and are explained in more detail below. The places filled with green stripes denote visual indication to the train driver, such as light indicators on the driver's console.

In this chapter, the communication initialization process is not discussed because it is not relevant for deriving the performance requirements for the communication system. For more information, refer to Appendix B.

The first information signal received by the communication system is routed through tr_{13} and evaluated by p_{28}. At p_{28}, the control node receives the distance estimate of its own train **TW1** as well as the distance estimate of the other train involved in this ATC maneuver, **TW2**). In addition, the control node receives the velocity estimate of **TW2**. p_{29} incorporates the velocity estimate of $\mathbf{TW}_1$. The estimate is computed by the velocity estimation system. The mean error of the estimates is assumed to be 0.188 m/s, as described in 6.2.1.

tr_{19} is triggered when p_{28}, p_{29}, and p_{38} have tokens. It is assumed that p_{29} always has a token, since it is assumed that the velocity estimation system regularly updates the control node with the estimates. On the other hand, p_{38} has a token at the beginning of the maneuver and at the end of each normal operating cycle to indicate the end of the current cycle. In other words, p_{38} prevents a start of a loop unless the previous loop is concluded.

Subsequently, the data received from the communication system is evaluated and the distance estimates of **TW1** and **TW2** are compared. If the difference between the two estimates is within a predefined threshold, tr_{19} would pass the token to p_{30}. Otherwise tr_{19} would pass the token to p_{39} and report an error in the communication system. This could also happen if the communication data is corrupted or not decodable.

6.4.1 Normal Operation

When all systems provide the correct input at a timely manner and operate as expected, normal operation is assumed. To trigger the tr_{19} transition and thus normal operation, the MMSE of the distance estimates of **TW1** and **TW2** must be below a predefined threshold. Furthermore, there must be no communication errors. At p_{30}, the control node evaluates the relative speed and compares it with the required relative speed for normal operation. The required relative speed at each separation distance can be stored in the train database as a lookup table. It is assumed that different lookup tables are recorded at each train control node, one for each train wagon type. Presently, the values shown in Figure 6.3 are used. If the relative velocity is within the normal operating range (light gray area), tr_{20} is triggered. If the relative velocity is above the maximum permissible relative velocity, an alarm is triggered. Depending on the severity of the error, a minor alarm tr_{28} or a major alarm tr_{29} is triggered. Major alarms are only triggered if an unavoidable accident is to be expected.

Assuming that the relative speed is within the normal operating range, the train proceeds with the ATC maneuver by informing the driver that normal operation has been triggered. This event takes place at p_{32}. In parallel, at p_{33}, the train control node accesses the database and retrieves the relevant lookup table which relates the relative velocity and the distance between the

train wagons. Afterwards, the train control node compares the estimated speeds and distances with the values in the database at p_{34}.

Subsequently, if the velocity is exactly equal to the target relative velocity (blue line in Figure 6.3), the control node commands the mechanical devices to maintain the current velocity via p_{35}. Otherwise, the control node instructs the mechanical devices to increase or decrease the speed if the speed is lower or higher than the target speed, accordingly. These two events take place in p_{36} and p_{37}, respectively. In either case, the control node triggers p_{38} to indicate the end of the current normal operating cycle. This signals the readiness of the control node to evaluate the next data set provided by the communication system. The control node must repeat this loop until either the maneuver was completed and successful or an alarm was triggered due to an error in the communication system.

6.4.2 Communication Error

If a communication error is detected at p_{28}, tr_{19} activates p_{39} to inform the control node that a communication error has occurred. In such a case, the error is propagated through tr_{26} to two places simultaneously, p_{40} and p_{41}. On the one hand, p_{40} is used to inform the driver of a communication error, e.g., by flashing an error signal in the driver's cockpit. On the other hand, p_{41} is a weighted place with variable weight. The weight value depends on the current separation distance between the trains and on how many communication errors can be tolerated before the relative velocity would potentially exceed the maximum allowed relative velocity.

In Figure 6.3 it can be observed that the difference between the target velocity and the maximum velocity threshold decreases as the distance between the two trains decreases. Therefore, the number of permissible consecutive errors is expected to decrease as trains approach each other due to more stringent requirements. As soon as the specified number of tokens appears on p_{41}, an alarm is triggered via tr_{27}. In this case, the train immediately aborts the ATC maneuver and commands the mechanical devices to brake via p_{44} until the two trains are at a safe distance. The train control node informs the driver that the maneuver has been aborted using p_{45} by flashing an abort indicator in the driver's cockpit.

6.5 Communication Performance Requirements and Evaluation

As a next step to evaluate the performance of the SC-FDE mm-Wave communication system, the number of tokens needed at p_{41} to trigger the abortion of the ATC maneuver must be derived. The number of tokens must be transformed into the number of permissible successive communication errors. To calculate the number of consecutive errors allowed, the time required for the relative velocity to potentially cross the maximum velocity limit is calculated at each separation distance. The aforementioned time includes the amount of delay incurred for each update p_{41} receives, the time required to notify the mechanical devices to abort the maneuver, and the response time of the mechanical devices, e.g., the response time of the brakes to take effect.

For all interactions between the communication system and the control node, an update delay of 25 ms is assumed according to the WTB protocols, and for all other interactions, an update delay of 1 ms is assumed as defined by the MVB protocols. The reaction time of the brakes depends on their type and state. In this work, we assume that the reaction time of the brakes is about 100 ms.

Based on the aforementioned values, the number of permissible subsequent errors can be derived. The results are shown in Figure 6.6. The total update delay for each communication update loop is 52 ms plus the expected response delay caused by the mechanical parts such as the brakes, which is considered to be approximately equal to 100 ms. The results show the maximum allowable successive errors at each separation distance to avoid the ATC maneuver failure. The closer the train wagons approach each other, the fewer successive communication errors are required to exceed the allowable speed limit. In other words, the communication performance requirements become more stringent the closer the trains are to each other.

Consequently, the probability of failure is equal to the PER estimated at each separation distance multiplied by the maximum number of allowed consecutive errors plus one. To evaluate the performance of the proposed SC-FDE mm-Wave communication system using the SIL criterion, the PFH

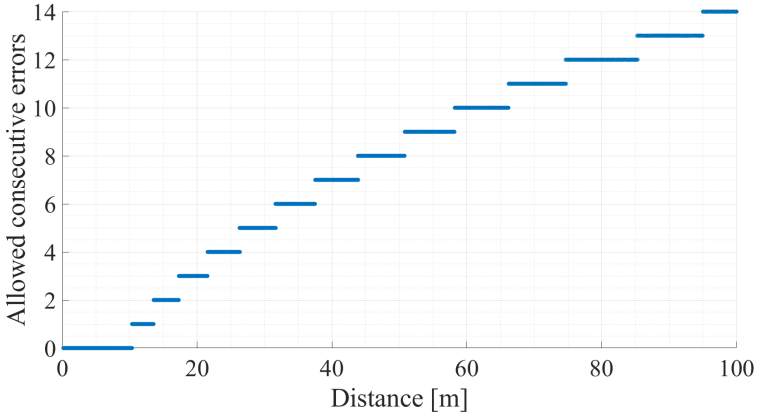

Figure 6.6: The number of allowed consecutive communication system errors to avoid ATC maneuver failure.

values are calculated for each separation distance d following the equation

$$\mathbf{PFH}\,(d) = \mathbf{PER}\,(d) \times (n_{\mathbf{CE}}\,(d) + 1) \times R \times 3600, \tag{6.3}$$

where $n_{\mathbf{CE}}\,(d)$ is the number of allowed consecutive errors at the corresponding distance d. R is defined as the data rate in symbols per second.

The PFH curves are shown in Figure 6.7, which compares the performance of the communication system using three different settings. The performance of the proposed SC-FDE mm-Wave communication system with CPA and a single or two redundant links is compared with the proposed system with horn antennas and two redundant links. The above three configurations are compared against the SIL-4 criterion. SIL-4 is used as the required upper limit to indicate whether the proposed system can meet the ATC application requirements from a control engineering perspective.

Notably, two redundant links improve the performance of PER over the entire maneuver, as expected. Whereas, CPA reduces the influence of the signal reflected from the ground, especially at large distances between 80 and 100 m. SIL-4 requires that the PFH values do not exceed 10^{-8} at any time. When compared to this upper limit, the results show that the use of two redundant wireless communication links and CPA satisfies the SIL-4

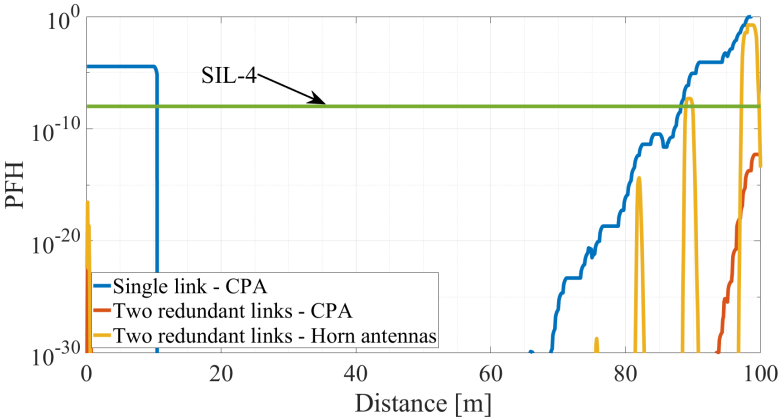

Figure 6.7: Probability of failure per hour for the proposed mm-Wave SC-FDE communication system at each separation distance with CPA compared to horn antennas with and without redundancy.

requirement.

6.6 Summary

In this chapter, we presented the various systems and devices involved in the ATC and discussed the interaction between them. The relative velocity requirements to perform a successful ATC maneuver were derived. Furthermore, the upper and lower bound curves to avoid accidents were plotted. Distance estimation and velocity estimation errors were included in the derivation. Including the aforementioned errors cause more stringent upper and lower bounds.

To evaluate the proposed SC-FDE mm-Wave communication system and determine if its performance is sufficiently good to successfully perform the ATC maneuver, the control node and its interaction with all other systems and devices were modeled using STPN. The toolbox TINA was used to evaluate the model. In addition, the interaction between the control node and other systems during normal operation and communication failures was described. By analyzing the STPN model, it was revealed that the ATC

maneuver is successful as long as the number of permissible consecutive communication errors does not exceed a predefined value. The predefined value is directly proportional to the distance between the train wagons. In other words, the smaller the distance between the trains, the smaller the number of consecutive errors allowed to avoid a maneuver failure.

Eventually, it was possible to evaluate the proposed SC-FDE mm-Wave communication device at the system level using the PER plots in combination with the allowed consecutive errors. The SIL levels were used as the evaluation criteria. The simulation results show that the proposed SC-FDE mm-Wave communication system meets the SIL-4 criterion as long as CPA antennas are used and redundancy is utilized.

Chapter 7

Summary and Conclusion

7.1 Summary

The development of rail transport systems is of great importance nowadays. There is a desire to shift passenger and freight traffic from road to rail, as rail is more energy efficient and causes less pollution. To facilitate the transition from road to rail, it is important to increase the efficiency of rail infrastructure use by enabling future applications.

The aim of this work is to investigate the possibility of enabling the ATC application. It is anticipated that ATC will increase the utilization of railroad infrastructure, increase the efficiency of the coupling and decoupling process, and thus increase the attractiveness of rail transportation systems.

To enable ATC, a wireless T2T communication and ranging system is required. Therefore, in **Chapter 2** an investigation on various wired and wireless communication systems was conducted. The state of the art in wired communication systems is highlighted to provide the basis for the operation of railroad systems. Moreover, various standardized and proprietary wireless communication systems were discussed to identify possible candidates for ATC. The study concluded that wireless communication systems with direct D2D communication mode are required to meet the latency requirements. Two communication systems were highlighted in the study, namely the SBDist and ITS-G5 system. While both systems are considered to enable

ATC, the SBDist system is chosen due to the larger bandwidth utilized. As was seen in **Chapter 5**, the larger bandwidth provides better ranging accuracy.

Motivated by the above conclusion, the evaluation and further development of the SBDist system was carried out in **Chapter 3**. Whereas the SBDist system provides the required performance in a AWGN channel, the ATC channel is expected to have contribution from two multipath rays, the LoS ray and the GR ray. Therefore, further development and evaluation was required to ensure the resilience of the SBDist system against the adverse effects of multipath components. In this work, three approaches have been adopted to improve the overall PER performance. First, frequency domain equalization and advanced preamble sequences were considered in the design of the physical layer. Second, CPAs were used to reduce the influence of the GR ray. Finally, various redundancy techniques were studied. The aforementioned approaches showed a significant improvement with respect to PER performance values. Moreover, PER fluctuations due to GR beam interference were minimized.

The SBDist communication system operates in the mm-Wave frequency band intended for ISM applications. Literature investigation revealed that there is a lack of mm-Wave channel models based on actual measurements in the railroad environment. Therefore, as described in **Chapter 4**, a mm-Wave T2T propagation measurement campaign was conducted at the RWTH Aachen University in Germany. Two experimental trains were used for the measurements, with one train moving toward and away from the other wagon to emulate the ATC maneuver. The recorded data showed that the measurements were consistent with the theoretical geometry-based two-ray path loss model. This suggests that the assessments performed in Chapter 3 are valid and would reflect real world levels of performance. In addition, a third multipath component was observed traveling nearly three times the distance as the LoS ray. This component is the result of the double bounce off the train bodies. Although the contribution of the third ray would not affect the performance of the communication system, it was used to improve the ranging accuracy, as described in Chapter 5.

Chapter 5 commenced with a comparison between distance estimation

schemes such as ToA, RTD, and TDoA. The comparison showed that ToA is the most suitable in the intended environment. Subsequently, theoretical CRLB for an unbiased estimator of the SBDist system were derived and compared to the lower bounds of ITS-G5 and IR-UWB. The results showed that the SBDist system has more accurate ranging estimates and that CRLB provided an indication of the expected ranging accuracy and optimal height for the installation of the SBDist transceiver modules. Finally, distance estimation algorithms such as SAGE and Kalman filters were used to enable ranging capability for the SBDist system. Data sets collected during the measurement campaign were used to evaluate the ranging accuracy. The knowledge gained from the propagation measurement campaign was used to compensate for the clock offset, and the distance estimation algorithm developed provided 6σ accuracy of 129 cm when GPS clock synchronization is used.

Chapter 6 connected the dots by defining the requirements for ATC. For this purpose, unconventional methods were used to derive the mechanical limitations and requirements by considering the mechanical and physical properties of the train wagons and their couplers. Additionally, the SBDist system, the control system, the mechanical systems, the speed estimation system, and the interactions between them were modeled using STPN. The system model using STPN identified the maximum number of consecutive communication errors that could be tolerated at each distance in order to perform a successful ATC maneuver. Moreover, ranging errors and uncertainties from other systems were included in the system model to obtain more representative conclusions. The results were converted to PFH values to assess whether the SBDist system would meet specific SIL levels.

7.2 Conclusion

ATC will enable efficient use of rail infrastructure and potentially enable other future applications. A T2T URLLC system capable of ranging is required to enable ATC. The SBDist system is the best candidate for this application, but some modifications were required to improve the PER performance. The extension of the physical layer, the introduction of CPAs, and the

use of redundancy provided exceptional PER performance. Utilizing the ToA scheme and considering the GPS-based clock synchronization, a novel distance estimation method is proposed. The proposed method provides a 6σ ranging accuracy of 129 cm.

To make the above results significant, the requirements of the application ATC were defined. From the requirements, it can be seen that as the distance between train wagons decreases, more stringent communication and ranging accuracy is necessary. By deriving the minimum allowed communication and ranging accuracy at each distance, a maximum number of consecutive communication errors must not be exceeded. These values can be derived and are based on the mechanical aspects of the train wagons involved. Besides, the number of consecutive errors can be conveniently converted into PFH values. As a result, it was found that the SBDist system satisfies the most dependable SIL-4 threshold at all separation distances. Therefore, it is possible to use the SBDist system to enable ATC by implementing the proposed modifications.

7.3 Outlook and Future Work

Although this is a self-contained study with clear objectives and results, there are numerous areas in which this research can be expanded. Some of the future research areas are highlighted in the following.

- The knowledge gained from the propagation measurement campaign was extremely useful for improving the ranging accuracy. To compensate for the drift between the two train clocks, a double-bounced multipath component was used. Due to the complex geometry of the train body and path loss, the estimate of the double-bounced ray is extremely noisy and exhibits a large variance. To improve the ranging accuracy of the proposed estimation method, the introduction of a more distinct and deterministic double-bounced ray could be beneficial. For this purpose, Reconfigurable Intelligent Surfaces (RIS) or flat reflective surfaces can be used. RIS can be installed at the front of each train wagon to reflect mm-Wave signals with greater accuracy while avoiding scattering, uncertainty, and unnecessary loss. RIS can

be especially beneficial on curved track sections or in sections with different elevation levels.

- The SBDist system can be exploited in a variety of ways to increase the safety of trains. For instance, the SBDist system can be potentially used to monitor train integrity when train wagons are coupled and to monitor the track for possible obstacles to avoid collisions. To evaluate the usability of the SBDist system, studies are needed to define the aforementioned applications and their requirements. In addition, an assessment of the performance and possible modification of the SBDist system is required.

- The interest in Artificial Intelligence (AI) Machine Learning (ML) is at its peak in this decade, as there are a variety of applications that can benefit from ML such as next generation mobile communication systems, autonomous vehicles, etc. The same is true for the ATC application. ML can be used in various domains to enhance the performance of the SBDist system and to introduce new applications. For example, operational relative velocity limits, optimal maneuver duration, mechanical equipment health, and other aspects for each train and coupler type can be estimated and maintained using ML techniques.

- Chapter 6 contains a system-level design of the systems involved to enable ATC. Simple but effective models were used, namely the STPN. Nevertheless, it would be advantageous to entrust the continuation of this work to system design experts in order to provide an advanced interpretation of the systems involved and their interaction. In addition, it was assumed that the response time of mechanical systems such as the brakes has a constant value, regardless of the health of the systems or other factors that may affect the values. A more detailed analysis may be needed to evaluate the performance under different conditions.

Appendices

Appendix A

CRLB derivation

We start this chapter by defining the CRLB. To do so, and following the notation from Chapter 5, consider a measurement $y[n;\boldsymbol{\theta}]$ consisting of L superimposed signals $s[n;\boldsymbol{\theta}_l]$. The measurements depend on a set of parameters $\boldsymbol{\theta} = [\theta_1, ..., \theta_L]$. Using an estimator, it is of interest to estimate the set of L parameters $\hat{\boldsymbol{\theta}} = \left[\hat{\theta}_1, ..., \hat{\theta}_L\right]$.

The estimate $\hat{\theta}_l$ is a random vector and is considered unbiased if the mean of the estimate of the parameters equals the value of the parameters itself

$$\mathrm{E}\left\{\hat{\theta}_l\right\} = \theta_l. \tag{A.1}$$

It is desirable to seek an unbiased estimator which is as close as possible to the parameter being estimated. For an unbiased estimate, the variance

$$\mathrm{VAR}\left\{\hat{\theta}_l\right\} = \mathrm{E}\left\{\left|\hat{\theta}_l - \theta_l\right|^2\right\} \tag{A.2}$$

is an appropriate measure of closeness of an estimator of parameter θ_l.

Before deriving the CRLB, we might have a look on the expectation value

$$\mathrm{E}\left\{\frac{\mathrm{d}}{\mathrm{d}\boldsymbol{\theta}}\ln \mathrm{p}(\mathbf{y}|\boldsymbol{\theta})\right\} = \iint_{-\infty}^{+\infty} \frac{\mathrm{d}}{\mathrm{d}\boldsymbol{\theta}}\ln \mathrm{p}(\mathbf{y}|\boldsymbol{\theta})\, \mathrm{p}(\mathbf{y}|\boldsymbol{\theta})\, \mathrm{d}\mathbf{y}, \tag{A.3}$$

where $\mathrm{p}(\mathbf{y}|\boldsymbol{\theta})$ is the conditional PDF of the measurements given a real valued parameter vector $\boldsymbol{\theta}$, which is of interest to be estimated.

$$\because \quad \frac{\mathrm{d}}{\mathrm{d}\boldsymbol{\theta}} \ln \mathrm{p}(\mathbf{y}|\boldsymbol{\theta}) = \frac{\frac{\mathrm{d}}{\mathrm{d}\boldsymbol{\theta}} \mathrm{p}(\mathbf{y}|\boldsymbol{\theta})}{\mathrm{p}(\mathbf{y}|\boldsymbol{\theta})} \tag{A.4}$$

$$\therefore \quad \mathrm{E}\left\{ \frac{\mathrm{d}}{\mathrm{d}\boldsymbol{\theta}} \ln \mathrm{p}(\mathbf{y}|\boldsymbol{\theta}) \right\} = \frac{\mathrm{d}}{\mathrm{d}\boldsymbol{\theta}} \iint_{-\infty}^{+\infty} \mathrm{p}(\mathbf{y}|\boldsymbol{\theta}) \, \mathrm{d}\mathbf{y} = \frac{\mathrm{d}}{\mathrm{d}\boldsymbol{\theta}} 1 = 0. \tag{A.5}$$

As already mentioned, we are interested in the variance of an estimator $\mathrm{VAR}\left\{ \hat{\boldsymbol{\theta}}\left(\mathbf{y}\right) \right\}$. To derive the minimum variance an unbiased estimator may achieve, we must have a look at the covariance function $\mathrm{COV}\left\{ \hat{\boldsymbol{\theta}}\left(\mathbf{y}\right), \frac{\mathrm{d}}{\mathrm{d}\boldsymbol{\theta}} \ln \mathrm{p}(\mathbf{y}|\boldsymbol{\theta}) \right\}$. According to Equation A.5, the expectation value of the second argument is equal to zero. Furthermore, using the Cauchy-Schwarz Inequality [BL06], we can express

$$\left| \mathrm{COV}\left\{ \frac{\mathrm{d}}{\mathrm{d}\boldsymbol{\theta}} \ln \mathrm{p}(\mathbf{y}|\boldsymbol{\theta}), \hat{\boldsymbol{\theta}}\left(\mathbf{y}\right) \right\} \right|^2 \leq \mathrm{VAR}\left\{ \frac{\mathrm{d}}{\mathrm{d}\boldsymbol{\theta}} \ln \mathrm{p}(\mathbf{y}|\boldsymbol{\theta}) \right\} \mathrm{VAR}\left\{ \hat{\boldsymbol{\theta}}\left(\mathbf{y}\right) \right\}. \tag{A.6}$$

By defining the left hand side of Equation A.6 as

$$\begin{aligned} \mathrm{COV}\left\{ \frac{\mathrm{d}}{\mathrm{d}\boldsymbol{\theta}} \ln \mathrm{p}(\mathbf{y}|\boldsymbol{\theta}), \hat{\boldsymbol{\theta}}\left(\mathbf{y}\right) \right\} &= \mathrm{E}\left\{ \frac{\mathrm{d}}{\mathrm{d}\boldsymbol{\theta}} \ln \mathrm{p}(\mathbf{y}|\boldsymbol{\theta}) \, \hat{\boldsymbol{\theta}}\left(\mathbf{y}\right) \right\} \\ &= \iint_{-\infty}^{+\infty} \frac{\mathrm{d}}{\mathrm{d}\boldsymbol{\theta}} \ln \mathrm{p}(\mathbf{y}|\boldsymbol{\theta}) \, \hat{\boldsymbol{\theta}}\left(\mathbf{y}\right) \mathrm{p}(\mathbf{y}|\boldsymbol{\theta}) \, \mathrm{d}\mathbf{y} = \frac{\mathrm{d}}{\mathrm{d}\boldsymbol{\theta}} \mathrm{E}\left\{ \hat{\boldsymbol{\theta}}\left(\mathbf{y}\right) \right\}, \end{aligned} \tag{A.7}$$

and by using $\mathrm{VAR}\left\{ \frac{\mathrm{d}}{\mathrm{d}\boldsymbol{\theta}} \ln \mathrm{p}(\mathbf{y}|\boldsymbol{\theta}) \right\} = \mathrm{E}\left\{ \left| \frac{\mathrm{d}}{\mathrm{d}\boldsymbol{\theta}} \ln \mathrm{p}(\mathbf{y}|\boldsymbol{\theta}) \right|^2 \right\}$, Equation A.6 can be rewritten as

$$\left| \frac{\mathrm{d}}{\mathrm{d}\boldsymbol{\theta}} \mathrm{E}\left\{ \hat{\boldsymbol{\theta}}\left(\mathbf{y}\right) \right\} \right|^2 \leq \mathrm{E}\left\{ \left| \frac{\mathrm{d}}{\mathrm{d}\boldsymbol{\theta}} \ln \mathrm{p}(\mathbf{y}|\boldsymbol{\theta}) \right|^2 \right\} \mathrm{VAR}\left\{ \hat{\boldsymbol{\theta}}\left(\mathbf{y}\right) \right\}. \tag{A.8}$$

By reorganizing Equation A.8, the CRLB can be written as

$$\mathrm{VAR}\left\{ \hat{\boldsymbol{\theta}}\left(\mathbf{y}\right) \right\} \geq \frac{\left| \frac{\mathrm{d}}{\mathrm{d}\boldsymbol{\theta}} \mathrm{E}\left\{ \hat{\boldsymbol{\theta}}\left(\mathbf{y}\right) \right\} \right|^2}{\mathrm{E}\left\{ \left| \frac{\mathrm{d}}{\mathrm{d}\boldsymbol{\theta}} \ln \mathrm{p}(\mathbf{y}|\boldsymbol{\theta}) \right|^2 \right\}}. \tag{A.9}$$

If the estimator is unbiased, the previous equation simplifies to

$$\mathrm{VAR}\left\{\hat{\boldsymbol{\theta}}\left(\mathbf{y}\right)\right\} \geq \frac{1}{\mathrm{E}\left\{\left|\frac{\mathrm{d}}{\mathrm{d}\boldsymbol{\theta}}\ln \mathrm{p}(\mathbf{y}|\boldsymbol{\theta})\right|^2\right\}}. \tag{A.10}$$

For a vector estimator with multiple parameters to be estimated, the CRLB of parameter θ_i is equivalent to the inverse of the diagonal components of the FIM $\left[\mathrm{F}\left(\boldsymbol{\theta}\right)^{-1}\right]_{i,i}$ and can be written as

$$\mathrm{VAR}\left\{\hat{\theta}_i\left(\mathbf{y}\right)\right\} \geq \frac{1}{\mathrm{E}\left\{\left|\frac{\mathrm{d}}{\mathrm{d}\theta_i}\ln \mathrm{p}(\mathbf{y}|\boldsymbol{\theta})\right|^2\right\}}. \tag{A.11}$$

Finally, the joint PDF of the measurement $\mathbf{y}$ based on the parameter vector $\boldsymbol{\theta}$ is expressed as the multiplication of the individual PDFs for each measurement y_i and can be written as

$$\mathrm{p}\left(\boldsymbol{y}|\boldsymbol{\theta}\right) = \prod_{i=1}^{m} \mathrm{p}\left(y_i|\boldsymbol{\theta}\right) = \left(2\pi\sigma^2\right)^{-\frac{m}{2}} e^{-\frac{1}{2\sigma^2}\sum_{i=1}^{m}|s_i(\boldsymbol{\theta})-y_i|^2}, \tag{A.12}$$

where each of the m observed measurements is considered to have experienced AWGN with zero mean and variance σ^2, and $s_i\left(\boldsymbol{\theta}\right)$ are the signal samples which are dependent on the parameter $\boldsymbol{\theta} = [\theta_1, ..., \theta_L]$.

Equations A.11 and A.12 are used in Chapter 5 to derive the CRLB of an unbiased LoS delay estimator to compare the distance estimation accuracy of the proposed SBDist communication system to other communication systems such as ITS-G5 and IR-UWB.

Appendix B

ATC system modeling using PN

This chapter is intended to provide a detailed description to the ATC system model. PN is used to model the SBDist system and the control system and their interactions as well as the interactions with other systems. While the control system must interact with other systems such as the on-board speed estimation system, brakes, gauges, and other mechanical devices, these systems are not modeled in this work and they are considered to have a deterministic and constant input or output based on the interaction.

As described in Chapter 6, STPN is adopted to model the SBDist system and the control system. STPN uses places and transitions to describe events and the conditions of them being triggered. The reader is encouraged to refer to Chapter 6 and the references thereon for more details on STPN, places, transitions, and their definitions.

In this chapter, the focus is to provide the complete STPN representation of the SBDist and control systems and to define each place and how it relates to the connected places. The complete system representation for ATC is shown in Figure B.1. The Figure represents a complete ATC maneuver including initialization, communication, coupling, and special cases where alarms or emergencies may occur.

Before describing each place, it must be noted that some places are

highlighted with green stripes to indicate that these places are used to visualize a state to the driver by switching on a specific light indicator in the driver's cabin. These are places p_{03}, p_{20}, p_{22}, p_{32}, p_{40}, p_{45}, and p_{47}. Furthermore, place p_{04} is highlighted with blue stripes. This place reflects the driver pressing on the maneuver start button. An exemplary interface to visualize the button and light indicators is shown in Figure B.2. In order to maintain consistent terminology, the train wagon being modeled is referred to as **TW1** and the train wagon involved in the maneuver is referred to as **TW2**.

Each of the ATC model places are described in the following.

P_{00} and P_{01} The SBDist system transmits periodically a beacon signal to search for other train wagons within range. This is done in a loop with a predefined period.

P_{02} This place signals the reception of a beacon signal from **TW2** pointing out that it is within range.

P_{03} This place functions as a visual indicator to the train driver to signal the detection of a signal from **TW2**.

P_{04} This place indicates the press of the maneuver start button by the train driver. This flags the start of the maneuver and gives **TW1** the master role and **TW2** the slave role.

P_{05} This place Receives the velocity of **TW2** and maintains a loop to ensure receiving velocity updates from **TW2** until the velocities of both trains are equal.

P_{06} This place signals the reception of the velocity of **TW1** from the WTB.

P_{07} This place signals the reception of the velocity of **TW2**.

P_{08} This place signals the reception of a distance estimate between **TW1** and **TW2**. The estimate is calculated by the SBDist system and is used to evaluate the integrity of the velocity estimations.

P_{09} This place is activated if the velocity from **TW1** is larger than that from **TW2**.

P_{10} This place is activated if the velocity from **TW1** is smaller than that from **TW2**.

P_{11} This place is activated if the velocity from **TW1** is equal to that from **TW2**.

P_{12} This place highlights **TW1** sending a message to **TW2** ordering it to increase its velocity.

P_{13} This place highlights **TW1** sending a message to **TW2** ordering it to decrease its velocity.

P_{14} This place is used to send a message to **TW2** confirming that the velocities of both wagons are equal and that it is possible to start the ATC maneuver.

P_{15} This place activates a timer until an acknowledgement is received from **TW2**.

P_{16} This place signals the reception of an acknowledgement from **TW2** agreeing to start the ATC maneuver.

P_{17} This place is used to send a message to **TW2** asking for an updated velocity and distance estimate.

P_{18} This place indicates the reception of an updated velocity and distance estimate from **TW2**.

P_{19} This place informs the control node that regular communication is maintained between the train wagons.

P_{20} his place functions as a visual indicator to the train driver to signal a communication establishment between the train wagons.

P_{21} This place forwards the signal from P_{19} to the next transition.

P_{22} This place is activated when both wagons have equal velocities and the communication is maintained. It acts as a visual indicator to the driver indicating the constant relative velocity is achieved.

P_{23} This place is activated when both wagons have equal velocities and the communication is maintained. It forwards this information to the next transition.

P_{24} This place indicates that the velocity-distance lookup table is imported from the train database.

P_{25} This place confirms that both trains are within the velocity limits based on their distance. It forwards this information to the SBDist system.

P_{26} The control node receives an acknowledgement from **TW2** allowing it to start the ATC maneuver.

P_{27} This place indicates the state of the communication. If there is an error, it will forward a request to the SBDist system asking for a communication reestablishment and measurement updates from **TW2**.

P_{28} This place indicates the reception of velocity and distance estimate measurements from **TW2** and the distance estimate from **TW1**.

P_{29} This place indicates the reception of velocity estimate measurements from **TW1**.

P_{30} This place uses the received measurements and compares them to the data received from the database to ensure that the velocities of both trains are within the predefined thresholds.

P_{31} This place is activated when the wagons are within the thresholds, that is, in normal operation.

P_{32} This place gives a visual indication to the driver that normal operation is ongoing.

P_{33} This place compares the relative velocity of the wagons to the preferred relative velocity retrieved from the database.

P_{34} This place decides whether the train needs to increase, decrease, or maintain velocity based on the input from P_{33}.

P_{35} This place informs the mechanical devices to maintain the current velocity.

P_{36} This place informs the mechanical devices to increase velocity.

P_{37} This place informs the mechanical devices to decrease velocity.

P_{38} This place maintains the normal operation loop and indicates to the control node when the current loop is concluded to start receiving new measurements from the other systems.

P_{39} This place is activated when the received message from **TW2** is corrupted or if there are any other communication problems.

P_{40} This place gives the driver a visual indication that there is a communication system error.

P_{41} This place is activated after a certain amount of consecutive communication errors are received. The amount of communication errors is based on the distance between the two wagons as explained in Chapter 6.

P_{42} This place is activated if a certain amount of consecutive communication errors occurred or if the relative velocity between the wagons is beyond the threshold of normal operation. This still assumes that the wagon will be able to brake in time that an accident can be avoided.

P_{43} This place is activated when the speed between the wagons exceeds the threshold of normal operation and an accident can no longer be avoided.

P_{44} This place is used to order the mechanical devices to perform an emergency brake maneuver to avoid an accident.

P_{45} This place functions as a visual indicator to the train driver to signal an alarm and that the ATC maneuver failed.

P_{46} This place is used to order the mechanical devices to perform an emergency brake maneuver.

P_{47} This place functions as a visual indicator to the train driver to signal an emergency and that an accident is about to occur.

P_{48} This place is used to send an automatic emergency message to the authorities to inform them that an accident is about to occur.

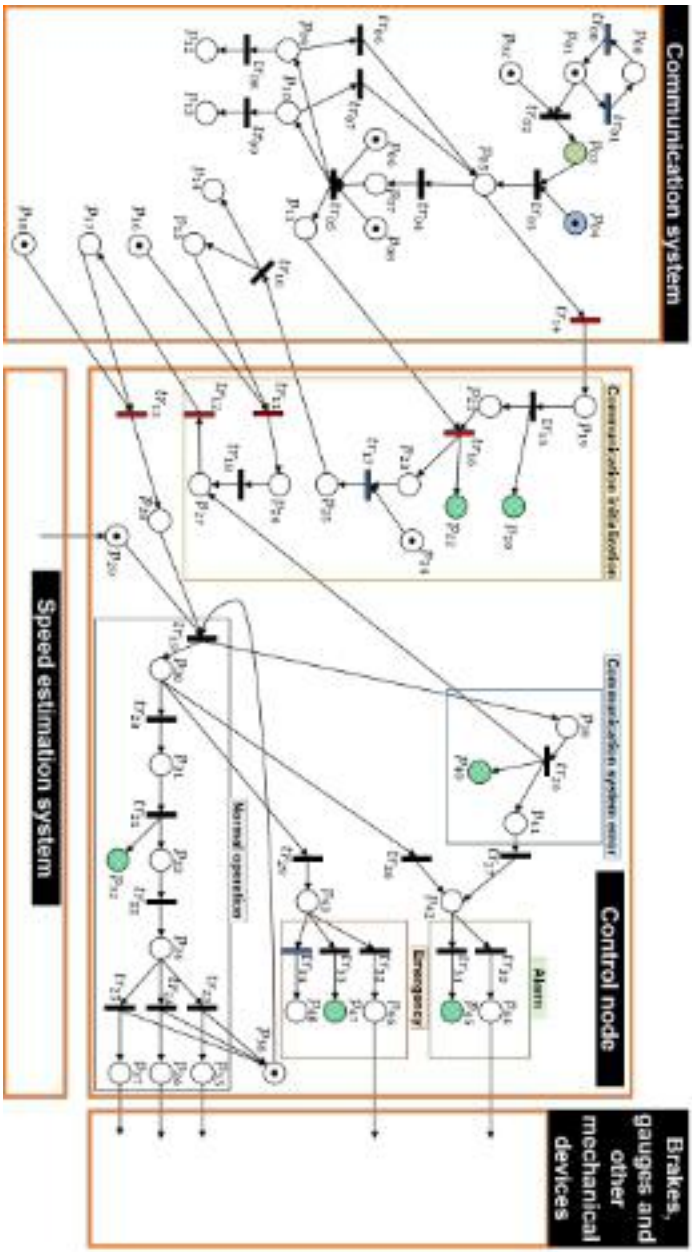

Figure B.1: Petri Net representation of the ATC maneuver, including the SBDist and control systems.

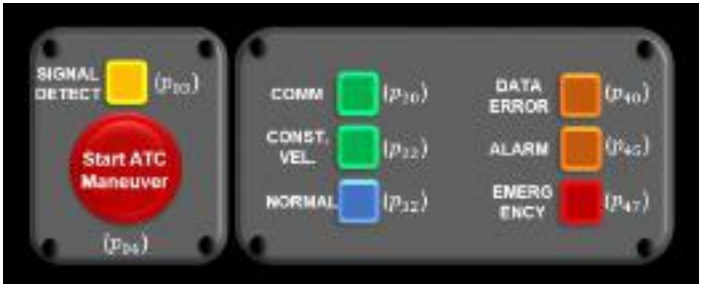

Figure B.2: A representation of the ATC interface including a maneuver start button and other light indicators.

Acronyms

5G Fifth Generation Mobile Network. 17, 39, 40, 41

ABB ASEA Brown Boveri. 11

AI Artificial Intelligence. 105

ATC Automatic Train Coupling. 3, 4, 5, 6, 8, 9, 15, 16, 17, 18, 20, 21, 22, 23, 24, 25, 26, 28, 33, 34, 36, 37, 39, 41, 51, 52, 56, 61, 63, 70, 74, 76, 82, 85, 86, 87, 88, 89, 93, 94, 95, 96, 97, 98, 99, 101, 102, 103, 104, 105, 113, 114, 115, 116, 118, 119, 120

AWGN Additive White Gaussian Noise. 31, 32, 61, 66, 102, 111

CDF Cumulative Distribution Function. 78, 79, 80, 81

CPA Circularly Polarized Antenna. 7, 24, 32, 33, 34, 36, 37, 40, 98, 99, 100, 102, 103

CRLB Cramér Rao Lower Bound. 7, 66, 67, 69, 82, 103, 109, 110, 111

CTC Centralized Traffic Control. 2, 15, 17

D2D Device-to-Device. 6, 18, 24, 101

DAC Digital to Analog Converter. 28, 29

DLR German Aerospace Center. 7, 42, 43

DMO Direct-Mode Operation. 17, 18

ECTS European Train Control System. 16, 17

EM Expectation Maximization. 8, 72, 73, 74

ETCS European Train Control System. 2

ETSI European Telecommunications Standards Institute. 18

FDD Frequency Division Duplex. 20, 35

FFT Fast Fourier Transform. 29

FIM Fisher Information Matrix. 67, 68, 69, 111

FIR Finite Impulse Response. 28

FRMCS Future Railway Mobile Communication System. 6, 17

GPRS General Packet Radio Service. 16, 17

GPS Global Positioning System. 18, 62, 78, 79, 80, 81, 83, 89, 103, 104

GR Ground-Reflected. 28, 29, 31, 32, 33, 54, 55, 64, 65, 67, 71, 79, 102

GSM Global System for Mobile Communications. 16

GSM-R Global System for Mobile Communications - Railway. 2, 6, 16, 17, 24

HST High Speed Trains. 1, 2, 3

ICE Inter-City Express. 87

IEC International Electrotechnical Commission. 11, 15, 90

IEEE Institute of Electrical and Electronics Engineers. 6, 11, 16, 18, 27, 63, 64, 82

IFFT Inverse Fast Fourier Transform. 30

IQ In-phase and Quadrature. 26, 43

IR-UWB Impulse Radio - Ultra Wide Band. 7, 24, 63, 64, 69, 70, 82, 103, 111

ISM Industrial, Scientific and Medical. 7, 25, 39, 102

ITS-G5 Intelligent Transport Systems at 5.9 GHz. 6, 7, 17, 18, 63, 64, 69, 70, 71, 101, 103, 111

KF Kalman Filter. 75, 76, 77, 78, 79, 80, 81, 82

LNA Low Noise Amplifier. 43

LO Local Oscillator. 43

LoS Line-of-Sight. 28, 29, 31, 32, 33, 40, 54, 55, 56, 58, 61, 64, 65, 67, 71, 72, 74, 79, 80, 81, 102, 111

LTE-R Long Term Evolution - Railway. 6, 16, 17, 24

ML Machine Learning. 105

MLE Maximum Likelihood Estimation. 72, 73, 74

MMSE Minimum Mean Square Error. 29, 95

mm-Wave Millimeter Wave. 5, 6, 7, 8, 19, 25, 27, 28, 29, 33, 36, 39, 40, 41, 42, 43, 44, 45, 46, 47, 49, 50, 51, 52, 56, 57, 58, 63, 64, 69, 70, 71, 82, 83, 85, 87, 89, 91, 93, 97, 98, 99, 100, 102, 104

MSC Mobile Switching Center. 16

MUSIC Multiple Signal Classification. 72

MVB Multifunction Vehicle Bus. 6, 11, 12, 13, 14, 15, 22, 93, 97

OFDM Orthogonal Frequency Division Multiplexing. 25, 69, 82

PDF Probability Density Function. 9, 67, 109, 111

PER Packer Error Rate. 4, 5, 7, 20, 24, 25, 27, 31, 32, 33, 34, 35, 36, 37, 57, 58, 90, 97, 98, 100, 102, 103, 104

PFH probability of failure per hour. 90, 97, 98, 103, 104

PN Petri Nets. 8, 91, 92, 93, 113

QPSK Quadrature Phase Shift Keying. 26, 27, 30

RIS Reconfigurable Intelligent Surfaces. 104

RRC Root-Raised Cosine. 28, 29

RSU Road Side Unit. 17, 18

RTD Round Trip Delay. 7, 61, 62, 63, 83, 103

RTP Real-Time Protocol. 13

SAGE Space-Alternating Generalized Expectation-maximization. 8, 55, 58, 73, 74, 76, 77, 78, 79, 80, 81, 82, 83, 103

SBDist Reliable and Low-Latency Broadband Transmission over Short Distances. 5, 6, 7, 8, 16, 19, 20, 21, 22, 24, 25, 36, 39, 101, 102, 103, 104, 105, 111, 113, 114, 115, 116, 119

SC Single Carrier. 5, 19, 20, 25, 82

SC-FDE Single Carrier with Frequency Domain Equalization. 24, 25, 26, 27, 28, 31, 32, 34, 36, 39, 50, 56, 63, 64, 69, 70, 71, 72, 82, 85, 87, 89, 91, 93, 97, 98, 99, 100

SIL Safety Integrity Level. 8, 90, 97, 98, 100, 103, 104

SINR Signal to Interference Noise Ratio. 40

SNR Signal-to-Noise Ratio. 31, 32

STPN Stochastic Timed Petri Nets. 85, 92, 93, 94, 99, 103, 105, 113

T2T Train-to-Train. 4, 6, 7, 17, 18, 23, 32, 33, 39, 41, 52, 57, 58, 101, 102, 103

TCN Train Communication Network. 6, 8, 11, 12, 14, 15, 19, 21, 22, 23, 86

TDMA Time Division Multiple Access. 18

TDoA Time Difference of Arrival. 61, 62, 63, 83, 103

TETRA Terrestrial Trunked Radio. 6, 16, 17, 18

TINA TIme petri Net Analyzer. 93, 99

ToA Time of Arrival. 7, 61, 62, 63, 78, 83, 89, 103, 104

UHF Ultra High Frequency. 18

UIC International Union of Railways. 11, 15, 17

URLLC Ultra-Reliable Low-Latency Communication. 4, 19, 24, 103

USRP Universal Software Radio Peripheral. 50

WTB Wire Train Bus. 6, 11, 13, 14, 15, 19, 21, 22, 24, 25, 36, 92, 93, 97, 114

Bibliography

[A8H] "German A8 Highway", `https://de.m.wikipedia.org/wiki/Datei:Autobahn_A8_bei_Holzkirchen.JPG#metadata`, accessed: 21.10.2024.

[ABAH18] A. Al-Bassam, W. Alshrafi, and D. Heberling, "A 60 GHz circularly polarized antenna array for line-of-sight train-to-train communication", *2018 11th German Microwave Conference (GeMiC)*, pp. 148–151, 2018.

[ACM02] B. Allotta, V. Colla, and M. Malvezzi, "Train position and speed estimation using wheel velocity measurements", *Proceedings of the Institution of Mechanical Engineers, Part F: Journal of Rail and Rapid Transit*, volume 216, no. 3, pp. 207–225, 2002.

[AKIR16] M. O. Al Kalaa, A. Imran, and H. H. Refai, "mmWave based vs 2 GHz networks: What is more energy efficient?", *2016 International Wireless Communications and Mobile Computing Conference (IWCMC)*, pp. 67–71, 2016.

[AWW+13] Y. Azar, G. N. Wong, K. Wang, R. Mayzus, J. K. Schulz, H. Zhao, F. Gutierrez, D. Hwang, and T. S. Rappaport, "28 GHz propagation measurements for outdoor cellular communications using steerable beam antennas in New York city", *2013 IEEE International Conference on Communications (ICC)*, pp. 5143–5147, 2013.

[AZSK19] K. Aono, B. Zheng, M. Sawahashi, and N. Kamiya, "Performance of FDE Using Cyclic-Shifted CDM Based Pilot Signal Multiplexing for Single-Carrier LOS-MIMO", *2019 IEEE 90th Vehicular Technology Conference (VTC2019-Fall)*, pp. 1–6, 2019.

[BG91] F. Belli and K.-E. Grosspietsch, "Specification of fault-tolerant system issues by predicate/transition nets and regular expressions-

approach and case study", *IEEE Transactions on Software Engineering*, volume 17, no. 6, pp. 513–526, 1991.

[BG18] A. Boussif and M. Ghazel, "Model-Based Monitoring of a Train Passenger Access System", *IEEE Access*, volume 6, pp. 41619–41632, 2018.

[BL06] E. K. Blum and S. V. Lototsky, *Mathematics of physics and engineering*, World Scientific Publishing Company, 2006.

[BS19] D. Becker and L. Schalk, "Enabling Air-to-Air Wideband Channel Measurements between Small Unmanned Aerial Vehicles with Optical Fibers", *2019 IEEE/AIAA 38th Digital Avionics Systems Conference (DASC)*, pp. 1–7, 2019.

[BV06] B. Berthomieu and F. Vernadat, "Time Petri nets analysis with TINA", pp. 123–124, 01 2006.

[Chu72] D. Chu, "Polyphase codes with good periodic correlation properties", *IEEE Transactions on Information Theory*, volume 18, no. 4, pp. 531–532, 1972.

[CLML18] R. Chen, W.-X. Long, G. Mao, and C. Li, "Development Trends of Mobile Communication Systems for Railways", *IEEE Communications Surveys & Tutorials*, volume 20, no. 4, pp. 3131–3141, 2018.

[CMT21] E. Commission, D.-G. for Mobility, and Transport, *EU transport in figures : statistical pocketbook 2021*, Publications Office, 2021.

[DT89] J. Dugan and K. Trivedi, "Coverage modeling for dependability analysis of fault-tolerant systems", *IEEE Transactions on Computers*, volume 38, no. 6, pp. 775–787, 1989.

[ETS15] ETSI, "Universal Mobile Telecommunications System (UMTS); Multiplexing and channel coding (FDD)", *3GPP TS 25.212*, volume 01, 2015.

[ETS19] T. ETSI, "Etsi en 302 663 v1. 3.0-intelligent transport systems (its); access layer specification for intelligent transport systems operating in the 5 ghz frequency band", *ETSI, May*, 2019.

[Eur16] EuroSpec, "Specification for Automatic Couplers", *SNCF*, volume 1, 2016.

[FH94] J. Fessler and A. Hero, "Space-alternating generalized expectation-maximization algorithm", *IEEE Transactions on Signal Processing*, volume 42, no. 10, pp. 2664–2677, 1994.

[Fit06] M. Fitzmaurice, "Use of 2.4 GHz frequency band for Communications Based Train Control data communications systems", *Proceedings of the 2006 IEEE/ASME Joint Rail Conference*, pp. 263–267, 2006.

[FR817] "FR8RAIL Project D5.1 - State of the Art on Automatic Couplers", 2017.

[FTH+99] B. Fleury, M. Tschudin, R. Heddergott, D. Dahlhaus, and K. Ingeman Pedersen, "Channel parameter estimation in mobile radio environments using the SAGE algorithm", *IEEE Journal on Selected Areas in Communications*, volume 17, no. 3, pp. 434–450, 1999.

[GAP+18] K. Guan, B. Ai, B. Peng, D. He, G. Li, J. Yang, Z. Zhong, and T. Kuerner, "Towards Realistic High-Speed Train Channels at 5G Millimeter-Wave Band-Part I Paradigm, Significance Analysis, and Scenario Reconstruction", *IEEE Transactions on Vehicular Technology*, volume 67, no. 10, pp. 9112–9128, 2018.

[GGB+02] F. Gustafsson, F. Gunnarsson, N. Bergman, U. Forssell, J. Jansson, R. Karlsson, and P.-J. Nordlund, "Particle filters for positioning, navigation, and tracking", *IEEE Transactions on Signal Processing*, volume 50, no. 2, pp. 425–437, 2002.

[Gha09] M. Ghazel, "Using Stochastic Petri Nets for Level-Crossing Collision Risk Assessment", *IEEE Transactions on Intelligent Transportation Systems*, volume 10, no. 4, pp. 668–677, 2009.

[Gha17] M. Ghazel, "A Control Scheme for Automatic Level Crossings Under the ERTMS/ETCS Level 2/3 Operation", *IEEE Transactions on Intelligent Transportation Systems*, volume 18, no. 10, pp. 2667–2680, 2017.

[GMB+18] A. A. Gómez, E. Mozo, L. Bernadó, S. Zelenbaba, T. Zemen, F. Parrilla, and A. Alberdi, "Performance Analysis of ITS-G5 for Smart Train Composition Coupling", *2018 16th International Conference on Intelligent Transportation Systems Telecommunications (ITST)*, pp. 1–7, 2018.

[GPH+21] K. Guan, B. Peng, D. He, J. M. Eckhardt, H. Yi, S. Rey, B. Ai, Z. Zhong, and T. Kuerner, "Channel Sounding and Ray Tracing for Intrawagon Scenario at mmWave and Sub-mmWave Bands", *IEEE*

Transactions on Antennas and Propagation, volume 69, no. 2, pp. 1007–1019, 2021.

[HAW+16] R. He, B. Ai, G. Wang, K. Guan, Z. Zhong, A. F. Molisch, C. Briso-Rodriguez, and C. P. Oestges, "High-Speed Railway Communications: From GSM-R to LTE-R", *IEEE Vehicular Technology Magazine*, volume 11, no. 3, pp. 49–58, 2016.

[HK04] L. Huang and C. C. Ko, "Performance of maximum-likelihood channel estimator for UWB communications", *IEEE Communications Letters*, volume 8, no. 6, pp. 356–358, 2004.

[HSA+20] R. He, C. Schneider, B. Ai, G. Wang, Z. Zhong, D. A. Dupleich, R. S. Thomae, M. Boban, J. Luo, and Y. Zhang, "Propagation Channels of 5G Millimeter-Wave Vehicle-to-Vehicle Communications Recent Advances and Future Challenges", *IEEE Vehicular Technology Magazine*, volume 15, no. 1, pp. 16–26, 2020.

[IEC] "IEC 61375-1: Electronic railway equipment - Train communication network (TCN) - General architecture", `https://webstore.iec.ch/publication/5397`, accessed: 01.06.2022.

[IEC02] IEC, "Functional safety of electrical/electronic/programmable electronic safety-related systems", volume 1-7, 2002.

[IEE99] "IEEE Standard for Communications Protocol Aboard Trains", *IEEE Std 1473-1999*, pp. 1–20, 1999.

[IEE09] "IEEE Standard for Information technology– Local and metropolitan area networks– Specific requirements– Part 15.3: Amendment 2: Millimeter-wave-based Alternative Physical Layer Extension", *IEEE Std 802.15.3c-2009 (Amendment to IEEE Std 802.15.3-2003)*, pp. 1–200, 2009.

[IFS] "IFS Department at RWTH Aachen University", `https://www.google.com/maps/@50.7806679,6.0691503,172m/data=!3m1!1e3?entry=ttu&g_ep=EgoyMDI0MTIwNC4wIKXMDSoASAFQAw%3D%3D`, accessed: 21.10.2024.

[ITU03] "Recommendation ITU-R P.838-2 Specification attenuation model for rain for use in prediction methods", *Standard*, International Telecommunication Union, 2003.

[JJL+21] A. Jia, S. Jiang, Y. Lv, X. Zhang, T. Chang, I. Rashdan, P. Unterhuber, and W. Wang, "Connectivity Analysis of V2V Channel at

Intersections", *2021 15th European Conference on Antennas and Propagation (EuCAP)*, pp. 1–4, 2021.

[KBNJ06] K. Kastell, S. Bug, A. Nazarov, and R. Jakoby, "Improvments in Railway Communication via GSM-R", *2006 IEEE 63rd Vehicular Technology Conference*, volume 6, pp. 3026–3030, 2006.

[KCH+17] J. Ko, Y.-J. Cho, S. Hur, T. Kim, J. Park, A. F. Molisch, K. Haneda, M. Peter, D.-J. Park, and D.-H. Cho, "Millimeter-Wave Channel Measurements and Analysis for Statistical Spatial Channel Model in In-Building and Urban Environments at 28 GHz", *IEEE Transactions on Wireless Communications*, volume 16, no. 9, pp. 5853–5868, 2017.

[KD18] K.-D. Kammeyer and A. Dekorsy, *Nachrichtenübertragung*, Springer Vieweg, Wiesbaden, Germany, 6th edition, Dec 2018, ISBN 978-3-658-17004-2.

[Kje96] S. Kjesbu, "Digital communications in advanced safety systems for trains", *Proceedings of the 1996 ASME/IEEE Joint Railroad Conference*, pp. 67–70, 1996.

[KN07] S. Khalesehosseini and J. Nielsen, "Generalized CRLB for DA and NDA Synchronization of UWB Signals with Clock Offset", *2007 IEEE International Conference on Communications*, pp. 4305–4310, 2007.

[LG07] S. Loyka and F. Gagnon, "On Accuracy and Efficiency of Monte-Carlo BER Simulations for Fading Channels", *2007 International Symposium on Signals, Systems and Electronics*, pp. 255–258, 2007.

[LS87] N. Leveson and J. Stolzy, "Safety Analysis Using Petri Nets", *IEEE Transactions on Software Engineering*, volume SE-13, no. 3, pp. 386–397, 1987.

[LS02] J.-Y. Lee and R. Scholtz, "Ranging in a dense multipath environment using an UWB radio link", *IEEE Journal on Selected Areas in Communications*, volume 20, no. 9, pp. 1677–1683, 2002.

[LSU17] A. Lehner, T. Strang, and P. Unterhuber, "Train-to-train propagation at 450 MHz", *2017 11th European Conference on Antennas and Propagation (EUCAP)*, pp. 2875–2879, 2017.

[MLLC14] K. M. Mak, H. W. Lai, K. M. Luk, and C. H. Chan, "Circularly Polarized Patch Antenna for Future 5G Mobile Phones", *IEEE Access*, volume 2, pp. 1521–1529, 2014.

[MNH+22] V. Maglogiannis, D. Naudts, S. Hadiwardoyo, D. van den Akker, J. Marquez-Barja, and I. Moerman, "Experimental V2X Evaluation for C-V2X and ITS-G5 Technologies in a Real-Life Highway Environment", *IEEE Transactions on Network and Service Management*, volume 19, no. 2, pp. 1521–1538, 2022.

[Moo96] T. Moon, "The expectation-maximization algorithm", *IEEE Signal Processing Magazine*, volume 13, no. 6, pp. 47–60, 1996.

[MRSD15] G. R. Maccartney, T. S. Rappaport, S. Sun, and S. Deng, "Indoor Office Wideband Millimeter-Wave Propagation Measurements and Channel Models at 28 and 73 GHz for Ultra-Dense 5G Wireless Networks", *IEEE Access*, volume 3, pp. 2388–2424, 2015.

[NGAT17] M. G. Nilsson, C. Gustafson, T. Abbas, and F. Tufvesson, "A Measurement-Based Multilink Shadowing Model for V2V Network Simulations of Highway Scenarios", *IEEE Transactions on Vehicular Technology*, volume 66, no. 10, pp. 8632–8643, 2017.

[OS14] A. V. Oppenheim and R. W. Schafer, *Discrete-time signal processing*, Pearson Education Limited, 2014.

[RBDMQ12] T. S. Rappaport, E. Ben-Dor, J. N. Murdock, and Y. Qiao, "38 GHz and 60 GHz angle-dependent propagation for cellular peer-to-peer wireless communications", *2012 IEEE International Conference on Communications (ICC)*, pp. 4568–4573, 2012.

[RGLSF08] C. Rico Garcia, A. Lehner, T. Strang, and K. Frank, "Channel Model for Train to Train Communication Using the 400 MHz Band", *VTC Spring 2008 - IEEE Vehicular Technology Conference*, pp. 3082–3086, 2008.

[Sch86] R. Schmidt, "Multiple emitter location and signal parameter estimation", *IEEE Transactions on Antennas and Propagation*, volume 34, no. 3, pp. 276–280, 1986.

[SH00] C. Schifers and G. Hans, "IEC 61375-1 and UIC 556-international standards for train communication", *VTC2000-Spring. 2000 IEEE 51st Vehicular Technology Conference Proceedings (Cat. No.00CH37026)*, volume 2, pp. 1581–1585 vol.2, 2000.

[SKCK16] Y.-S. Song, J. Kim, S. W. Choi, and Y.-K. Kim, "Long term evolution for wireless railway communications:testbed deployment and performance evaluation", *IEEE Communications Magazine*, volume 54, no. 2, pp. 138–145, 2016.

[Sor88] H. Sorenson, “Recursive estimation for nonlinear dynamic systems”, *Bayesian analysis of time series and dynamic models*, volume 94, pp. 127–165, 1988.

[SS14] A. Sniady and J. Soler, “LTE for Railways: Impact on Performance of ETCS Railway Signaling”, *IEEE Vehicular Technology Magazine*, volume 9, no. 2, pp. 69–77, 2014.

[SS19] H. Song and E. Schnieder, “Availability and Performance Analysis of Train-to-Train Data Communication System”, *IEEE Transactions on Intelligent Transportation Systems*, volume 20, no. 7, pp. 2786–2795, 2019.

[SSCO09] Y. Shoji, H. Sawada, C.-S. Choi, and H. Ogawa, “A Modified SV-Model Suitable for Line-of-Sight Desktop Usage of Millimeter-Wave WPAN Systems”, *IEEE Transactions on Antennas and Propagation*, volume 57, no. 10, pp. 2940–2948, 2009.

[SSK+19] M. Soliman, J. Siemons, J. Kochems, W. Alshrafi, J. Shamshoom, D. Heberling, and A. Dekorsy, “Automatic Train Coupling: Challenges and Key Enablers”, *IEEE Communications Magazine*, volume 57, no. 9, pp. 32–38, 2019.

[SSS+17] R. Sattiraju, J. Siemons, M. Soliman, W. Alshrafi, F. Rein, and H. D. Schotten, “Design of a highly reliable wireless module for ultra-low-latency short range applications”, *2017 IEEE 13th International Workshop on Factory Communication Systems (WFCS)*, pp. 1–4, 2017.

[SSSS17] M. Soliman, S. Sand, M. Schmidhammer, and E. Staudinger, “Effect of non-integer delay on ranging accuracy for ultra-reliable systems”, *2017 International Conference on Localization and GNSS (ICL-GNSS)*, pp. 1–5, 2017.

[SUDPM+18] M. Soliman, P. Unterhuber, F. De Ponte Muller, M. Schmidhammer, S. Sand, and A. Dekorsy, “Design and Evaluation of a Millimeter Wave Channel Sounder for Dynamic Propagation Measurements”, *2018 IEEE 88th Vehicular Technology Conference (VTC-Fall)*, pp. 1–5, 2018.

[SUG16] M. Soliman, P. Unterhuber, and D. Gera, “First analysis of inside Train communication with ITS-G5 measurement data”, *2016 International Symposium on Wireless Communication Systems (ISWCS)*, pp. 451–455, 2016.

[SUS+19] M. Soliman, P. Unterhuber, S. Sand, E. Staudinger, J. Shamshoom, C. Schindler, and A. Dekorsy, "Dynamic Train-to-Train Propagation Measurements in the Millimeter Wave Band - Campaign and First Results", *2019 13th European Conference on Antennas and Propagation (EuCAP)*, pp. 1–5, 2019.

[SWJ+16] M. Sybis, K. Wesolowski, K. Jayasinghe, V. Venkatasubramanian, and V. Vukadinovic, "Channel Coding for Ultra-Reliable Low-Latency Communication in 5G Systems", *2016 IEEE 84th Vehicular Technology Conference (VTC-Fall)*, pp. 1–5, 2016.

[Tem] "Rubidium atomic clock website", `https://www.orolia.com/product/spectratime-lpfrs-rubidium-oscillator/`, accessed: 21.09.2021.

[TFB20] M. N. Tahir, S. Fatima, and N. Bashir, "Car-to-Car Communication Using ITS-G5 & 5G", *2020 IEEE 5th International Conference on Intelligent Transportation Engineering (ICITE)*, pp. 331–335, 2020.

[TMS21] M. N. Tahir, K. Mäenpää, and T. Sikuvaara, "Wireless Vehicular Communication: C-ITS Field Measurements Using ITS-G5", *2021 International Conference on Software, Telecommunications and Computer Networks (SoftCOM)*, pp. 1–4, 2021.

[UPS+16] P. Unterhuber, S. Pfletschinger, S. Sand, M. Soliman, T. Jost, A. Arriola, I. Val, C. Cruces, J. Moreno, J. P. García-Nieto, et al., "A survey of channel measurements and models for current and future railway communication systems", *Mobile Information Systems*, volume 2016, 2016.

[URWK20] P. Unterhuber, I. Rashdan, M. Walter, and T. Kürner, "Path Loss Models and Large Scale Fading Statistics for C-Band Train-to-Train Communication", *2020 14th European Conference on Antennas and Propagation (EuCAP)*, pp. 1–5, 2020.

[USS+17] P. Unterhuber, S. Sand, M. Soliman, B. Siebler, A. Lehner, T. Strang, M. d'Atri, F. Tavano, and D. Gera, "Wide band propagation in train-to-train scenarios - Measurement campaign and first results", *2017 11th European Conference on Antennas and Propagation (EUCAP)*, pp. 3356–3360, 2017.

[VZF+18] E. M. Vitucci, M. Zoli, F. Fuschini, M. Barbiroli, V. Degli-Esposti, K. Guan, B. Peng, and T. Kuerner, "Tri-Band Mm-wave Directional Channel Measurements in Indoor Environment", *2018 IEEE 29th*

Annual International Symposium on Personal, Indoor and Mobile Radio Communications (PIMRC), pp. 205–209, 2018.

[Wat96] M. Watkins, "Project EIRENE. A new radio system for the European railways", *1996 International Conference on Public Transport Electronic Systems (Conf. Publ. No. 425)*, pp. 52–56, 1996.

[WCF16] J. Wu, Y. J. Cheng, and Y. Fan, "Millimeter-Wave Wideband High-Efficiency Circularly Polarized Planar Array Antenna", *IEEE Transactions on Antennas and Propagation*, volume 64, no. 2, pp. 535–542, 2016.

[WFZ14] M. Walter, U.-C. Fiebig, and A. Zajic, "Experimental Verification of the Non-Stationary Statistical Model for V2V Scatter Channels", *2014 IEEE 80th Vehicular Technology Conference (VTC2014-Fall)*, pp. 1–5, 2014.

[WJRF17] W. Wang, T. Jost, R. Raulefs, and U.-C. Fiebig, "Ship-to-ship broadband channel measurement at 5.2 GHz on North sea", *2017 11th European Conference on Antennas and Propagation (EUCAP)*, pp. 3872–3876, 2017.

[WWS+17] X. Wu, C.-X. Wang, J. Sun, J. Huang, R. Feng, Y. Yang, and X. Ge, "60-GHz Millimeter-Wave Channel Measurements and Modeling for Indoor Office Environments", *IEEE Transactions on Antennas and Propagation*, volume 65, no. 4, pp. 1912–1924, 2017.

[XGPJ11] Z. Xiao, N. Ge, Y. Pei, and D. Jin, "SC-UWB: A low-complexity UWB technology for portable devices", *2011 IEEE International Conference on Signal Processing, Communications and Computing (ICSPCC)*, pp. 1–6, 2011.

[YSG20] Y.-H. Yang, B.-H. Sun, and J.-L. Guo, "A Single-Layer Wideband Circularly Polarized Antenna for Millimeter-Wave Applications", *IEEE Transactions on Antennas and Propagation*, volume 68, no. 6, pp. 4925–4929, 2020.

[ZQZ+19] X. Zhang, G. Qiu, J. Zhang, L. Tian, P. Tang, and T. Jiang, "Analysis of Millimeter-Wave Channel Characteristics Based on Channel Measurements in Indoor Environments at 39 GHz", *2019 11th International Conference on Wireless Communications and Signal Processing (WCSP)*, pp. 1–6, 2019.

[Zur] "Zurich Train Station", `https://commons.wikimedia.org/wiki/File:Gleise_zu_Z%C3%BCrich_HB_2010.jpg`, accessed: 21.10.2024.

[Zur05] R. Zurawski, *The Industrial Communication Technology Handbook*, Industrial Information Technology, CRC Press, 2005, ISBN 9781420037821.

[ZW87] E. Zehavi and J. Wolf, "On the performance evaluation of trellis codes", *IEEE Transactions on Information Theory*, volume 33, no. 2, pp. 196–202, 1987.

[ZZ94] R. Zurawski and M. Zhou, "Petri nets and industrial applications: A tutorial", *IEEE Transactions on Industrial Electronics*, volume 41, no. 6, pp. 567–583, 1994.